

https://dspace.org/

Numerical Investigation of Strakes and Strakelets on a Missile at High Angles of Attack

Kistan, Prevani

2007-02-28T11:38:22Z
http://hdl.handle.net/10539/2152

Downloaded from a DSpace repository. https://dspace.org/

Numerical Investigation of Strakes and Strakelets on a Missile at High Angles of Attack

Prevani Kistan

A dissertation submitted to the Faculty of Engineering and the Built Environment, University of the Witwatersrand, Johannesburg, in fulfilment of the requirements for the degree of Master of Science in Engineering.

Johannesburg, August 2006

Declaration

I declare that this dissertation is my own, unaided work, except where otherwise acknowledged. It is being submitted for the degree of Master of Science in Engineering in the University of the Witwatersrand, Johannesburg. It has not been submitted before for any degree or examination at any other university.

Signed this ___ day of _____ 20___

_____

Prevani Kistan.

Acknowledgements

Firstly, I would like to thank the Almighty for giving me the strength to get this far. To Dr Craig Law for his advice and for taking over the role of supervisor from Prof L. Ravaglia, who retired. To Dr C.P. Crosby and Mr S.G. Gobey for their technical advice, patience and support throughout my research. To my parents, my siblings and Shahen Naidoo for their patience and unwavering moral support throughout my research, especially during some really trying times in my work. To the School of Mechanical, Industrial and Aeronautical Engineering and Denel Aerospace Systems for allowing me to work towards my Masters in Science in Engineering degree. To Prof D. Degani (Isreal Technicon) and Mr P. Champigny (ONERA Châtillon) for providing research papers which are unavailable and for their technical advice. Finally to Mr Rory Yorke for his constant assistance.

Abstract

A computational fluid dynamics (CFD) study was carried out to improve the aerodynamic performance of an agile high angle of attack missile. The normal force generated by the missile strakes had to be increased at the low angles of attack and the large side forces, experienced at high angles of attack due to the formation of steady asymmetric vortices had to be eliminated using strakelets on the missile nose. The first objective was achieved by increasing the missile strake span from $0.06D$ to $0.13D$. The larger strake span increased the effective diameter of the missile body and prevented flow reattachment to the body, a problem that was experienced when the strake span was $0.06D$. Due to flow separating further away from the body, strong vortices formed on the missile strakes, resulting in an increase in the normal force generated by the missile strakes at low angles of attack. The second objective was two-fold. Prior to analysing the effect of the strakelets on a steady asymmetric flowfield, the steady asymmetric flowfield had to first be created. This was achieved by placing a permanent, geometric perturbation on the missile nose. The size of the perturbation used in the study, which was determined by an iterative process, did not force flow separation at low angles of attack and resulted in a steady asymmetric flowfield that was representative of that on a blunt-ogive body. The effect of changing the span of the strakelets and the axial position of the strakelets were then investigated. It was found that the strakelets with a span of $0.09D$, placed $1D$ from the nose tip eliminated the side forces by forcing vortex symmetry. Increasing or decreasing the span of the strakelet, positioned $1D$ from the nose tip or placing the strakelets with a span of $0.09D$ closer or further away from the nose tip did not eliminate the steady vortex asymmetry.

Contents

Declaration i

Acknowledgements ii

Abstract iii

Contents iv

List of Figures viii

List of Tables xiv

List of Symbols xv

1 Introduction 1

1.1 Flowfield Around a Missile Body at Angles of Attack 1

1.1.1 Low angles of attack ($\alpha \leq \alpha_{SV}$) 2

1.1.2 Moderate angles of attack ($\alpha_{SV} \leq \alpha \leq \alpha_{AV}$) 2

1.1.3 High angles of attack ($\alpha_{AV} \leq \alpha \leq \alpha_{UV}$) 3

1.1.4 Very high angles of attack ($\alpha \geq \alpha_{UV}$) 6

1.2 Reduction of Asymmetric Vortex Effects 6

1.2.1 Side force control 7

1.2.2 Side force alleviation 9

1.3 Document Layout 11

1.4 Motivation 12

1.5 Objectives 13

2 Validation Studies **14**

2.1 Mesh Size Sensitivity 14

2.1.1 Grid generation 15

2.1.2 Results 20

2.1.3 Discussion 25

2.2 Outlet Boundary Position 26

2.2.1 Grid generation 26

2.2.2 Results 26

2.3 Comparison Between Full Model and Half Model Simulations 28

2.3.1 Grid generation 29

2.3.2 Results 30

2.3.3 Discussion 33

2.4 Turbulence models 34

2.4.1 Grid generation 36

2.4.2 Results 36

2.4.3 Discussion 42

2.5 Conclusions 44

3 Effect of Changing the Span of Missile Strakes **45**

3.1 Grid Generation 48

3.2 Strake Height Influence on Coefficient Behaviour 49

3.3 Strake Height Effects on the Flowfield 52

3.4 Conclusion 54

4 Creation of Steady Asymmetric Vortices in CFD 55

4.1 Size of Geometric Perturbation Required to Simulate Asymmetric Vortices 59

4.1.1 Grid generation 60

4.1.2 Results for 5° angle of attack 61

4.1.3 Results for 20° angle of attack 63

4.1.4 Results for 40° angle of attack 67

4.1.5 Discussion 71

4.1.6 Confirmation of type of instability 74

4.1.7 Full length missile results 75

4.2 Effect of Axial and Circumferential Position of A Perturbation on the Flowfield 76

4.2.1 Grid generation 76

4.2.2 Results 77

4.2.3 Discussion 83

4.3 Conclusion 84

5 Effect of Strakelets on Steady Asymmetric Vortices 86

5.1 Effect of Changing the Span of the Strakelets 89

5.1.1 Grid generation 89

5.1.2 Results 91

5.1.3 Discussion 101

5.2 Effect of Changing the Axial Position of the Strakelets 105

5.2.1 Grid generation 105

5.2.2 Results 106

5.2.3 Discussion 120

5.3 Effect of Strakelets on a Steady Asymmetric Flowfield 122

5.4 Conclusion 124

6 Conclusions and Recommendations **126**

6.1 Conclusions 126

6.2 Recommendations 130

REFERENCES **131**

List of Figures

1.1 Four angle of attack regions(Ericsson and Reding, 1991) 2

1.2 Vortex flows on a body of revolution at high angles of attack (ESDU, 1989) 4

1.3 Typical axial distribution of local side force coefficient due to asymmetric vortex flow (ESDU, 1989) 5

1.4 Suggested crossflow patterns generating opposite side forces for $\phi_s = 60^\circ$ and $\phi_s = 90^\circ$ (Rao et al., 1987) 8

1.5 Effect of helical and straight body trips on side force of ogive-cylinder body (Ericsson and Reding, 1991) 10

2.1 A portion of the missile body geometry 15

2.2 Structured grid used in this study 16

2.3 A closer view of the structured grid around the body surface shown in Figure 2.2 17

2.4 Change in normal force per iteration 19

2.5 Surface pressure distribution on the three models with different grids at $\alpha = 40^\circ$ 20

2.6 Comparison of surface pressure distribution along length of body (left of the body centre-line) 21

2.7 Comparison of surface pressure distribution along length of body (right of the body centre-line) 21

2.8 Helicity density contours at $x = 2.5D$ at $\alpha = 40°$ 23

2.9 Helical density contours at $x = 3.5D$ at $\alpha = 40°$ 24

2.10 Streamlines off the surface of the missile at $\alpha = 40°$ 25

2.11 Comparison of the pressure distribution for the two outlet positions 27

2.12 Closer view of the surface pressure distribution near the missile nose for the two outlet positions. 27

2.13 Helical density contours at $x = 3.5D$ at $\alpha = 40°$ 28

2.14 Full geometry of missile body 29

2.15 A closer view of the grid constructed on the half model 29

2.16 Comparison of values of of the normal force coefficients for the half and full models 31

2.17 Comparison of values of the pitching moment coefficients for the half and full models 32

2.18 Density contours at $x = 0.31D$ at an angle of attack of 40° 32

2.19 Density contours at $x = 6.3D$ at an angle of attack of 40° 33

2.20 Comparison of values of the normal force coefficients for the two turbulence models 38

2.21 Comparison of values of the pitching moment coefficients for the two turbulence models 38

2.22 Side view of the surface pressure distributions for the different turbulence models at $\alpha = 40°$ 39

2.23 Density contour plot at $x = 3.1D$ at $\alpha = 40°$ 40

2.24 Density contour plot at $x = 5D$ at $\alpha = 40°$ 41

2.25 Density contour plot at $x = 6.3D$ at $\alpha = 40°$ 41

2.26 Comparison of normal force coefficients 42

2.27 Ribbon traces off the surface of the missile body at $\alpha = 40°$ 43

2.28 Flow development on the missile body in the high-speed wind tunnel (CSIR-Defencetek, 2004) 43

3.1 Missile body-strake configuration 45

3.2 Normal force coefficient of strakes in the presence of the body (Mach 0.8) (DAS, 2004) 47

3.3 Pitching moment coefficient of strakes in the presence of the body (Mach 0.8) (DAS, 2004) 47

3.4 Comparison of normal force coefficient between the different span configurations 50

3.5 Comparison of pitching moment coefficient between the different span configurations 51

3.6 A side view of the cross flow velocity at $x = 4.7D$ at 20° 52

3.7 A side view of the cross velocity at $x = 4.7D$ at 20° for the strakes orientated in the '+' roll orientation 53

4.1 Experimental side force coefficient on a body of revolution at Mach 0.8 (DAS (2004)) 58

4.2 Formation of steady asymmetric vortices in the high-speed wind tunnel at Mach 0.8 at an angle of attack of 30° ((CSIR-Defencetek, 2004)) 58

4.3 Body and geometric perturbation geometry 60

4.4 Surface pressure distribution on missile body at $\alpha = 5°$ for various geometric perturbations 61

4.5 Helicity density contours at $x = 6D$ at $\alpha = 5°$ for various geometric perturbations 62

4.6 Surface pressure distribution on missile body at $\alpha = 20°$ for various geometric perturbations 63

4.7 Surface pressure distribution along the length of the missile body at 20° angle of attack for various geometric perturbations 64

4.8 Helicity density contours at $x = 4D$ at $\alpha = 20°$ for various geometric perturbations 65

4.9 Helicity density contours at $x = 6D$ at $\alpha = 20°$ for various geometric perturbations 66

4.10 Surface pressure distribution on missile body at $\alpha = 40°$ for various geometric perturbations 67

4.11 Surface pressure distribution along the length of the missile body at 40° angle of attack for various geometric perturbations 68

4.12 Helicity density contours at $x = 4D$ at $\alpha = 40°$ for various geometric perturbations 69

4.13 Helicity density contours at $x = 6D$ at $\alpha = 40°$ for various geometric perturbations 70

4.14 Comparison of side force coefficient values for the different perturbations 72

4.15 Side force variation per iteration 74

4.16 Surface pressure distribution on the full length missile body 75

4.17 Front view showing the two different circumferential positions of the perturbations 77

4.18 Surface pressure distributions on missile bodies with perturbations at different axial locations ($\alpha = 40°$) 78

4.19 Helical density contours at $x = 4D$ at $\alpha = 40°$ for the perturbations at different axial locations 79

4.20 Helical density contours at $x = 6D$ at $\alpha = 40°$ for the perturbations at different axial locations 80

4.21 Streamlines on body at $\alpha = 40°$ for the perturbations at different axial locations 81

4.22 Surface pressure distribution on missile bodies with geometric perturbations at different circumferential locations ($\alpha = 40^\circ$) 82

4.23 Helical density contours at $x = 4D$ at $\alpha = 40^\circ$ for the geometric perturbations at different circumferential positions 82

5.1 Comparison of experimental side force data for a body-tail configuration with and without strakelets 87

5.2 Geometry of missile with nose strakelets 89

5.3 A close view of the structured grid constructed on the missile-strakelet geometry 90

5.4 Surface pressure distributions on the strakelet models with different spans at 40° angle of attack 91

5.5 The surface pressure distribution along the length of the body for the strakelet models with different spans 92

5.6 Flowfield on the missile bodies with strakelets with different spans at $x = 1.4D$ at an angle of attack of 40° 94

5.7 Flowfield on the missile bodies with strakelets with different spans at $x = 2.5D$ at an angle of attack of 40° 96

5.8 Flowfield on the missile bodies with strakelets with different spans at $x = 2.8D$ at an angle of attack of 40° 98

5.9 Flowfield on the missile bodies with strakelets with different spans at $x = 6D$ at an angle of attack of 40° 100

5.10 The effect of the strakelets on the normal force coefficient 105

5.11 Surface pressure distributions on the different strakelet models at different axial locations at 40° angle of attack 106

5.12 The surface pressure distribution along the length of the missile body with the different strakelet models at different axial locations 107

5.13 Flowfield on the missile bodies with different strakelet models at $x = 0.55D$ at an angle of attack of 40° 109

5.14 Flowfield on the missile bodies with different strakelet models at $x = 1.2D$ at an angle of attack of 40° 111

5.15 Flowfield on the missile bodies with different strakelet models at $x = 1.5D$ at an angle of attack of 40° 113

5.16 Flowfield on the missile bodies with different strakelet models at $x = 2.3D$ at an angle of attack of 40° 115

5.17 Flowfield on the missile bodies with different strakelet models at $x = 3.4D$ at an angle of attack of 40° 117

5.18 Flowfield on the missile bodies with different strakelet models at $x = 6.9D$ at an angle of attack of 40° 119

List of Tables

2.1 Percentage difference in the normal force and pitching moment coefficients between the full and half symmetry models 31

2.2 Percentage difference in normal force and pitching moment coefficients between the two turbulence models 37

3.1 Percentage increase in normal force coefficient and pitching moment coefficient for the different missile strake spans 50

4.1 Dimensions of geometric perturbations 59

5.1 Coefficients for Effects in a 2^3 Experiment 88

5.2 Comparison of normal force coefficients for the strakelet models with different spans 104

List of Symbols

α	Angle of attack
ϵ	Dissipation rate of kinetic energy
$\%\Delta$	Percentage change
κ	Kàrmàn's constant
ω	Specific dissipation rate of kinetic energy
ϕ	Circumferential location
ρ	Density
C_m	Pitching moment coefficient
C_N	Normal force coefficient
C_y	Side force coefficient
C_μ	Closure constant
D	Diameter
F_y	Side force
H_d	Helicity density
k	Turbulent kinetic energy
l_{ref}	Reference length
N	Normal force
M_z	Pitching moment

M	Mach number
M_∞	Freestream Mach number
M_N	Crossflow Mach number
P	static pressure
S_{ref}	Reference area
T	Static temperature
u_τ	Friction velocity
V	Freestream velocity
y	Distance from the surface
y^+	Dimensionless, sublayer-scaled, distance

Subscripts

SV	Symmetric vortices
AV	Asymmetric vortices
UV	Unsteady asymmetric vortices
S	Circumferential location of strake
S1	Circumferential location of primary separation line
S2	Circumferential location of secondary separation line
A1	Circumferential location of primary attachment line
A2	Circumferential location of secondary attachment line
Full	Full model
Half	Half model
SST	Menter-SST $k-\omega$ turbulence model

$k-\epsilon$	$k-\epsilon$ turbulence model
High	Strake span of $0.13D$
Short	Strake span of $0.06D$

1 Introduction

Missiles, unlike aircraft, have cruciform wing (and control) surfaces, which are subjected to significant three-dimensional flow. The wing and control surfaces are mounted on a relatively large diameter body, resulting in considerable mutual aerodynamic interference between these surfaces and the body. In most cases, the wing and control surfaces have similar dimensions and are often placed in fairly close proximity to one another. This gives rise to further aerodynamic interference (Dexter, 1993). In order to achieve increasing performance demands modern missiles need to manoeuver and operate at higher angles of attack than previously.

1.1 Flowfield Around a Missile Body at Angles of Attack

In the high angle of attack flight domain, the flow around a missile body is very complex. It is characterised by the presence of large separated regions that result in the development of nonlinear normal force and pitching moment characteristics (Dexter, 1993).

Ericsson and Reding (1991) identified four flow regimes in terms of angle of attack. These are illustrated in Figure 1.1. The definitions of the symbols used in Figure 1.1 are:

- α - angle of attack,
- α_{SV} - angle of attack at which symmetric vortices form,
- α_{AV} - angle of attack at which steady asymmetric vortices form, and
- α_{UV} - angle of attack at which unsteady asymmetric vortices form.

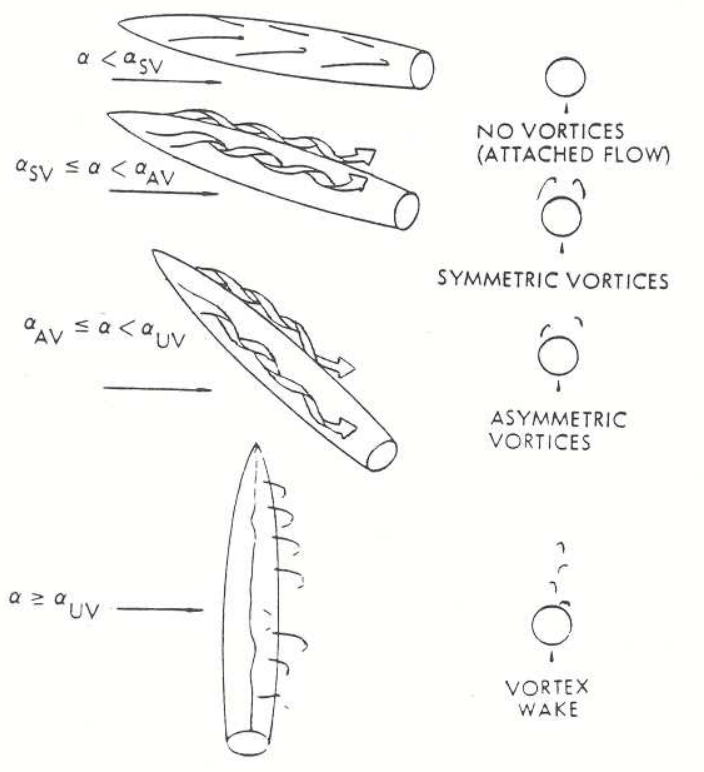


Figure 1.1: Four angle of attack regions(Ericsson and Reding, 1991)

1.1.1 Low angles of attack ($\alpha \leq \alpha_{SV}$)

The flow on a body of revolution pitched up slowly from zero angle of attack, remains attached to the body. The axial component of the flow dominates, although the transverse component of the flow is already responsible for the boundary layer thickening on the leeward side. Potential flow theory generally accounts for this first flow state. The forces that develop on the body, for example normal force, vary linearly with angle of attack (Champigny, 1994). The side force acting on the body is zero.

1.1.2 Moderate angles of attack ($\alpha_{SV} \leq \alpha \leq \alpha_{AV}$)

The transverse component of the flow becomes increasingly important. Under the influence of adverse pressure gradients and the increasing transverse flow component, flow separates on the leeward side and the resulting shear layers roll up into two well-defined vortices, which are symmetric. The separated flow is well ordered, but does introduce complexity into the aerodynamic model (Dexter, 1993). Lift increases non-linearly with the angle of attack, due to the vortex lift (Champigny, 1994). The

side force acting on the body is still zero since the formed vortices are symmetric.

1.1.3 High angles of attack ($\alpha_{AV} \leq \alpha \leq \alpha_{UV}$)

The initial steady symmetric flowfield in Section 1.1.2 around a body of revolution becomes steady asymmetric when the angle of attack of the body is further increased, even though the body and the freestream flow are symmetric. Initially several different mechanisms were suggested as causes for the formation of steady asymmetric vortices on bodies of revolution at high angles of attack, however it is now generally accepted that microscopic, time-invariant, geometric disturbances on the nose of bodies of revolution are responsible for the formation of steady asymmetric vortices.

This occurs because the flow around a body of revolution at high angles of attack is unstable (Champigny, 1994). Above a certain angle of attack it is not possible for two strong, counter-rotating vortices to co-exist symmetrically. A very small perturbation, caused by geometric imperfections on the nose of the body of revolution, is sufficient to cause the vortex system to go from a metastable symmetric state to a stable, steady asymmetric state (Champigny, 1994).

Champigny (1994) highlighted two irregularities of flow, namely a slight body sideslip and turbulence in the flow as also being responsible for the formation of asymmetric vortices. Experiments highlighted by Champigny (1994) show that while both irregularities did result in the formation of asymmetric vortices, the stable and steady nature of asymmetric vortices were not maintained, as both irregularities are temporal.

In order to maintain the stable and steady nature of asymmetric vortices the perturbation needs to be a time-invariant one, such as the geometric imperfections on the nose of a body of revolution. These permanent geometric imperfections are unavoidable as they are often due to imperfect manufacturing.

The steady asymmetric flowfield is shown in Figure 1.2. The body vortices grow with differing strengths along the length of the body, due to flow interaction with the microscopic geometric imperfections on the missile nose. The weaker vortex is forced to separate first by the the stronger vortex. The stronger vortex separates at a different axial location on the body. The weak vortex becomes the outer primary vortex. The stronger vortex that separated second, remains tucked in between the outer primary vortex and the body. The outer primary vortex moves down the length of the body and away from it, until the shear layer feeding the outer vortex

is cut. The vortex is shed, trailing off and curving into the freestream direction, downstream of the body. A new primary vortex forms inboard on the side from which the shed vortex originated, as shown in Figure 1.2. The formerly inner vortex now becomes the outer vortex and the separation process continues along the length of the body until this vortex is shed and so on (Dexter, 1993). Very long bodies can develop several pairs of asymmetric vortex pairs.

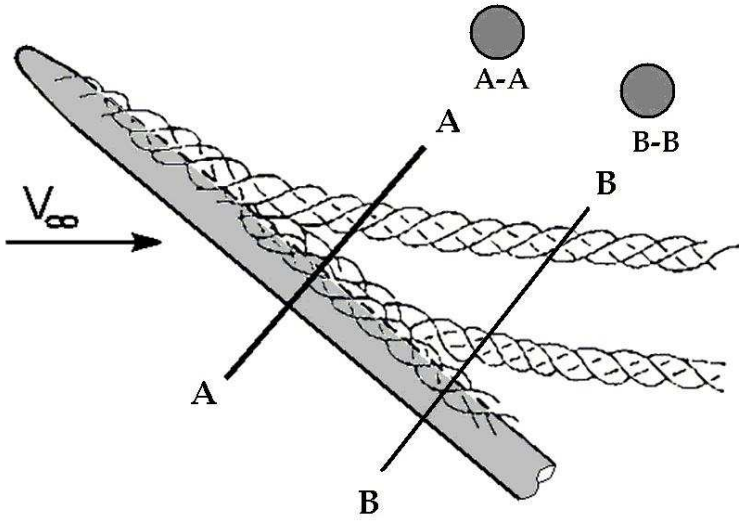


Figure 1.2: Vortex flows on a body of revolution at high angles of attack (ESDU, 1989)

Many researchers have related the unsteady two-dimensional von Kàrmàn vortex street to the steady three-dimensional vortex array, by using the principle of space-time equivalence (Ericsson and Reding, 1991). By this principle, flow development is related to time, measured either from the beginning of an impulsive two-dimensional motion or from the instant a fluid particle makes contact with a three-dimensional body. In the latter case, time is defined by a distance travelled along the body and the axial component of freestream velocity (Fidler and Bateman, 1975), as shown in section B-B in Figure 1.2.

The steady asymmetric flow on the body results in the generation of steady side forces and yawing moments on the body. Since the asymmetric flow is steady, side force distribution along the length of the body is sinusoidal and each maximum corresponds to the detachment of a vortex sheet from the body, as shown in Figure 1.3.

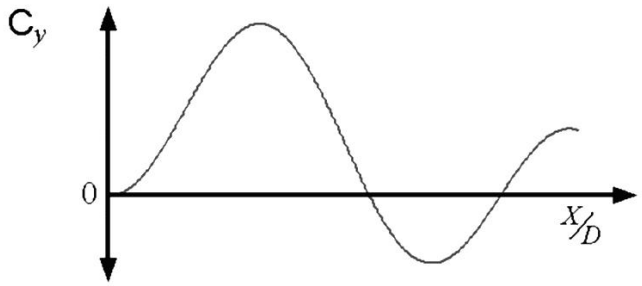


Figure 1.3: Typical axial distribution of local side force coefficient due to asymmetric vortex flow (ESDU, 1989)

Two different types of vortex asymmetry can occur:

- On a pointed, slender body steady vortex asymmetry usually begins at the nose and the frequency at which the vortices are shed increases with angle of attack (Champigny, 1994).
- On slightly blunted bodies steady vortex asymmetry usually begins at the aft end of the body and with a further increase in angle of attack, the asymmetry becomes stronger and moves forward until it reaches the nose tip of the body at high angles of attack (Dexter, 1993). Alternate vortex shedding does not occur as readily, and thus side force cells are much larger and can cover the entire cylindrical body (Champigny, 1994).

For pointed, slender bodies the angle of attack at which steady asymmetric vortices develop is dependent on the cone-half angle (θ_c) (Ericsson and Reding, 1991). Asymmetric vortex development occurs when the angle of attack is approximately double the total included angle at the apex ($\alpha_{AV} \simeq 2\theta_A$).

For slightly blunted bodies the onset angle of attack for steady asymmetric vortices is determined by the overall body fineness ratio. Ericsson and Reding (1991) provided evidence that for blunt ogive bodies, vortex asymmetry began a distance away from the nose when $\alpha_{AV} \simeq 4.2\frac{d}{l}$ where d is the diameter and l is the overall length of the body.

The existence of steady asymmetric vortices at high angles of attack has been a topic of interest since the early 1950s. Flow-visualisation pictures of experimental flows have shown the existence of steady asymmetric vortices (Levy et al., 1996). In the 1970s schilieren pictures confirmed that vortices curve away from the body on alternate sides, and move downstream at a small angle to the freestream direction (Levy et al., 1996).

1.1.4 Very high angles of attack ($\alpha \geq \alpha_{UV}$)

Finally, at very high angles of attack, when the body is almost perpendicular to the flow, the previously described stable and steady asymmetric flow, now changes into a time-dependent flow, becoming a two-dimensional flow around the cylinder at 90° angle of attack. This develops gradually from the aft end of the body, manifesting itself as a periodic fluctuation superimposed on an asymmetric pressure distribution around the body and moves forward with increasing angle of attack.

On a long body, the aft end may be subjected to significant periodic fluctuations while a steady flow is present on the front of the body. Increasing the angle of attack causes the fluctuating region to spread further upstream, resulting in reduced, mean local side forces (Champigny, 1994).

1.2 Reduction of Asymmetric Vortex Effects

Due to unavoidable microscopic manufacturing imperfections on the nose cones of missiles, steady asymmetric vortices will always occur at high angles of attack. Therefore some form of control or alleviation is required. In the absence of control, a missile maneuvering at high angles of attack, will experience large continuous side forces and moment changes that vary erratically with angle of attack (Ericsson and Reding, 1991). The side on which the side forces will develop cannot be predicted as manufacturing imperfections change from model to model. Advanced aircraft have the same problem and many of the available solutions have been obtained with aircraft applications in mind.

Proposed solutions fall into one of the two following groups (Champigny, 1994):

To use the asymmetric flowfield for flight control: This requires sophisticated data systems and data processing which are difficult to implement. Such systems do not affect the aerodynamics of the missile as there are no external appendages on the body of revolution.

To reduce or eliminate asymmetries in the flowfield, by forcing flow symmetry: Examples of such are forebody strakes. They are easier to implement on to a body of revolution but since they are external appendages the aerodynamics of the body of revolution will change.

1.2.1 Side force control

Much effort has been directed toward the development of ways by which the forebody flow separation could be controlled. The motivation of this has been to enhance the agility of advanced aircraft and missiles. Rao et al. (1987) used two deployable strakes on either side of a body of revolution to obtain a more gradual control. The strakes were pivoted along their length and deployed at command from their conformal stored position on the forebody. Two different strake deployments were studied by Rao et al. (1987):

Asymmetric deployment: Only one strake is deployed at a time, forcing a strong asymmetric vortex. This results in a side force, which is controllable by strake deflection.

Simultaneous deployment: Both strakes are deployed. A symmetrical pair of augmented vortices is established, from which a controlled sided force is generated by means of asymmetric strake deflection.

However, Rao et al. (1987) did not succeed in eliminating the nonlinear variation of side force with angle of attack. The side force control variation with body roll and sideslip is illustrated in Figure 1.4. When the strake is at a circumferential position (ϕ_s) of 90°, the strake forces flow separation which results in the indicated positive side force generation of flow model B. However at $\phi_s = 60°$, the pre-separation effect allows for reattachment of the boundary layer to withstand final separation well past $\phi = 90°$, resulting in a negative side force for flow model A.

For dual strake deployment, at $\phi_s = 90°/270°$, the left vortex is lifted up while the right vortex is drawn closer to the forebody. The asymmetric pressure distributions were very similar to that produced by the single strake at $\phi_s = 90°$ (Rao et al., 1987). While a single strake was effective in producing large yawing moments, the control was nonlinear and the strake was ineffective in eliminating the naturally occurring asymmetry and associated yawing moments at zero sideslip. Thus a pair of differentially deflectable strakes was more appropriate since it was able to address the above issues, but vortex asymmetry was not totally eliminated.

Ng and Malcolm (1992) showed that rotatable nose-tip strakes were able to produce controlled yawing moments, even at relatively moderate angles of attack. Effective control of vortex asymmetry could be obtained by controlling flow separation near the tip region. In this way the flow pattern is modified and the effective geometry of the tip is changed. The purpose of the rotatable nose-tip strakes is to influence

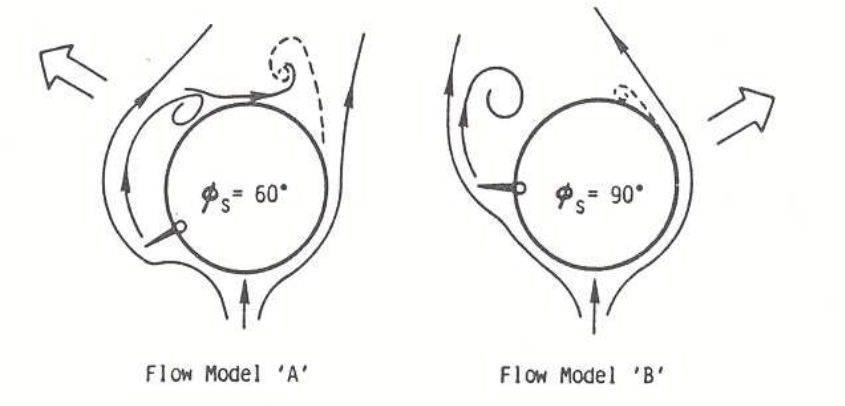


Figure 1.4: Suggested crossflow patterns generating opposite side forces for $\phi_s = 60°$ and $\phi_s = 90°$ (Rao et al., 1987)

only a small region near the tip of the forebody, whereas large strakes affect a much larger region aft of the tip. The rotatable nose-tip strakes function by creating, in effect, an asymmetric forebody apex.

Bernhardt and Williams (1998) introduced the idea of using unsteady bleed techniques for experiments to control the development of steady asymmetric vortices. The basic premise of the proportional control with unsteady bleed technique is that by controlling the initial flow disturbances at the tip, the configuration of the forebody vortices can be modified. The interaction of the unsteady bleed with the external flow produces a highly localised variable amplitude low pressure disturbance in the mean flow. This dominates the built-in geometric asymmetry of the cone and controls the formation of tip vortices. In addition to the role as actuators, the unsteady bleed technique enables the investigation of the important flow physics by studying the response of the flow to a controlled input. Bernhardt and Williams (1998) found that the most effective control of vortex configuration and side force is achieved by placing flow actuators near the tip of the forebody model.

Fidler (1981) rotated the nose-tip, nose and a portion of the body surface aft of the nose, to achieve cyclic variation of side force and yawing moment. These portions were rotated, first as smooth surfaces and then with artificial disturbances fixed to them. This allowed for the examination of small disturbances under controlled conditions. Increasing the spin rate of the nose and the nose tip resulted in a decrease in the maximum values of the sinusoidal side force variation. This was due to the vortices being unable to establish their flowfields quickly enough to produce the full effect on the body. Varying the number of artificial disturbances fixed to the nose and the nose-tip resulted in a change in the magnitude and sign of the side force. Fidler (1981) concluded that the spinning device concept would be successful

irrespective of the direction in which the body was pitched or yawed.

1.2.2 Side force alleviation

Early efforts to alleviate side force problems included various forms of geometric changes such as nose bluntness, strakes and boundary layer trips. Many investigations have focussed on jet blowing to obtain the same effect (Champigny, 1994).

Nose bluntness, which is an example of a passive flow control technique, can be an effective means of reducing the side force. However, it is possible that nose-induced asymmetry on a pointed nose body can be traded for an aft body asymmetry as surface geometric imperfections will still exist on the nose of the body of revolution. A small degree of nose bluntness delays the formation of steady asymmetric vortices on the nose, thus decreasing the induced side force. Eventually, as the nose bluntness is increased, vortex asymmetry begins on the cylindrical part of the body and that results in the formation of side force cells on the aft body (Ericsson and Reding, 1991).

A nose boom, added to the forebody, decreases the separation induced side force. The boom's multi-vortex wake effectively nullifies the asymmetry generating potential of a slender pointed nose (Ericsson and Reding, 1991). Ng (1992) found that the flow off a nose boom was very similar to that off a cylindrical, slender body. Initially, at moderate angles of attack, the flow separation is symmetric, but as the angle of attack increases, the separation becomes asymmetric. The asymmetric pattern, which is related to the number of separated asymmetric vortices and the strength of the asymmetric vortices, is not specific. The effect of the nose boom on the forebody is dependent on how the boom is fitted.

Ng (1992) also found that at moderate-to-high angles of attack, where the vortex pattern over the nose boom becomes asymmetric, the wake over the nose boom goes over small, naturally present perturbations on the body. This leads to an increase or decrease in forebody vortex asymmetry when the body is at zero-sideslip. At very high angles of attack, unsteady vortex shedding occurs over the nose and the nose boom wake flow is symmetric on a time-average basis. Nose booms are mainly used on the forebodies of fighter aircraft, operating at high angles of attack but not on missiles as it obstructs the missile seeker heads.

Ericsson and Reding (1991) provided evidence that helical body trips were more effective in reducing the side force, than straight body trips. These can be seen in

Figure 1.5. Unlike forebody strakes, body trips do not generate their own vortex. The body trip acts on the boundary layer over the forebody, thus its location relative to the natural separation line is crucial. It was shown that the straight boundary trips were efficient at supercritical flow conditions but at critical flow conditions, it generated close to maximum side force. The helical trips however, were able to alleviate the separation induced side force.

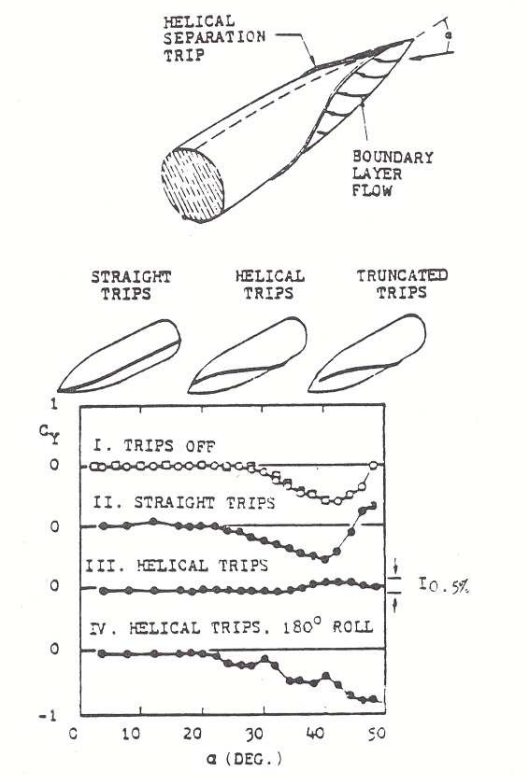


Figure 1.5: Effect of helical and straight body trips on side force of ogive-cylinder body (Ericsson and Reding, 1991)

Both Champigny (1994) and Ericsson and Reding (1991) have demonstrated that boundary layer blowing is effective at controlling forebody flow asymmetry. If blowing is tangential to the wall and upstream of the boundary layer separation, it re-energises the boundary layer, delaying separation. If it is performed under a vortex sheet it will modify the vortex position by entrainment. Champigny (1994) noted that keeping the flow symmetric at high angles of attack by means of blowing is difficult and it may be necessary to add forebody strakes. The most effective method of controlling forebody vortex flow is by using forebody strakes (Ng and Malcolm, 1992).

The use of a fixed pair of forebody strakes, attached symmetrically to the forebody has been effective in forcing steady asymmetric vortices at high angles of attack to become symmetric. In this way the large side forces and yawing moments are

significantly reduced (Ng and Malcolm, 1992).

Actively deployed forebody strakes are also a means of enhancing high angle of attack controllability (Ng and Malcolm, 1992). These strakes extended along the length of the forebody and were deflected at different angles of attack about a hinge line fixed along a meridian line. While a single strake was effective in producing large yawing moments, the control was nonlinear and the strake was ineffective in eliminating the steady asymmetry and associated yawing moments at zero sideslip.

Ericsson and Reding (1991) also noted that a single strake, a splitter-plate-fin, could be used to force vortex symmetry. From studies conducted by Ng (1990), it was found that the use of a single strake on the forebody drastically reduced the vortex asymmetry. The position of the strake was very critical. Ng (1990) showed that the flow near the apex was highly three-dimensional and had a strong influence on the axial flow. By reducing the interaction and entrainment between flows on the two sides, the flow asymmetry is not amplified downstream.

Yuan and Howard (1991) studied the effects of placing four strakes in the cruciform orientation and the effect of placing eight strakes symmetrically very close to the tip of the forebody of a missile. It was found that the four-strake configuration was more effective than the eight-strake configuration in reducing the yawing moments experienced by the body. However, the four-strake configuration was not able to reduce the yawing moments at the low angles of attack, since asymmetries formed on the aft body. At high angles of attack though, the induced side forces and yawing moments were virtually eliminated. The four strakes were orientated such that they were aligned with the horizontal and vertical planes of the body, the '+' configuration, and were able to force the forebody-generated vortices to become symmetrical.

1.3 Document Layout

The work is structured and presented as follows:

This chapter (Chapter one) provides a brief background into high angle of attack missile aerodynamics, a motivation as to why this research was carried out and the objectives of the study.

Chapter two validates the mesh, the position of the outlet boundary and the turbulence model used in this work. In Chapter two the similarity between results for a

full and half model are shown, which is used in Chapter three.

In Chapter three the effect of changing the missile strake span on the values of longitudinal aerodynamic coefficients is investigated.

Chapter four studies the creation of steady asymmetric vortices in CFD by placing a geometric perturbation on the missile nose. The iterative process followed in determining the effect of the size of the perturbation and the effect of the axial and circumferential positions of the geometric perturbation on the nose of the missile body are shown.

Chapter five investigates the effect of changing the span and axial positions of the strakelets on the steady asymmetric flowfield, created in Chapter four.

Chapter Six summarises the conclusions drawn from this work and makes some suggestions for future work.

1.4 Motivation

In 1993, aerodynamic work towards designing an agile, high angle of attack missile with very low aspect ratio wings and control tail fins, started at Denel. Four low aspect ratio wings, referred to as strakes, were orientated such that they were at 45° to the horizontal and vertical planes of the body ('×') and the four tail fins were orientated such that they were aligned with the horizontal and vertical planes ('+'). Initial wind tunnel tests were carried out in a high speed wind tunnel in 1995 and was followed by a medium speed wind tunnel test in 1996 (Gobey, 2004). Data obtained from both wind tunnel tests indicated that severe body and strake vortex interaction with the tail fins, in particular the large lateral disturbances or side forces, were as a result of steady asymmetric body vortices. The irregularity of the disturbances made the design of the missile flight control system very difficult.

The large magnitude of the lateral disturbances encountered at various roll orientations, even at moderate angles of attack were of particular interest. The strakes were re-orientated such that they were in-line with the tail fins. This alteration reduced the irregularity of the disturbances, but the magnitude of the side forces was still large and were subsequently attributed to geometric imperfections on the missile nose (Gobey, 2004).

The following problematic areas needed to be addressed so that the missile's aerodynamic performance could be improved:

- Improve the aerodynamics of the missile strakes when in the '×' orientation
- Reduce lateral disturbances by employing four miniature strakes on the forebody of the missile. The miniature strakes are referred to as strakelets.

1.5 Objectives

The objectives of the study are:

- To investigate the effect of increasing the strake span on normal force when the strakes are orientated in the '×' configuration.
- To model a steady asymmetric flowfield on a missile body at high angles of attack in CFD.
- To investigate the effect of changing the span and axial position of strakelets to alleviate the steady vortex asymmetry around a generic missile body.

2 Validation Studies

Validation studies were carried out in the following areas of importance:

- Mesh size sensitivity
- Outlet boundary position
- Half symmetry
- Turbulence models

2.1 Mesh Size Sensitivity

All computational fluid dynamics (CFD) models require appropriate grids, with sufficient grid density in regions of high flow gradients. The problem lies in determining where these critical regions exist. In a vortical flowfield, high flow gradient regions exist in the boundary layer, regions of shear layer separation and the primary and secondary vortices.

A grid resolution study was performed to minimise the error induced by the spatial resolution of the mesh. In order to validate the chosen mesh size, the number of grid points in the circumferential, radial and axial directions were first halved and then doubled. The results obtained from these two simulations were then compared to that of the original mesh.

The three models that were used in the mesh sensitivity study are identified as follows:

- Model A : Model with the number of grid points halved in each direction.
- Model B : Model with the number of grid points doubled in each direction.
- Model C : The grid that has been used for the bulk of this study

2.1.1 Grid generation

A portion of the missile body was modelled for the mesh sensitivity study. The chosen geometry, shown in Figure 2.1, had a length of 3.8D, where D is the body diameter.

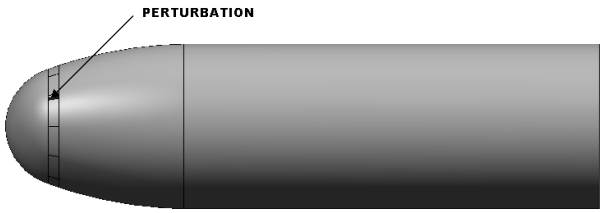


Figure 2.1: A portion of the missile body geometry

The geometric perturbation on the nose of the missile body acts as trigger for the formation of steady asymmetric vortices. It's purpose is further discussed in Chapter 4.

All meshes in this study were constructed in CFD-GEOM, which is the grid generator for CFD-FASTRAN. Structured grids were created on the geometries. Thomas and Hartwich (1991) found that the structured grid approach leads to the most efficient algorithms for treating viscous flows, because the grid cells can be highly stretched in the direction normal to the developing shear layers.

The height of the first cell perpendicular to the body surface is dependent on the the turbulence model used. The Menter-Shear Stress Transport (SST) $k-\omega$ turbulence model that has been used in this study, is implemented in CFD-FASTRAN without the use of wall functions[1]. Therefore the height of the first cell perpendicular to the body had to be 10 μm away from the body so that y^+ values of 1 were obtained on the body surface. The height of the first cell was calculated from Equation 2.1 (CFDRC, 2003).

$$y^+ = \frac{u_\tau y}{\nu} \tag{2.1}$$

where:

- u_τ is the friction velocity (m/s),
- y is the distance from the surface in the boundary layer (m),
- ν is the kinematic molecular viscosity = $\frac{\mu}{\rho}$ (m^2/s),
- μ is the molecular viscosity (kg/ms), and
- ρ is the density (kg/m^3)

The mesh domain used in this study is shown in Figures 2.2 and 2.3.

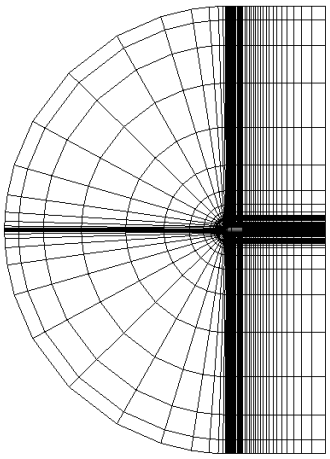


Figure 2.2: Structured grid used in this study

[1]Wall functions bridge the extremely thin viscous layer near the surface. In order to adequately resolve the turbulent portion of the boundary layer, at least 8-10 points are required in the turbulent regime (ERCOFTAC, 2000)

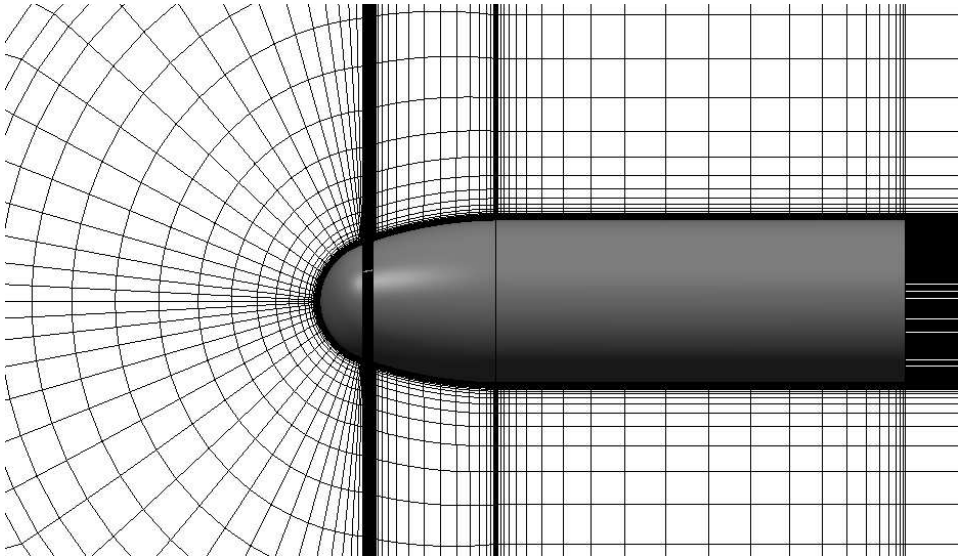


Figure 2.3: A closer view of the structured grid around the body surface shown in Figure 2.2

The grid shown in Figure 2.2 consisted of 272 equispaced circumferential points extending completely around the body, which was maintained radially out to the farfield, boundary 52 radial points between the body surface and the computational outer boundary and 90 axial points between the nose tip and the end of the body. This grid was very similar to that created by Degani (1992) and it was found to capture important flow characteristics (Degani, 1992). The first cell of the grids for model A and B's grids were also 10 μm high, ensuring that a y^+ value of 1 was obtained on the body surface.

The grid used for model A comprised of 136 circumferential points, 26 radial points and 45 axial points. The grid constructed on Model B consisted of 542 circumferential points, 104 radial points and 180 axial points.

Figure 2.2 shows grid cells concentrated close to the body. Since viscous flows over slender body configurations are dominated by separated vortical flows, placing a high density of grid cells close to the body surface allows these flow characteristics to be captured. The flow at the farfield boundaries, located 15 body lengths away from the body surface, is not of interest and thus larger aspect ratio cells are present in that region.

Simulations were carried out at the following flight conditions:

- Freestream Mach number (M_∞) = 0.8
- Static Pressure (P) = 101.325 kPa
- Static Temperature (T) = 288 K
- Reynolds number = 3×10^6

The values of the turbulent kinetic energy (k) and the specific dissipation rate of kinetic energy (ω) are determined from Equations 2.2 and 2.4 (CFDRC, 2003).

$$k = \frac{{u_\tau}^2}{\sqrt{C_\mu}} \tag{2.2}$$

$$\epsilon = \frac{C_\mu^{\frac{3}{4}} k^{\frac{3}{2}}}{\kappa y} \tag{2.3}$$

$$\omega = \frac{k}{\epsilon} \tag{2.4}$$

where

- C_μ is the closure constant,
- κ is the von Kàrmàn's constant, and
- ϵ is the dissipation rate of kinetic energy (J/kgs).

The values of k and ω used were 3.703 m^2/s^2 and 5674.2 s^{-1} respectively.

The mesh sensitivity study was only carried out at an angle of attack of 40°, since many of the simulations in this study were carried out at this angle of attack.

The boundaries situated in the farfield were specified as Inflow-Outflow boundaries and were set at freestream conditions since they were located sufficiently far from the body (Thomas and Hartwich, 1991).

The farfield outlet boundary was placed approximately 5 body lengths away from the base of the missile. In Section 1.2, the effect of the outlet boundary position

is discussed and it is shown that placing the outlet boundary 5 body lengths away from the body base is sufficient since the flow on the nose of the missile body is of interest and the objective of this study is to qualitatively investigate the effects of the steady asymmetric flowfield observed experimentally. The outlet boundary was not placed at the missile base, as simulations were carried out at subsonic Mach numbers and placing the outlet at the base would force a constant pressure solution across the wake which is not physically possible.

The Roe's Flux Differencing Splitting (FDS) scheme was used in conjunction with the Osher-Chakravarthy (Osher-C) flux limiter to solve the Reynolds Averaged Navier-Stokes (RANS) equations (CFDRC, 2003). The Roe's FDS scheme is more accurate for separated flows than the Van Leer Flux Vector Splitting (FVS), which is the other spatial difference scheme implemented in CFD-FASTRAN (Thomas and Hartwich, 1991). High angle of attack flow, at subsonic and transonic Mach numbers, is characterised by large regions of separation and no shocks are present, thus allowing for the use of Roe's FDS with the Osher-C flux limiter.

The initial conditions were set to the previously defined freestream conditions and are applicable to all simulations in this study. Since the solution algorithms, for both unsteady and steady flows, require inputs for boundary and initial conditions, they are considered to be time-marching algorithms. The initial conditions, when set to freestream conditions, correspond to an impulsive start (Thomas and Hartwich, 1991).

All simulations were run on a Boxx-Dual-Opteron. Each processor had 2Gb of RAM. The simulations were deemed converged once the forces acting on the modelled geometry reached a steady state value. The convergence of the normal force is shown in Figure 2.4.

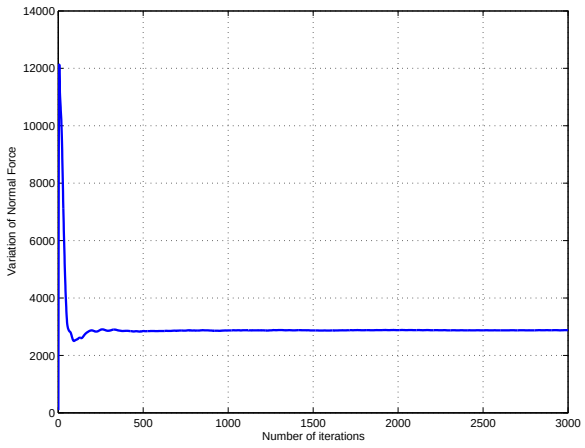
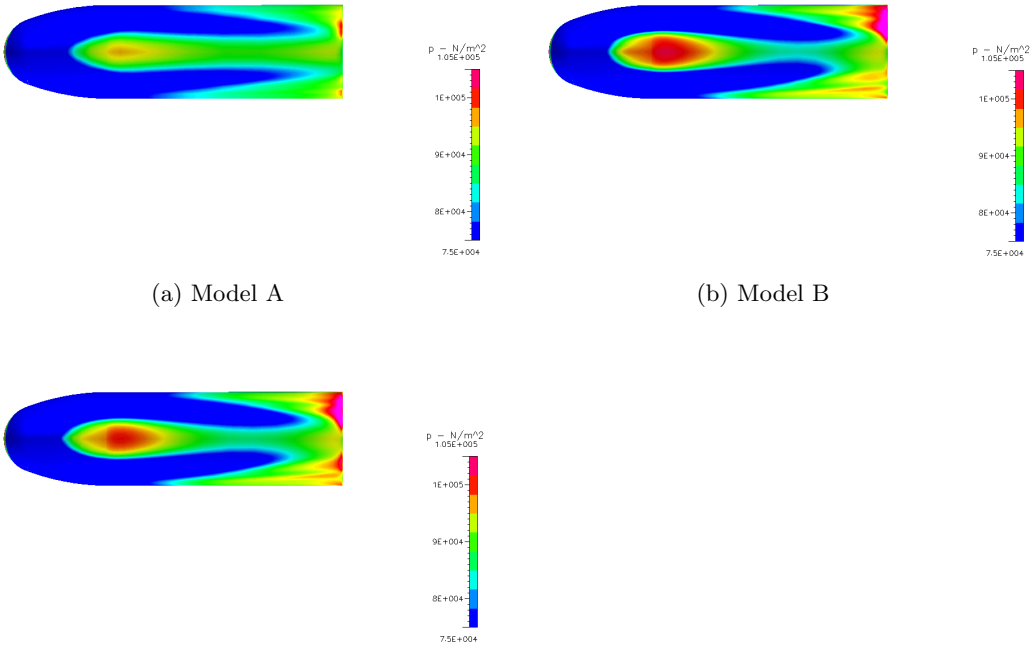


Figure 2.4: Change in normal force per iteration

2.1.2 Results

Figure 2.5 shows the surface pressure distribution on the geometries for the different grids.



(a) Model A

(b) Model B

(c) Model C

Figure 2.5: Surface pressure distribution on the three models with different grids at $\alpha = 40°$

From Figure 2.5, it can be seen that the surface pressure distributions for models B and C are very similar, while model A fails to capture certain critical characteristics that are captured by models B and C. Model A has not captured the high pressure region at the centre of the missile body, which is seen in Figures 2.5b and 2.5c. The high pressure region on model B in Figure 2.5b is larger than that on model C in Figure 2.5c since model B had more grid points than model C. This high pressure region is due to the counter-rotating separated vortices.

Models B and C show that the low pressure regions on the nose of the missile, indicated by the blue region, are asymmetric. The asymmetry is due to the formed vortices separating at different axial positions on the body as a result of the geometric perturbation on the nose triggering vortices of different strengths. Due to the coarse grid on model A, this asymmetry is not captured, as shown in Figure 2.5a. The symmetric, low pressure regions on model A indicate that the vortices separated at the same axial position on the body, that is the effect of the geometric perturbation

is not captured.

At the rear of the geometry, the large high pressure regions shown in Figures 2.5b and 2.5c for models B and C are not visible in Figure 2.5a. The high pressure region at the rear of model B is larger than that on model C.

The surface pressure distributions, $0.06D$ on either side of the body centre-line, are shown in Figures 2.6 and 2.7.

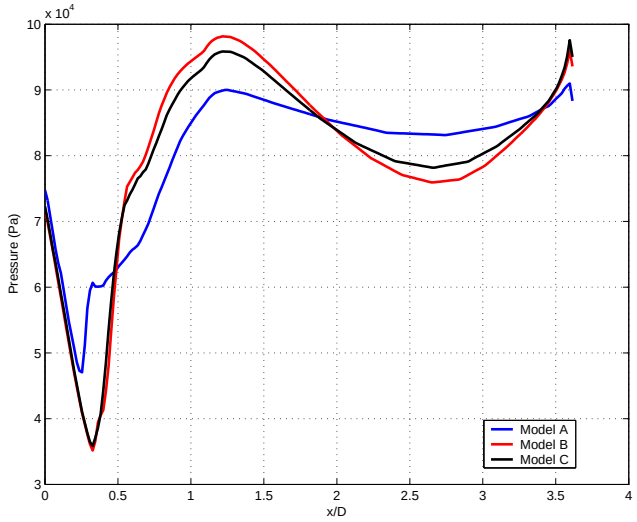


Figure 2.6: Comparison of surface pressure distribution along length of body (left of the body centre-line)

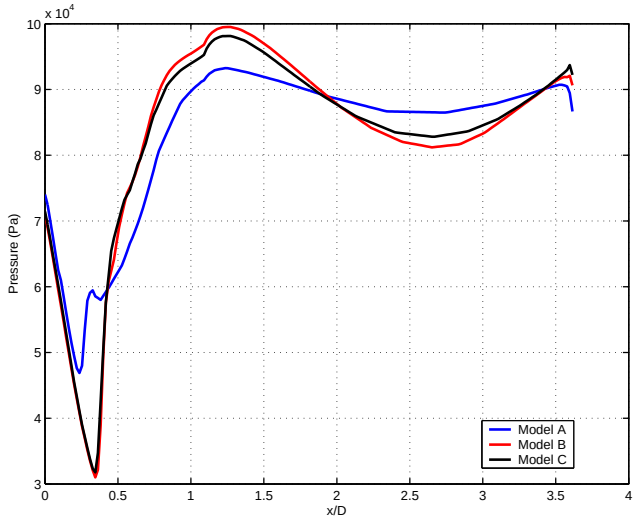


Figure 2.7: Comparison of surface pressure distribution along length of body (right of the body centre-line)

Figures 2.6 and 2.7 are numerical representations of Figure 2.5. The pressure distribution trend, displayed by all three models is very similar. However, the peak surface pressure on model A is significantly lower than the peak surface pressures on models B and C. The difference in the surface pressure distributions on model B and C is very small, even though model B has eight times the overall number of grid cells in the three directions.

Helicity density plots

Levy et al. (1990) found that scalar quantities such as pressure and density were insufficient in describing vortex formation and development. While these quantities could identify the cores of concentrated primary vortices in high-speed flows, they could not identify low-speed phenomena such as secondary vortices or diffused vortices. Another major shortfall was that these quantities could not identify the sense of swirl of the vortices, thus the difference between primary and secondary vortices could not be distinguished.

Levy et al. (1990) found that helicity density was able to:

- identify vortices,
- distinguish between primary and secondary vortices, and
- indicate the direction of the swirling motion

Helicity density is defined as the dot product between the velocity vector and the vorticity vector (Levy et al., 1990):

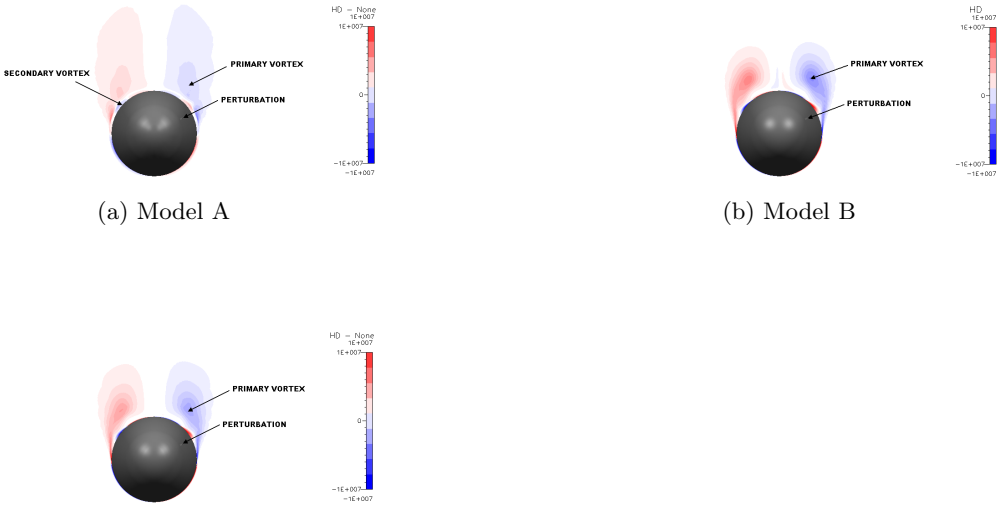
$$H_d = \mathbf{V} \cdot \omega \tag{2.5}$$

Even though helicity density is a scalar, both its sign and magnitude are meaningful. High magnitudes of helicity density reflect high values of speed and vorticity when the relative angle between the two vector strengths is small. The sign of helicity density, which is determined by the cosine of the angle between the velocity and vorticity vectors, indicates the direction of the swirl of the vortex relative to the streamwise velocity component.

Helical density may be graphically displayed, using colour graduation for magnitude and different colours for different signs in a two colour flood plot. This allows primary and secondary vortices to be clearly distinguished (Levy et al., 1990).

The use of helicity density to indicate vortices in low subsonic flows and at low angles of attack is needed as neither density nor pressure mapping are sufficiently sensitive to the changes in density or pressure variations that are a small percentage of full scale in such flowfields. The sensitivity of helicity density always remains high in the vortex region because in this region both velocity and vorticity are high and the angle between the two vectors are small. Therefore helicity density is a better representation of vortices than density mapping, giving a clear representation of both strength and direction.

Helicity density contour plots, showing the separation of vortices at two locations along the length of the body, are illustrated in Figures 2.8 and 2.9.



(a) Model A

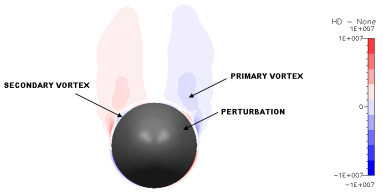
(b) Model B

(c) Model C

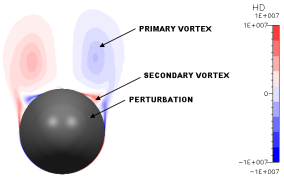
Figure 2.8: Helicity density contours at $x = 2.5D$ at $\alpha = 40°$

Figure 2.8 shows the formation of primary vortices on the missile body. The shades of blue indicate counter-clockwise rotation, with the darkest shade of blue indicating maximum vortex strength and lightest shade of blue indicating the minimum vortex strength. The shades of red indicate clockwise vorticity. The darkest shade of red indicates maximum vortex strength and the lightest shade of red indicates the minimum.

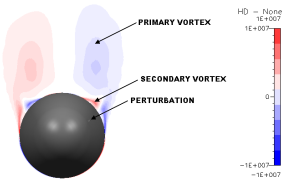
The shear layer on the sides of the missile body, that feeds into the formed vortices for models B and C, shown in Figures 2.8b and 2.8c, are smeared in 2.8a, due to the coarse grid on model A. Two well defined primary vortices, are formed for models B and C. The vortices formed for model A, show that a set of primary vortices have formed but they are not well defined. The vortex cores in model A are not captured as well as they are captured in models B and C.



(a) Model A



(b) Model B

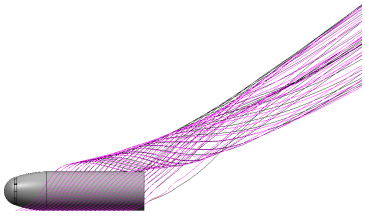


(c) Model C

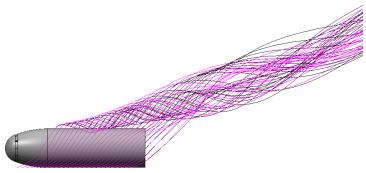
Figure 2.9: Helical density contours at $x = 3.5D$ at $\alpha = 40°$

The formation of secondary vortices, rotating in the opposite direction to their associated primary vortices can be clearly seen in Models B and C, while that displayed for model A are not well defined. Model B and C show the strength of the secondary vortices.

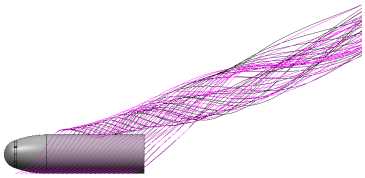
Ribbon traces were plotted on the body so as to show the vortex trajectories off the surface of the body. This is shown in Figure 2.10



(a) Model A



(b) Model B



(c) Model C

Figure 2.10: Streamlines off the surface of the missile at $\alpha = 40°$

Model A, due to the fewer grid cells is unable to show the spiraling of the ribbon traces, that models B and C are able to predict. Models B and C also show that the vortices have separated from the body.

2.1.3 Discussion

Figures 2.5 to 2.7 show that the mesh of model A, predicts significantly different surface pressure distributions to that of models B and C due to the coarser mesh. The high surface pressure distribution, which is captured by models B and C, shown in Figures 2.6 and 2.7, is not captured by model A. Model A predicts a surface pressure distribution that is approximately 37% less than that predicted by models B and C.

At axial locations of $x = 2.5D$ and $x = 3.5D$, model A is unable to adequately capture the formation of the primary and secondary vortices. The ribbon plots in Figure 2.10 show that model A is unable to predict flow swirl.

The failure of model A to capture regions of high pressure distribution and the strengths of the primary and secondary vortices shows that by using a grid with too few grid cells, important flow features are not captured.

Figures 2.6 and 2.7 show similar surface pressures on models B and C. By increasing

the number of grid cells, the increase in surface pressures is approximately 2% at $x = 2.5D$ and approximately 3% at $x = 2.8D$. Thus by using a grid with almost half the density of cells, an answer of sufficient accuracy can be obtained. The improvement in result quality due to an increase in mesh size for model B does not warrant the computational expense of running at the higher resolution.

2.2 Outlet Boundary Position

In order to set the outlet boundary at atmospheric pressure, the outlet boundary has to be placed sufficiently far from the base of the body, so that it has no influence or a very weak influence on the upstream flow (ERCOFTAC, 2000).

2.2.1 Grid generation

The geometry of Figure 2.2 was modified and the outlet boundary was placed approximately 5 body lengths away from the base of missile body. This decision was based on the fact that the region of interest was the flow on the nose of the missile. In order to check if this position was suitable, the outlet boundary was moved such that it was 20 body lengths away from the base of the missile. This distance was suggested by CFDRC (2003).

The structured grid used for the second model was that of Figure 2.2. However, the number of grid points in the outlet region was increased to 40.

This study was carried out at an angle of attack of 40° only.

2.2.2 Results

Figure 2.11 shows the surface pressure distribution along the top surface of the missile body and the distance from the base of the missile to the outlet boundary. The pressure trace was placed on the body centre-line.

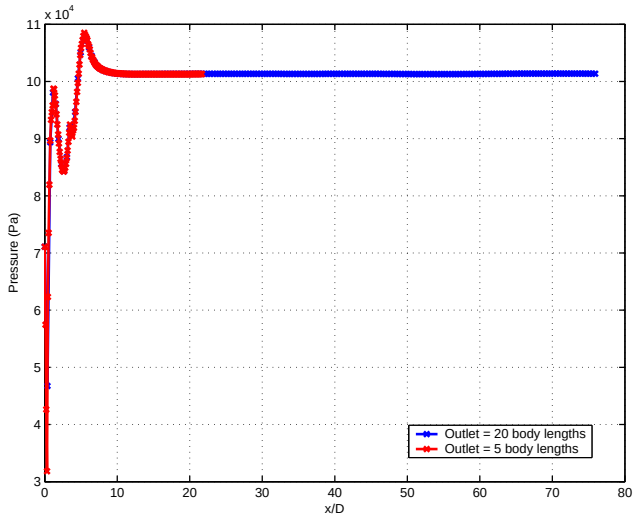


Figure 2.11: Comparison of the pressure distribution for the two outlet positions

Figure 2.11 shows no difference in the pressure distributions along the length of the body and both models predict the same value for pressure distribution at the outlet boundary. A closer view of the surface pressure distribution near the missile nose in Figure 2.12 shows different peak values for the two different models. However, this difference is small enough to be considered negligible.

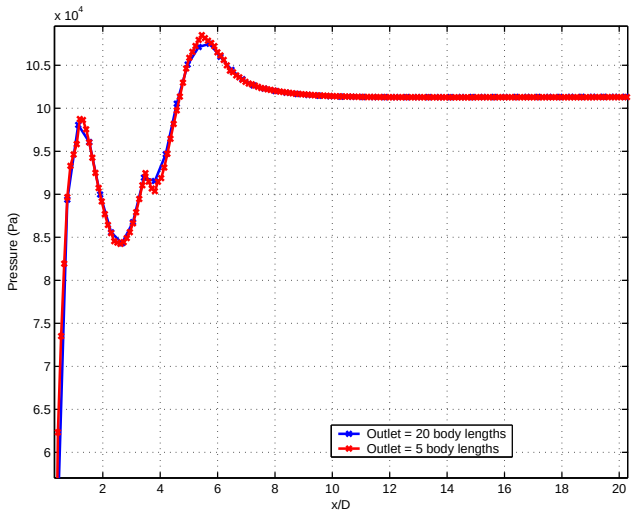
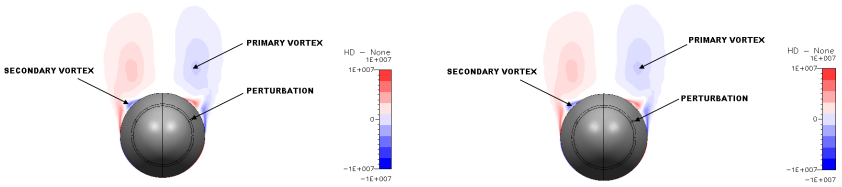


Figure 2.12: Closer view of the surface pressure distribution near the missile nose for the two outlet positions.

Figure 2.13b shows the formation of primary and secondary vortices on the missile body at $x = 3.5D$. The vortex formation for both outlet boundary positions look identical.



(a) Model A (b) Model B

Figure 2.13: Helical density contours at $x = 3.5D$ at $\alpha = 40°$

Figures 2.11 and 2.12 show that the position of the outlet boundary has had a negligible effect on the surface pressure distribution on the upper surface of the missile body, while Figure 2.13 shows no change in vortex formation.

The study is primarily concerned with flow on the nose of the missile and its interaction with the strakelets as well as qualitatively reproducing steady asymmetric vortices. Thus placing the outlet boundary 5 body lengths from the base of the missile should not have a significant influence on the flow at the nose. This is seen in Figure 2.13, where the outlet boundary position has had no visible effect on the formation of primary and secondary vortices. The outlet boundary can thus be left at 5 body lengths from the rear of the missile.

2.3 Comparison Between Full Model and Half Model Simulations

For symmetric flowfields it is possible to model only a portion of the geometry to obtain a solution which is representative of the whole geometry. The advantage of modelling a portion of the geometry is that the number of grid points and thus the size of the overall mesh is reduced. In this way the computational time required to obtain a reasonably accurate solution is also reduced. An investigation was undertaken to determine if the normal force and pitching moment coefficients obtained from a full model simulation and a half model simulation would be similar. This would justify the use of a half model for further symmetric flowfield simulations.

2.3.1 Grid generation

The geometry shown in Figure 2.14 was analysed. The length of the missile body was $18D$ and the aspect ratio[2] of the strakes on the body was 3.7×10^{-3}.



Figure 2.14: Full geometry of missile body

Since the flowfield is symmetric about the vertical plane, only one half of the model was created in CFD-GEOM. A portion of the structured grid, created on the half model, is shown in Figure 2.15.

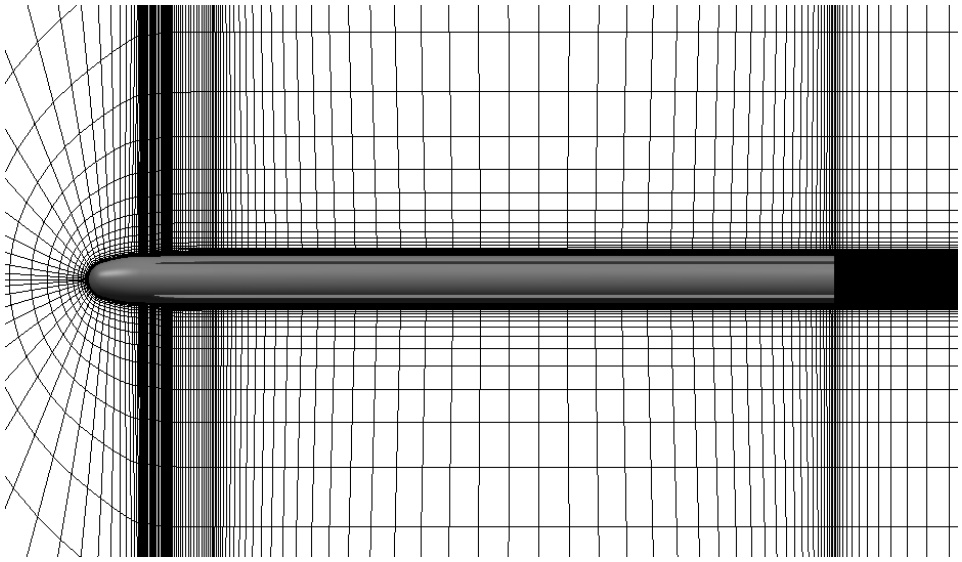


Figure 2.15: A closer view of the grid constructed on the half model

For the half model a symmetry plane was set. The half model grid consisted of approximately 1.2 million grid cells. For the full model the half model was mirrored

[2]ratio of strake span to strake chord

about its symmetry axis and the symmetry boundary was removed. Simulations were carried out at angles of attack from 0° to 50° in increments of 10° at the flight conditions specified in Section 2.1. The Menter-SST $k-\omega$ turbulence model was used. The values used for k and ω were 3.703 m^2/s^2 and 5674.2 s^{-1} respectively. The spatial numerical method used was Roe's FDS, together with the Osher-C flux limiter to solve the Reynolds averaged form of the Navier-Stokes equations.

2.3.2 Results

The normal force coefficient (C_N) and pitching moment coefficient (C_m) for the full model were calculated from Equations 2.6 and 2.7:

$$C_N = \frac{N}{0.5\rho V^2 S_{ref}} \tag{2.6}$$

$$C_m = \frac{M_z}{0.5\rho V^2 S_{ref} l_{ref}} \tag{2.7}$$

where:

- N is the normal force (N),
- M_z is the pitching moment about the z-axis (N.m),
- ρ is the density = 1.225 kg/m^3,
- V = 272.14 m/s at Mach = 0.8,
- S_{ref} is the cross-sectional area = $\frac{\pi D^2}{4}$ (m^2), and
- l_{ref} is the reference length = D (m)

The percentage difference in the values obtained for the normal force and pitching moment coefficients, calculated from Equations 2.8 and 2.9, are shown in Table 2.1. The actual values obtained for the two models are shown in Figures 2.16 and 2.17.

$$\%\Delta C_N = \frac{C_{NFull} - C_{NHalf}}{C_{NFull}} \times 100 \tag{2.8}$$

$$\%\Delta C_N = \frac{C_{mFull} - C_{mHalf}}{C_{mFull}} \times 100 \tag{2.9}$$

where:

- C_{NFull} is the normal force coefficient for the full model
- C_{NHalf} is the normal force coefficient for the half model
- C_{mFull} is the pitching moment coefficient for the full model
- C_{mHalf} is the pitching moment coefficient for the half model

Table 2.1: Percentage difference in the normal force and pitching moment coefficients between the full and half symmetry models

α **(deg)**	$\%\Delta C_N$	$\%\Delta C_m$
0	0.000	0.000
10	4.957	1.346
20	4.494	3.420
30	2.379	0.8610
40	1.361	0.0310
50	0.1340	1.343

Figures 2.16 and 2.17 are comparisons of the normal force coefficient and pitching moment coefficients respectively.

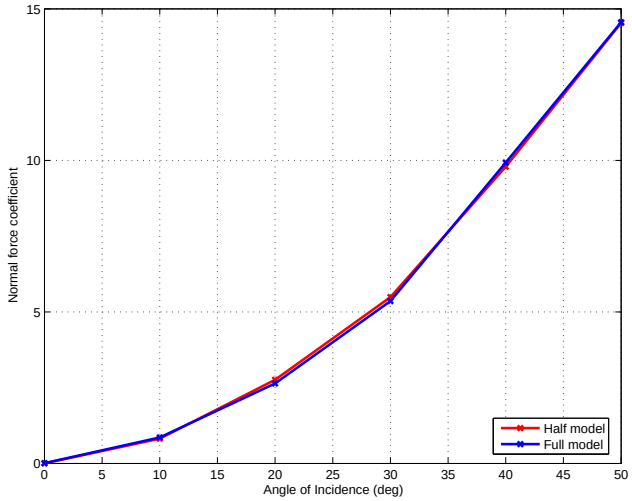


Figure 2.16: Comparison of values of of the normal force coefficients for the half and full models

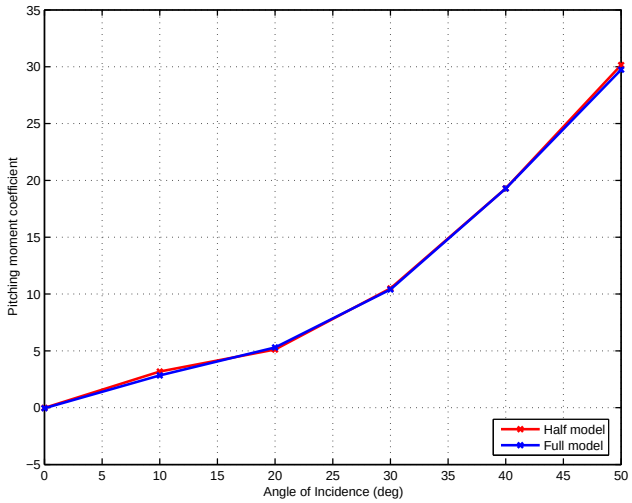
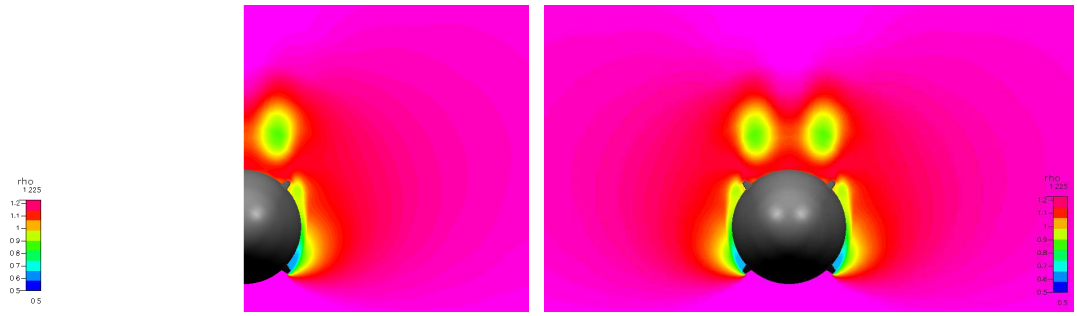


Figure 2.17: Comparison of values of the pitching moment coefficients for the half and full models

Figures 2.16 and 2.17 show that there is very little difference in the values of the normal force and pitching moment coefficients, obtained from the full and half symmetry model simulations.

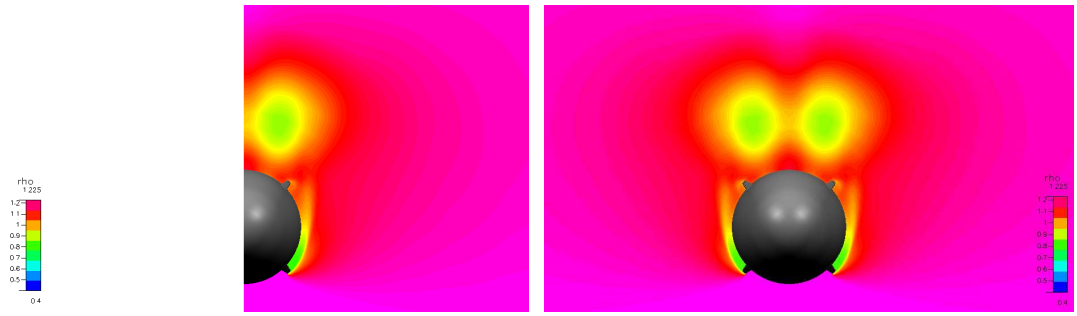
Figures 2.18 and 2.19 show the flow development on the two models at axial locations of $0.31D$ and $6.3D$.



(a) Half model (b) Full model

Figure 2.18: Density contours at $x = 0.31D$ at an angle of attack of 40°

The vortex formed in Figure 2.18a is very similar to the vortices in Figure 2.18b. The vortices shown in Figure 2.18b are the same height above the body. This vortex height is captured by the half model in Figure 2.18a as well.



(a) Half model (b) Full model

Figure 2.19: Density contours at $x = 6.3D$ at an angle of attack of 40°

In Figure 2.19 flow separation occurs on both sides of the body, at the top strakes. This flow separation is also captured by the half model in Figure 2.19a. The flowfields on both halves of the body in Figure 2.19b are identical, indicating that the flowfield is symmetrical.

2.3.3 Discussion

Table 2.1 and Figures 2.16 and 2.17 show that the values for the normal force and pitching moment coefficients from a half model simulation correlate very well with the values obtained from a full model simulation. The maximum percentage difference obtained is approximately 5% at an angle of attack of 10° for the normal force coefficient and 3.4% for the pitching moment coefficient at 20° angle of attack. These differences are acceptable when weighed against the computational time saved.

Figures 2.18 and 2.19 show that important characteristics such as vortex formation and flow separation is captured even if a half model simulation is carried out. The flowfields in Figures 2.18b and 2.19b show that the flowfields on both halves of the body are identical, indicating that no asymmetries exist in the flowfield. This shows that for a perfectly symmetrical body it is possible to model only half of the body and important flow characteristics will be captured. However, if a time-accurate simulation or asymmetrical flowfield is to be modelled, a full model of the geometry must be used. It is possible that for a time-accurate simulation, the flow might not develop symmetrically (if perturbed) and for an asymmetrical model, the flow on either sides of the model is not identical.

2.4 Turbulence models

Turbulence is one of the key phenomena in fluid dynamics. There are various techniques for the numerical prediction of turbulent flows ranging from the Reynolds Averaged Navier-Stokes (RANS), large eddy simulation (LES) and direct numerical simulation (DNS) (Cummings et al., 2003). DNS attempts to resolve all scales of turbulence from the largest to the smallest by solving the Navier-Stokes equations directly. LES attempts to model the smaller, more homogenous scales, while resolving the larger energy containing scales, thus making grid refinement for LES less than that for DNS. For the RANS approach , the equations have been averaged over a time-scale, which is small in relation to the aerodynamic time-scale but large in comparison to the time-scale of the turbulent eddies (Thomas and Hartwich, 1991).

The RANS approach attempts to solve the time-averaged flow, which means that all scales of turbulence must be modelled.

Turbulence models are semi-empirical formulations that are used to close the RANS equations by approximating the Reynolds stress terms (Cummings et al., 2003). They are generally calibrated on building block flows such as boundary layers, shear layers and wakes. Reynolds stresses are modelled in two ways, namely eddy viscosity models and shear stress transport models (Cummings et al., 2003).

Shear stress transport models make no general assumptions about the form of the six components of the Reynolds stress model and unless assumptions have been made, the turbulence model solves for all six unknowns. The more common eddy viscosity models are based on Boussineq's approximation that the Reynolds stresses are directly proportional to the local strain rate of flow. This assumption reduces the number of unknowns from six to a single unknown which is the turbulent eddy viscosity term (Wilcox, 2000).

Most common are zero-, one- and two-equation turbulence models. The zero-equation turbulence models use algebraic relations rather than partial differential equations. The zero-equation turbulence models avoid the necessity of finding the edge of the boundary layer and employ a purely algebraic modelling of the eddy viscosity. The simplicity of the zero-equation turbulence model allows for good computational efficiency but their applicability is limited. The more complex one- and two-equation models are aimed at more closely mimicking the physics of turbulent flows. These models assume that the eddy viscosity is a function of a turbulence length and velocity scale. The two-equation models use two partial differential equations to compute the velocity and length scales. The one-equation models compute

the velocity scales via a partial differential equation but algebraically evaluate the turbulence length scale (Wilcox, 2000).

A major challenge in aerodynamic design is the accuracy of turbulence models for simulations of complex turbulent flows for example high angle of attack flows (Bardina et al., 1997). Development of improved turbulence models has increased in the last decade due to the technological requirements of present aerodynamic systems, aided by advances in computers and numerical simulation capabilities. A variety of researchers have proposed methods for adapting algebraic turbulence models for high angles of attack. Degani and Schiff (1991) proposed a modification to the Baldwin-Lomax model, an eddy viscosity turbulence model, that predicted flow reasonably accurately in the separated flow region.

In this study, while the flow separation and the formation of steady asymmetric vortices are important, it is the interaction of the steady asymmetric vortices with surfaces on the slender body that is of primary importance.

Five different turbulence models are available for use in CFD-FASTRAN, namely the Baldwin-Lomax model, the standard $k-\epsilon$ (Launder-Spalding) model, the $k-\omega$ (Wilcox) model, the Spallart-Allmaras model and the Menter-SST $k-\omega$ model.

The standard $k-\epsilon$ turbulence model is a two-equation eddy viscosity model for incompressible and compressible turbulent flows. It is a high Reynolds number model and is not meant to be used in the near wall regions were viscous effects are greater that the effects of turbulence (Bardina et al., 1997). The standard k-ϵ turbulence model has been implemented in CFD-FASTRAN by means of wall functions.(CFDRC, 2003)

The Menter-SST $k-\omega$ turbulence model is also a two-equation eddy viscosity model. The Menter-SST turbulence model is a combination of the standard $k-\epsilon$ turbulence model and Wilcox's $k-\omega$ turbulence model. It uses the $k-\omega$ model near solid walls and the standard $k-\epsilon$ turbulence model near the boundary layer edges.

The Spalart-Allmaras turbulence model is a one-equation model, based on the transport eddy viscosity and was designed for aerospace applications. It predicts flow separation very well, (Bardina et al., 1997), but was not used in this study, because it has not been properly implemented in CFD-FASTRAN.

The LES turbulence model was formulated for solving unsteady cyclic and vortical flows and should be chosen for modelling steady asymmetric vortex flow. The LES turbulence model was not implemented in CFD-FASTRAN at the time the study

was conducted.

The Menter-SST $k-\omega$ turbulence model and the standard $k-\epsilon$ turbulence model were used in this investigation to determine which turbulence model would provide acceptable results for complex high angle of attack flows. Although Bardina et al. (1997) and Menter (2003) have shown that the standard $k-\epsilon$ turbulence model does not fair well in separated flows, the shortfall of the standard $k-\epsilon$ turbulence model would be investigated alongside the Menter-SST $k-\omega$ turbulence model.

2.4.1 Grid generation

In Section 2.3, it was seen that it was sufficient to model only half of a symmetrical model as all important flow field characteristics were captured with the half model simulation. Therefore only half the missile body shown in Figure 2.14 was modelled in CFD-GEOM.

Two different grids had to be constructed since y^+ values of between 30 to 100 were required for the standard $k-\epsilon$ turbulence model and y^+ values equal to 1 were required by the Menter-SST $k-\omega$ turbulence model (CFDRC, 2003). To ensure that these values of y^+ were obtained, the height of the first cell perpendicular to the body surface had to be approximately 0.5 mm and 10 μm for the standard $k-\epsilon$ turbulence model and Menter-SST turbulence models respectively.

A structured grid, such as that shown in Figure 2.15 was constructed on the body surface. The grid for the standard $k-\epsilon$ turbulence model consisted of 146 circumferential grid points, 55 radial grid points and 150 axial grid points. The number of radial grid points had to be increased for the Menter-SST $k-\omega$ turbulence grid as more points were required closer to the body surface.

As with the half symmetry study, the investigation was carried out at the flight conditions specified in Section 2.1 at angles of attack from 0° to 50° in increments of 10°. Roe's FDS was the spatial numerical method used, together with Osher-C flux limiter, to solve the RANS equations (CFDRC, 2003).

2.4.2 Results

The values for the normal force and pitching moment coefficients were determined from Equations 2.6 and 2.7. The percentage difference in normal force and pitching

moment coefficients were calculated from Equations 2.10 and 2.11 and are shown in Table 2.2.

$$\%\Delta C_N = \frac{C_{NSST} - C_{Nk-\epsilon}}{C_{NSST}} \times 100 \tag{2.10}$$

$$\%\Delta C_N = \frac{C_{mSST} - C_{mk-\epsilon}}{C_{mSST}} \times 100 \tag{2.11}$$

where:

- C_{NSST} is the normal force coefficient for the Menter-SST $k-\omega$ turbulence model
- $C_{Nk-\epsilon}$ is the normal force coefficient for the standard $k-\epsilon$ turbulence model
- C_{mSST} is the pitching moment coefficient for the Menter-SST $k-\omega$ turbulence model
- $C_{mk-\epsilon}$ is the pitching moment coefficient for the standard $k-\epsilon$ turbulence model

Table 2.2: Percentage difference in normal force and pitching moment coefficients between the two turbulence models

α **(deg)**	$\%\Delta C_N$	$\%\Delta C_m$
0	0.000	0.000
10	1.120	0.4800
20	18.13	10.56
30	21.32	6.680
40	15.84	10.73
50	12.61	10.02

Table 2.2 indicates that the percentage difference in the values of obtained for the normal force and pitching moment coefficients for the two turbulence models at 10° angle of attack are low. However, at the higher angles of attack, a significant difference exists between the coefficients obtained from the two turbulence models.

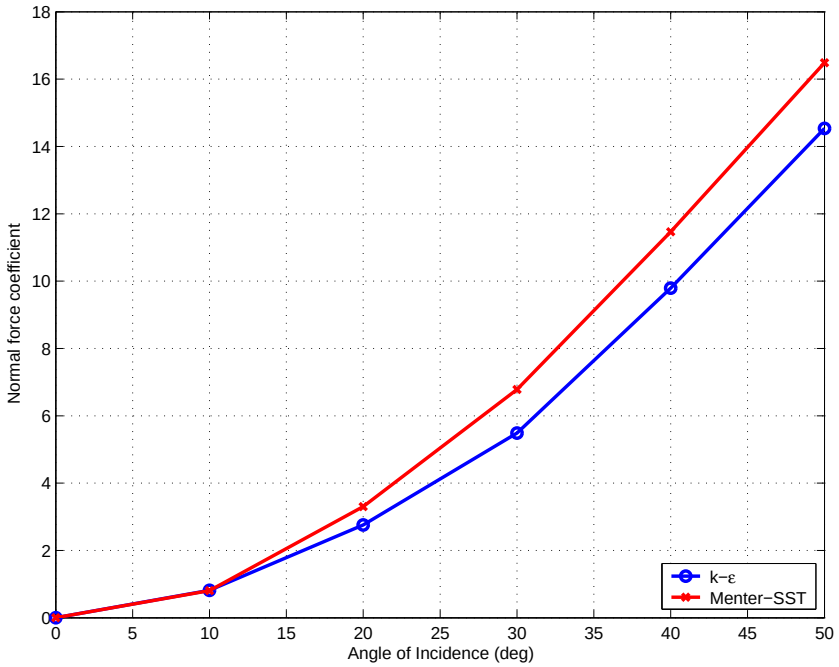


Figure 2.20: Comparison of values of the normal force coefficients for the two turbulence models

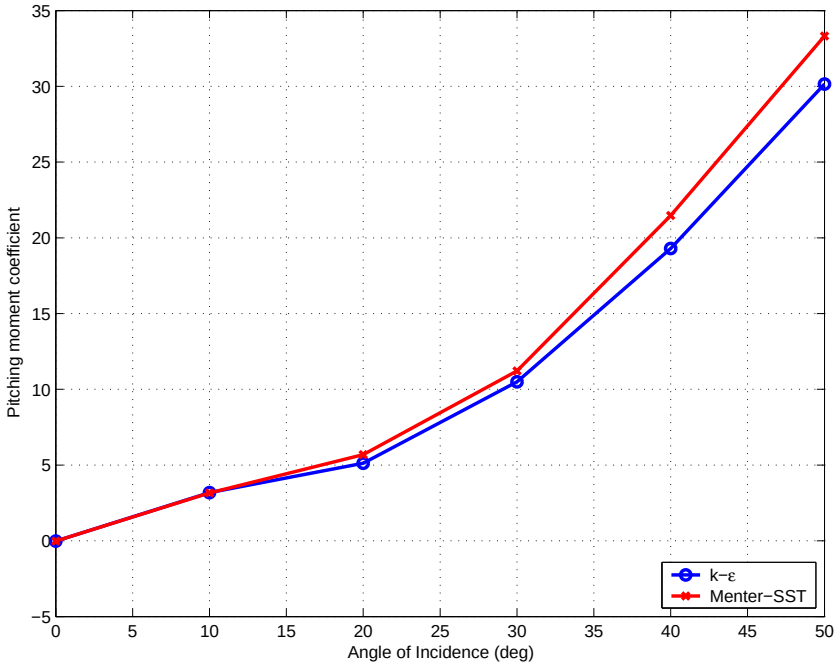
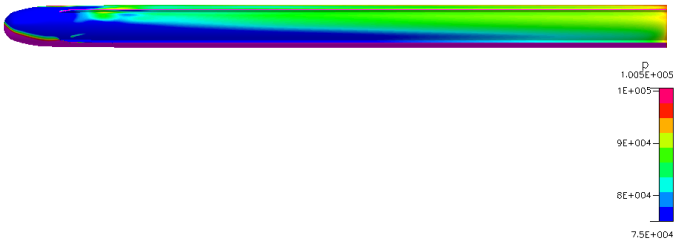


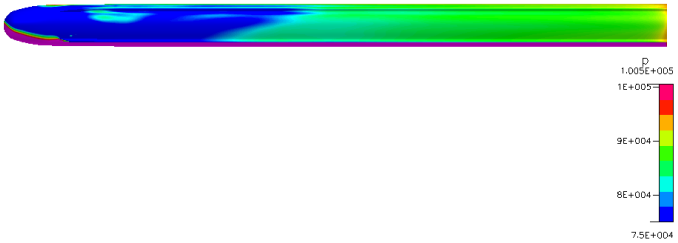
Figure 2.21: Comparison of values of the pitching moment coefficients for the two turbulence models

Figures 2.20 and 2.21 illustrate the differences in the normal force and pitching moment coefficients respectively obtained for the two different turbulence models. At the lower angles of attack, up to and including 10°, the standard $k-\epsilon$ turbulence model and the Menter-SST turbulence model predict very similar values of normal force and pitching moment coefficients. However, at higher angles of attack, the differences in values of the normal force and pitching moment coefficients between the two turbulence models increases. The Menter-SST turbulence model predicts higher values of normal force and pitching moment coefficients than the standard $k-\epsilon$ turbulence model.

The difference in surface pressure distributions, predicted by the two turbulence models is shown in Figure 2.22 for an angle of attack of 40°.



(a) Standard $k-\epsilon$

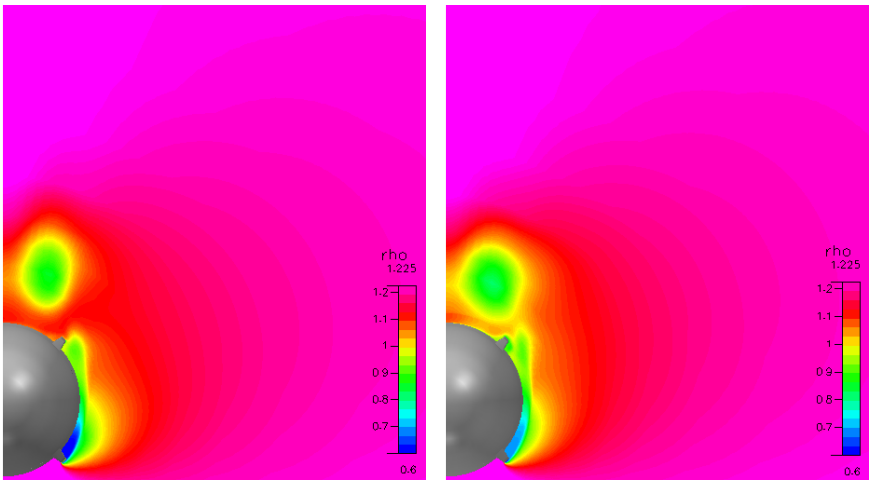


(b) Menter-SST

Figure 2.22: Side view of the surface pressure distributions for the different turbulence models at $\alpha = 40°$

The low surface pressure distribution, indicated by the blue region, on the side of missile body in Figure 2.22b indicates that the flow moves to the leeward side of the body before it separates. In Figure 2.22a, the low pressure regions indicate that flow remains attached on the body for a longer period of time and does not move towards the leeward side of the body.

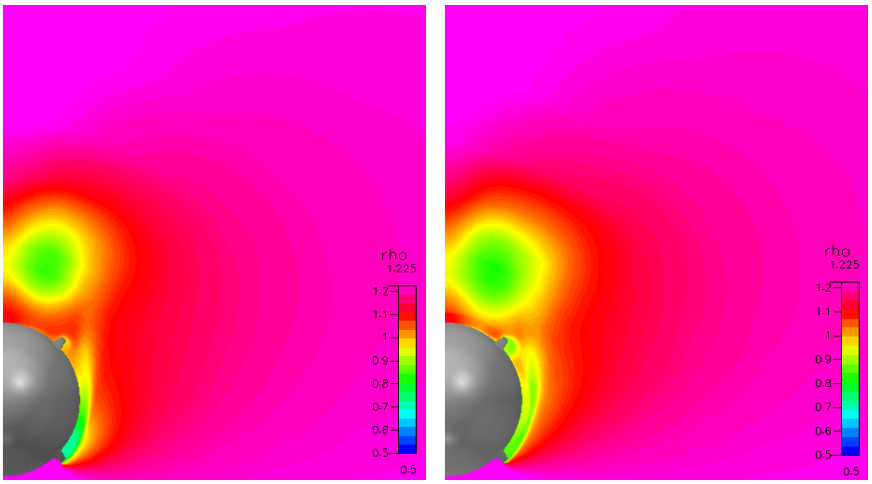
Sectional cuts, at different axial locations are shown in Figures 2.23 to 2.25. These illustrate the difference in the flow formation along the length of the missile body.



(a) Standard $k - \epsilon$ (b) Menter-SST

Figure 2.23: Density contour plot at $x = 3.1D$ at $\alpha = 40°$

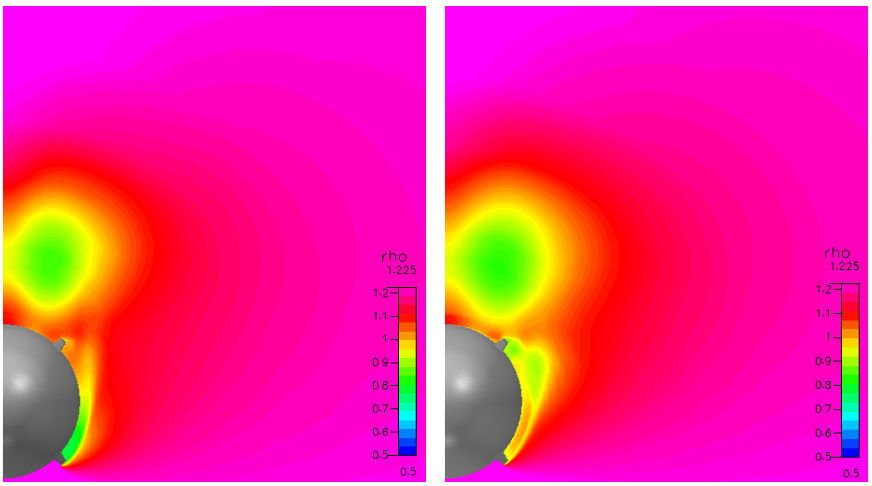
At an axial location of $x = 3.1D$ (Figure 2.23a) the standard $k-\epsilon$ turbulence model predicts that the flow separation vortex that formed as a result of flow interaction with the top strake has separated from the body. The standard $k - \epsilon$ turbulence model predicts that the flow between the two strakes remains attached to the body. From Figure 2.23b it can be seen that the Menter-SST turbulence model predicts that flow between the two strakes is about to separate. The vortex, which formed due to flow interaction with the top strake is still close to the body.



(a) Standard $k - \epsilon$ (b) Menter-SST

Figure 2.24: Density contour plot at $x = 5D$ at $\alpha = 40°$

At an axial location of $x = 5D$, the Menter-SST turbulence model predicts that the flow from the lower body strake separates from the body while the standard $k - \epsilon$ turbulence model does not show this separation (Figure 2.24). A region of recirculating air at the top strake is captured by the Menter-SST turbulence model (Figure 2.24b). The standard $k-\epsilon$ turbulence model fails to predict the recirculating air under the top strake (Figure 2.24a).



(a) Standard $k - \epsilon$ (b) Menter-SST

Figure 2.25: Density contour plot at $x = 6.3D$ at $\alpha = 40°$

At $x = 6.3D$ (Figure 2.25b) the Menter-SST shows that a second vortex separation occurs at the lower strake and that the vortex moves towards the top strake. This second separation is not captured by the standard $k - \epsilon$ turbulence model of Figure 2.25a.

2.4.3 Discussion

In Figures 2.20 and 2.21, the values of the normal force and pitching moment coefficients calculated from the two turbulence models, at the low angles of attack, (between 0° and 10°) are very similar since in this angle of attack range the flow is still attached to the body. However, at the higher angles of attack, the flow begins to separate from the body and areas of recirculating air develop as in Figure 2.24. Therefore at the larger angles of attack, the values calculated for the normal force and pitching moment coefficients are significantly different, with the standard k-ϵ model predicting lower values for the normal force and pitching moment coefficients.

Simulations were run at 40° angle of attack on the geometry at experimental conditions. The normal force coefficients obtained from the CFD simulations for the standard $k-\epsilon$ and Menter-SST $k-\omega$ turbulence models are compared to the experimental normal force coefficient in Figure 2.26. The results obtained from the Spalart-Allmaras turbulence model is also shown in Figure 2.26.

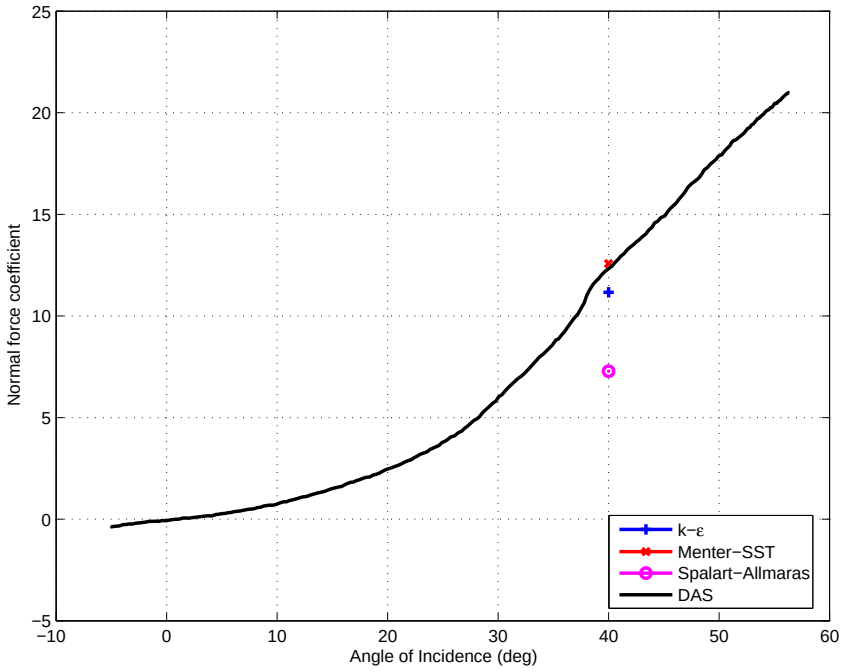


Figure 2.26: Comparison of normal force coefficients

From Figure 2.26 it can be seen that the Menter-SST turbulence model predicts the closest value for the normal force coefficient to the experiment. The standard $k-\epsilon$ turbulence model under-predicts the value for the normal force coefficient. The Spalart-Allmaras turbulence model predicts a normal force coefficient much lower than the experimental normal force coefficient, indicating that the Spalart-Allmaras turbulence model would not be suitable for further use in this study.

Bardina et al. (1997) found that the standard $k - \epsilon$ model under-predicted flow separation. This is indicated by the lower values for C_N. Figure 2.22 shows that the Menter-SST turbulence model predicts separation earlier than the standard k-ϵ turbulence model. This is in keeping with the findings of Bardina et al. (1997) that the standard $k - \epsilon$ turbulence model delays flow separation.

In Figure 2.27 ribbon traces were plotted on the missile body. This figure shows that the Menter-SST turbulence model predicts that the vortex core moves away from the body while the standard $k - \epsilon$ turbulence model shows that the vortex core remains relatively close to the body. When Figure 2.27 is compared to Figure 2.28, which shows flow development on the body of the missile in the wind tunnel, the Menter-SST turbulence model shows a better prediction of the flow around the missile body.



(a) Standard $k - \epsilon$ (b) Menter-SST

Figure 2.27: Ribbon traces off the surface of the missile body at $\alpha = 40°$

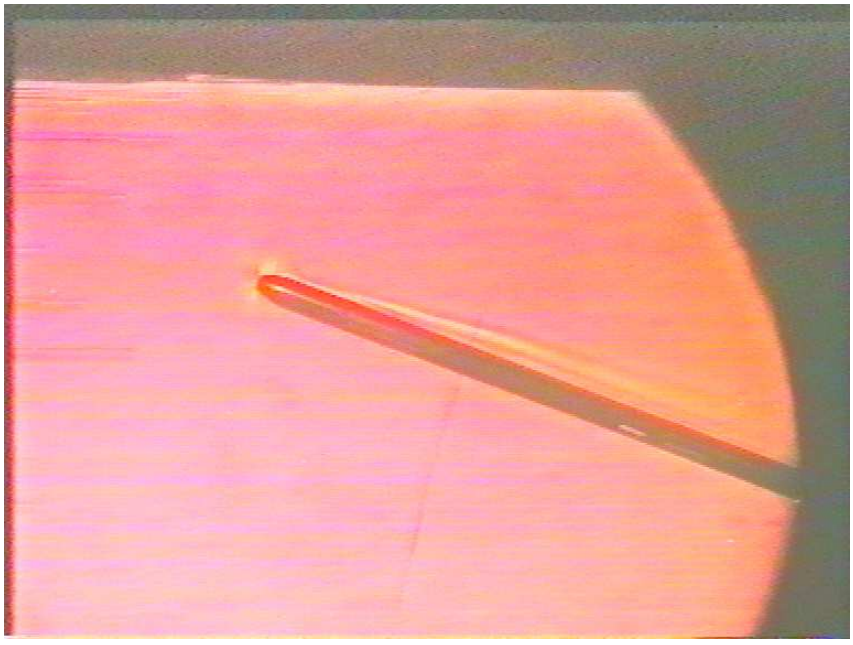


Figure 2.28: Flow development on the missile body in the high-speed wind tunnel (CSIR-Defencetek, 2004)

2.5 Conclusions

From the validation study a number of decisions were made regarding the simulation methods applied in the balance of this study. These are summarised as:

- If a grid with fewer cells than the one used in this study is used, important flow characteristics are not captured properly. There is also a significant difference in surface pressure distributions. Using a grid with more cells has resulted in a very small increase in accuracy. The grid used for model C is adequate as the finer grid of model B does not justify the added computational expense.
- Placing the outlet boundary a distance 5 body lengths from the base of the missile, results in a similar flowfield as when the outlet boundary is placed 20 body lengths away from the base of the body. Thus placing the outflow boundary 5 body lengths from the base of the missile and at atmospheric conditions is acceptable since the flow does not have a significant effect the upstream boundaries.
- As long as the geometry of the missile body and the flowfield are symmetrical and a steady solution is sought, it is sufficient to model half of the geometry in order to obtain values for the normal force and pitching moment coefficients and to gain an understanding of the flowfield.
- Since the Menter-SST $k-\omega$ turbulence model predicted flow separation at high angles of attack better than the standard $k-\epsilon$ turbulence model, the Menter-SST $k-\omega$ turbulence model will be used in further investigations.

3 Effect of Changing the Span of Missile Strakes

A body and strake configuration like that shown in Figure 3.1 was tested in past wind tunnel test series (DAS, 2004). The length of the missile body was $18D$ and the aspect ratio of the strakes was 3.7×10^{-3}.



Figure 3.1: Missile body-strake configuration

The values for normal force coefficient and pitching moment coefficient, shown in Figures 3.2 and 3.3, were determined from Equations 3.1 and 3.2 (Gobey, 2004).

$$C_{NStrake} = C_{NBody-Strake} - C_{NBody} \tag{3.1}$$

$$C_{mStrake} = C_{mBody-Strake} - C_{mBody} \tag{3.2}$$

where:

- $C_{NStrake}$ is the increment in normal force coefficient due to the strakes on a body-strake configuration. It includes the interference factors of the body on the strakes and the strakes on the body.
- $C_{NBody-Strake}$ is the experimental normal force coefficient acting on the body with the strakes.
- C_{NBody} is the experimental normal force coefficient acting on the body of revolution.
- $C_{mStrake}$ is the increment in pitching moment coefficient due to the strakes on a body-strake configuration. It includes the interference factors of the body on the strakes and the strakes on the body.
- $C_{mBody-Strake}$ is the experimental pitching moment coefficient acting on the body with the strakes.
- C_{mBody} is the experimental pitching moment coefficient acting on the body of revolution.

The increment due to the the strakes on a body-strake configuration is often referred to as the effect of the strakes in the presence of the body. The normal force coefficient and pitching moment coefficient for the strakes in the presence of the body are shown in Figures 3.2 and 3.3.

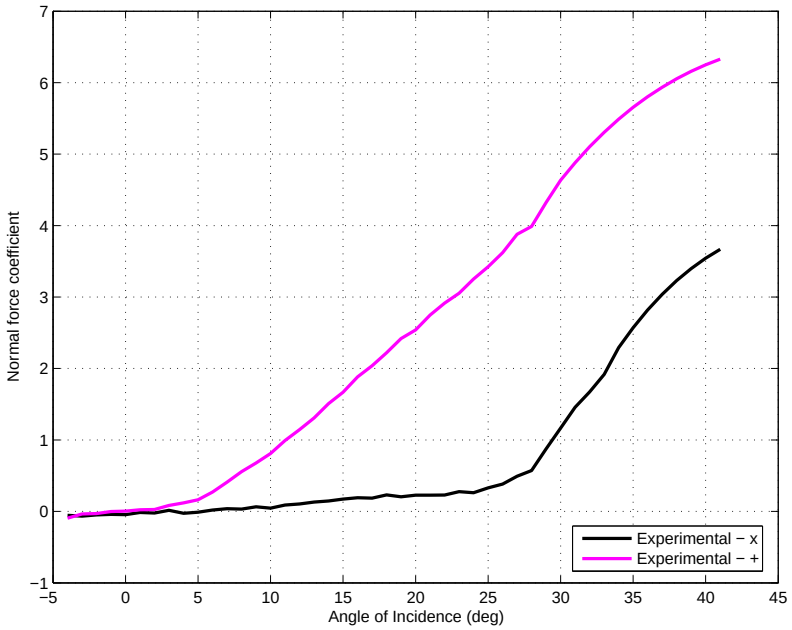


Figure 3.2: Normal force coefficient of strakes in the presence of the body (Mach 0.8) (DAS, 2004)

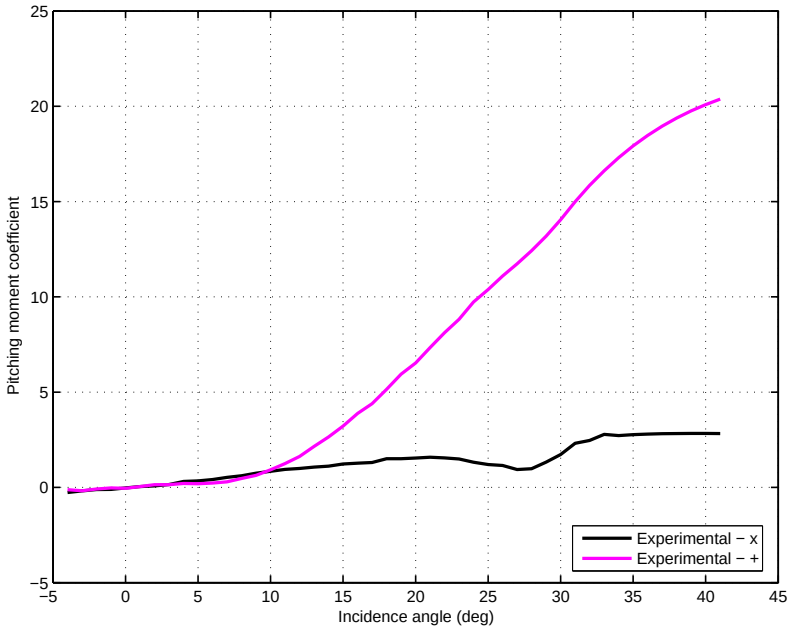


Figure 3.3: Pitching moment coefficient of strakes in the presence of the body (Mach 0.8) (DAS, 2004)

The experimental data in Figures 3.2 and 3.3 were analysed by Gobey (2004). When the strakes are in the '+' roll orientation the strakes have an influence on the normal force coefficient from an angle of attack of 3° upwards. The pitching moment coefficient for the strakes in the '+' roll orientation in Figure 3.3, shows an initial slope and then a sudden increase in slope at a large angle of attack that corresponds to the increase in the normal force coefficient slope. This indicates that the centre of pressure on the strakes shifts forward between angles of attack of 5° and 10° and then remains constant at the large angles of attack (Gobey, 2004).

When the strakes are in the '×' roll orientation the normal force coefficient remains at almost zero magnitude up to 25° angle of attack. This indicates that the strakes are not forcing the flow to separate from the body when they are in the '×' orientation (Gobey, 2004). The pitching moment coefficient of the strake in the presence of the body has a very low slope over the entire angle of attack range in Figure 3.3. There is a dramatic difference in the aerodynamic behaviour of the strakes in the two roll orientations. Gobey (2004) stated that this difference must be eliminated, if possible, to make the aerodynamics of the configuration more consistent with roll angle.

Since the existing configuration could not be drastically changed due to design specifications, it was proposed that the current strake span of $0.06D$ be increased to $0.13D$. The new value for the strake span was based on the fact that by increasing the span of the strakes greater flow separation is forced around the body, increasing the normal force produced by the strakes. However due to design constraints, the strake span could not be increased by a large amount. The value chosen for the new span was not the optimal solution but it was a workable one. A CFD study was carried out to determine if increasing the strake span would result in a sufficient increase in normal force coefficient generated by the strakes when in the '×' orientation, thus allowing for more consistent aerodynamic behaviour with roll angle.

3.1 Grid Generation

Since symmetric flowfields were being investigated, only one half of the geometry, such as that shown in Figure 3.1, was modelled.

A structured grid, such as that shown in Figure 2.15, was used. The grid for the short strake model comprised of 146 circumferential grid points, 55 radial grid points and 150 axial grid points. For the long strake model the number of radial grid points was increased to 65.

The study was carried out at the flight conditions specified in Section 1.1, at angles of attack from 0° to 50° in increments of 10°.

The RANS equations were used to solve the steady flow simulation. The Menter-SST turbulence model was implemented. Roe's FDS was used together with the Osher-C flux limiter to solve the RANS equations.

3.2 Strake Height Influence on Coefficient Behaviour

The normal force and pitching moment coefficients for the two different strake span configurations were calculated by equations 2.6 and 2.7. The percentage increase on the normal force and pitching moment coefficients carried by the strakes due to the increased strake span was calculated from Equations 3.3 and 3.4.

$$\%\Delta C_N = \frac{C_{NHigh} - C_{NShort}}{C_{NHigh}} \times 100 \tag{3.3}$$

$$\%\Delta C_N = \frac{C_{mHigh} - C_{mShort}}{C_{mHigh}} \times 100 \tag{3.4}$$

where:

- C_{NHigh} is the normal force coefficient for the strake with span of $0.13D$,
- C_{NShort} is the normal force coefficient for the strake with span of $0.06D$,
- C_{mHigh} is the pitching moment coefficient for the strake with span of $0.13D$, and
- C_{mShort} is the pitching moment coefficient for the strake with span of $0.06D$.

These values are shown in Table 3.1.

Table 3.1: Percentage increase in normal force coefficient and pitching moment coefficient for the different missile strake spans

α (°)	$\%\Delta C_N$	$\%\Delta C_m$
0	0.000	0.000
10	41.66	46.19
20	16.08	52.59
30	11.28	43.34
40	16.18	35.44
50	19.16	37.45

Table 3.1 shows that by increasing the strake span, there is a significant increase in the normal force and pitching moment coefficients, in particular at angles of attack between 10° and 30°. This implies that with the larger span, the aerodynamic loads carried by the strakes have increased.

The normal force and pitching moment coefficients of the strakes in the presence of the body are shown in Figures 3.4 and 3.5 along with the experimental data. The experimental data is present to confirm the trend of the CFD results and not to serve as an exact match.

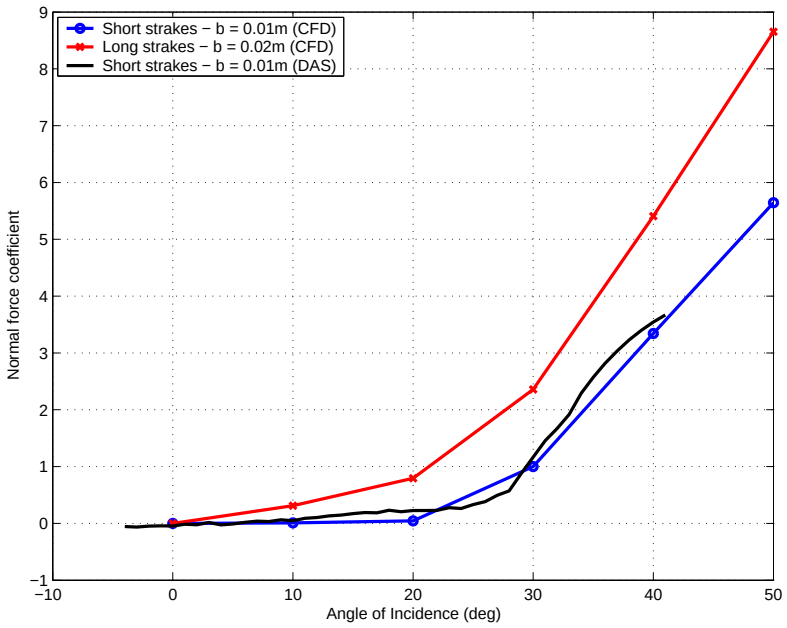


Figure 3.4: Comparison of normal force coefficient between the different span configurations

In Figure 3.4 the trend of the CFD data for the short strakes resembles that of the experimental data for the short strakes. Between angles of attack of 20° and 30° the

slope of the experimental data changes.

The normal force coefficient on the large strakes has increased significantly at the lower angles of attack, up to 25°. For the large strakes there is an increase in the slope of normal force coefficient at low angles of attack compared to the short strakes where the slope of normal force coefficient was almost zero and the normal force coefficient remained at almost zero magnitude up to 20°. The large strakes resulted in an increase in normal force coefficient at the low angles of attack, ranging from 11.28% at 30° angle of attack to 41.66% at 10° angle of attack.

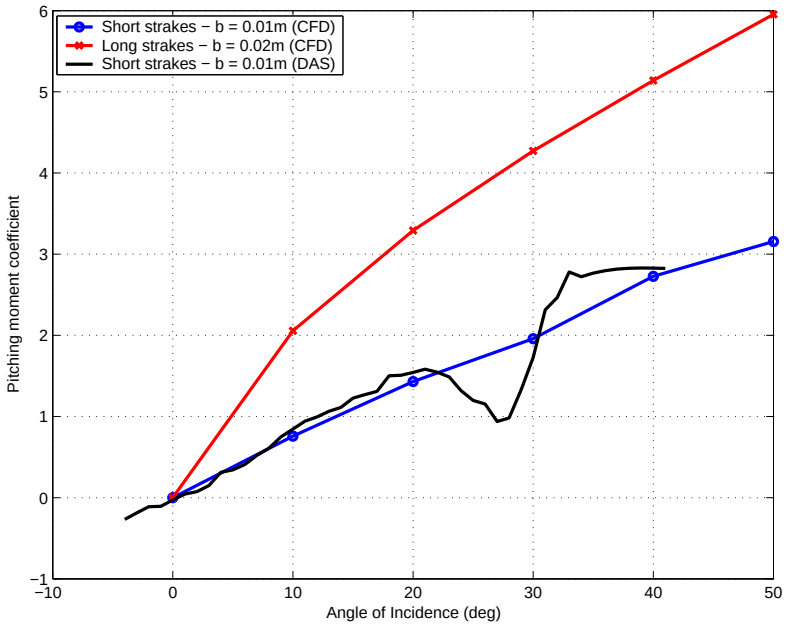


Figure 3.5: Comparison of pitching moment coefficient between the different span configurations

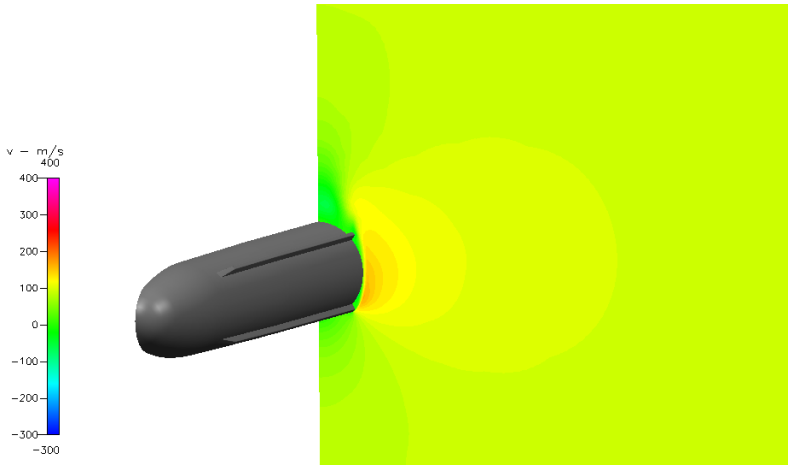
The pitching moment coefficient has also increased significantly at the lower angles of attack, due to the increase in the normal force coefficient. The large strakes have resulted in a percentage increase ranging from 43.34% at 30° angle of attack to 52.59% at 20° angle of attack. For the short strakes pitching moment coefficient varied from 0 to approximately 3. However, in the same angle of attack range, the large strakes' pitching moment coefficient varies from 0 to 6. This indicates that the larger strakes have improved the aerodynamics of the missile. The slope of the pitching moment of the strake has increased significantly with the increase in the strake span. At angles of attack between 20° and 30° the CFD results do not display the same trend as the experimental data. This is due to the formation of steady asymmetric vortices on the experimental model.

The results obtained from the CFD simulations for normal force coefficient compare

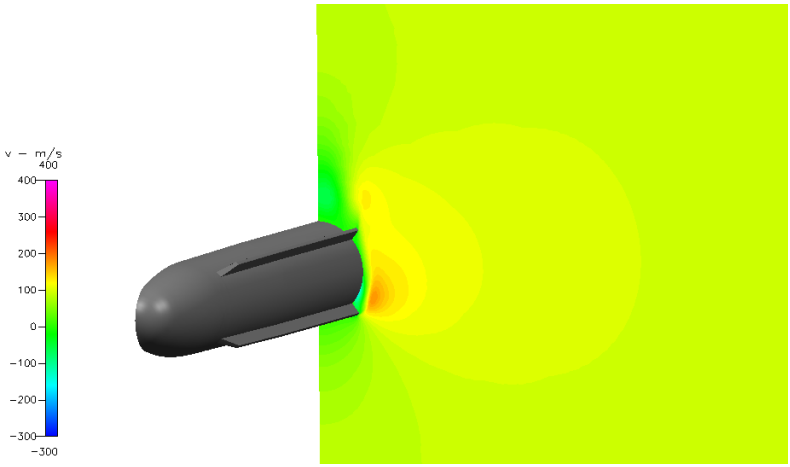
well with the experimental data. The trend for both sets of results are very similar. This is an indication that the CFD results obtained for the increment in normal force coefficient due to the strakes with a span of $0.13D$ would be reasonably accurate.

3.3 Strake Height Effects on the Flowfield

Figures 3.4 and 3.5, show that there is a large increase in the normal force coefficient and pitching moment coefficient on the larger strakes. This is attributed to the larger strakes causing the flow around the body to separate. This is confirmed by Figure 3.6.



(a) Short strakes



(b) Long strakes

Figure 3.6: A side view of the cross flow velocity at $x = 4.7D$ at 20°

Figure 3.6 show that the strakes with $0.06D$ span are not large enough to cause the flow around the body to separate. The flow separates on contact with the lower strake but immediately reattaches itself to the body. When the flow does separate, it does not make contact with the top strake. By increasing the strake span to $0.13D$, reattachment of flow to the body is prevented and stronger vortices are produced.

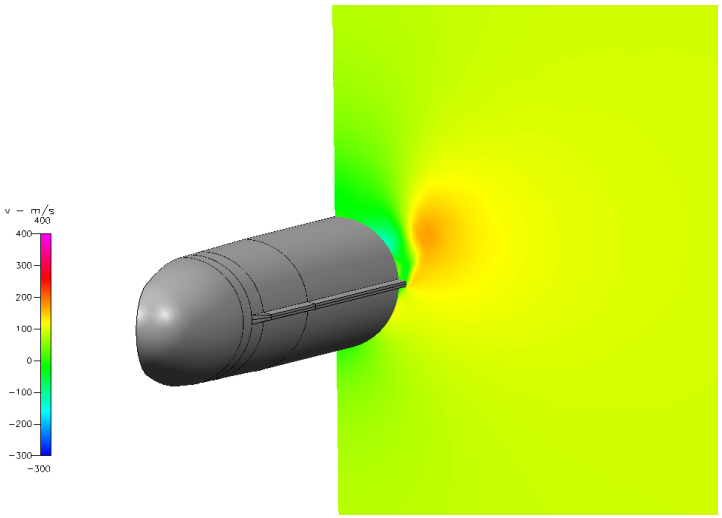


Figure 3.7: A side view of the cross velocity at $x = 4.7D$ at 20° for the strakes orientated in the '+' roll orientation

Figure 3.2 shows that when the short strakes are orientated in the '+', the normal force generated by the strakes is almost twice the normal force generated by the short strakes in the '×' roll orientation at 20° angle of attack. Figure 3.7 shows that the horizontal strakes force flow separation around the body and the separated flow does not reattach onto the body as seen in Figure 3.6a. Since the short strakes, in the '+' roll orientation prevent flow reattachment, the normal force on the strakes in the presence of the body is much larger.

The larger strakes increase the effective diameter of the body, thus causing flow to separate from the body and to remain separated. This resulted in an increase in normal force coefficient at the lower angles of attack, ranging from 11.28% at 30° angle of attack to 41.66% at 10° angle of attack. There was a corresponding increase in the pitching moment coefficient, ranging from 43.34% at 30° angle of attack to 52.59% at 20° angle of attack. This indicates that the overall aerodynamics of the body with the strakes, orientated in '×', has improved. Figure 3.4 shows that between angles of attack of 20° and 30° the normal force coefficient slope changes. This is due to flow not reattaching to the body, thus increasing the normal force coefficient at angles of attack greater than 30°.

Increasing the span of the strakes even further could increase the pitch-up performance of the missile but the size of the strakes are constrained by the aircraft carriage size and the required overall missile mass.

The difference in the CFD data and experimental data for pitching moment coefficient is due to the formation of steady asymmetric vortices on the experimental model. This was expected as CFD does not readily predict the formation of steady asymmetric vortices and considerable effort is required to simulate a steady asymmetric flowfield.

3.4 Conclusion

By increasing the strake span from $0.06D$ to $0.13D$, there was an overall increase in the normal force coefficient ranging from 11.28% at 30° angle of attack to 41.66% at 10° angle of attack. The increase in the normal force coefficient resulted in a corresponding increase in the pitching moment coefficient, ranging from 43.34% at 30° angle of attack to 52.59% at 20° angle of attack. The increase in normal force coefficients, and thus pitching moment coefficients, is due to the large span strakes forcing the flow to separate sufficiently far from the body, thus preventing reattachment of the separated flow to the body. From this it can be concluded that an increase in the strake span results in greater flow separation around the body.

Increasing the strake span to $0.13D$ has prevented the flow around the body from reattaching to the body, thus improving the aerodynamics of the body-strake configuration, for the strakes in the '×' orientation. The aerodynamics of the strakes in the '×' orientation has now been made more consistent with roll orientation since flow reattachment, observed previously only when the strakes were orientated in the '+' orientation, is now observed when the strakes are in '×' orientation as well.

4 Creation of Steady Asymmetric Vortices in CFD

As discussed in Section 1.1 and shown in Figure 1.2 steady vortex asymmetry occurs on a missile body at high angles of attack ($\alpha_{AV} \leq \alpha \leq \alpha_{UV}$), due to geometric imperfections on the missile nose. It is due to this steady asymmetric vortex formation that large side forces develop on the missile body, even at zero sideslip. This results in an uncontrollable missile (Section 1.3). The geometric imperfections provide the initial disturbance which is amplified along the missile body by a spatial instability (Bernhardt and Williams, 1998).

Flow asymmetry is amplified along the length of the body by one of the following two types of instabilities: (Cummings et al., 2003)

Absolute Hydrodynamic Instability The small flow perturbation yields a bifurcated asymmetry, even after the perturbation has been removed, for example unsteady von Kármán vortices. This is a temporal instability and is not considered in this study.

The absolute hydrodynamic instability hypothesis states that as the angle of attack is increased, a bifurcation state occurs at a critical angle of attack that produces one of two 'mirror images'. At any angle of attack greater than the critical angle of attack, only two values of side force exist.

Convective Instability Small geometric perturbations are required for steady vortex asymmetry to exist and the flowfield is not limited to two bifurcated states. If the geometric perturbations are removed the flow returns to its steady symmetric state.

The convective instability hypothesis states that any level of asymmetry is possible at high angles of attack. The asymmetry is not confined to only two levels. As the angle of attack is increased, an unstable state is reached where an infinite number of paths are possible, until the very high angle of attack

regime is reached (Section 1.1.4). At this point, the side force has reached a fully bifurcated state but intermediate regions do exist.

It is evident from the two different instabilities described above that irrespective of the type of instability, a perturbation is required for the formation of asymmetric vortices. In experiments, these perturbations are very common but in numerical calculations these perturbations need to be introduced into the calculation. In numerical calculations the flowfield is an ideal one and the body surfaces are perfectly smooth. Therefore it is not possible to obtain an asymmetric flowfield in numerical calculations without an external perturbation.

Cummings et al. (2003) provide evidence that certain numerical algorithms that break symmetry preservation, do exist, thus causing the flowfield to become asymmetric. One such algorithm is the diagonalised algorithm which was developed to speed up the vector-flux splitting algorithm. This algorithm was not used as the level of disturbance introduced by the algorithm is uncontrolled.

Degani and Schiff (1991) showed numerically, that when an asymmetric perturbation, fixed in time and space, was introduced near the apex of an ogive cylinder, the steady flowfield became asymmetric. By explicitly adding a geometric perturbation on the missile body the level of disturbance introduced into the simulation is known (Cummings et al., 2003). Degani and Schiff (1991) suggested the use of a geometrical bump on the nose of the body of revolution or a small jet flowing normal to the body of revolution. Levy et al. (1996) have shown that, qualitatively, the essential steady asymmetric, multi-vortex structure can be captured by the use of a simple, simulated disturbance. The multi-vortex structure of Figure 1.2 is formed by the breakaway of the higher positioned vortices and the generation of new vortices, developing alternately on either side of the body axis (Xueying et al., 1991). The alternating vortex formation is time-independent but changes along the length of the body (ESDU, 1989). When the perturbation is removed the flow returns to it's symmetric state, demonstrating that the asymmetry was amplified by a convective instability (Degani, 1992).

In order to investigate the effect of the strakelets on steady asymmetric vortices in CFD, a steady asymmetric flowfield had to be simulated first. Once the steady asymmetric flowfield had been simulated on a missile body of revolution (referred to as the missile body), then the strakelets were added to the missile body to investigate the effects of the strakelets on the steady asymmetric vortices.

The size of the geometric perturbation required to trigger the formation of steady asymmetric vortices on the missile body was unknown. Thus an iterative process was carried out to determine:

- the size of geometric perturbation required to trigger the formation of steady asymmetric vortices,
- the effect of the axial location of the geometric perturbation on the formation of steady asymmetric vortices, and
- the effect of the circumferential location of the geometric perturbation on the formation of steady asymmetric vortices.

A way of confirming that an appropriately sized geometric perturbation was chosen, was to to simulate the flowfield around the missile body with the geometric perturbation and at a very low angle of attack. As mentioned in Section 1.1, at low angles of attack the flow on the body remains attached. Therefore the geometric perturbation must not force the attached flowfield to separate from the missile body as this would not be representative of the naturally occurring flowfield on a body of revolution at low angles of attack.

From experimental data shown in Figure 4.1 it was observed that the missile body experienced non-zero side forces at moderate angles of attack due to the formation of steady asymmetric vortices. This is in keeping with the evidence provided by Ericsson and Reding (1991) that for blunt ogive noses, the onset angle of attack for steady asymmetric vortices is lower than that for pointed ogive noses. The onset angle of attack is approximately determined by $4.2\frac{d}{l}$ (Ericsson and Reding, 1991). By that criterion, the onset of steady asymmetric vorticity should occur between 10° and 12° angle of attack. Figure 4.1 shows that steady asymmetric vortices begin at approximately 11° angle of attack. The geometric perturbation must thus be able to simulate steady asymmetric vortices at these low angles of attack as well.

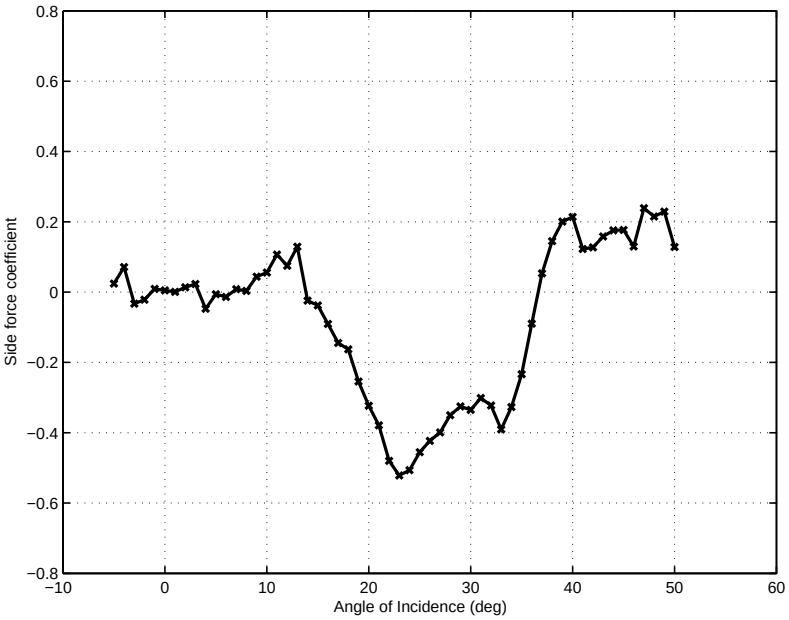


Figure 4.1: Experimental side force coefficient on a body of revolution at Mach 0.8 (DAS (2004))

Figure 4.2 is a schilieren image which shows flow development on the body of revolution in the wind tunnel.

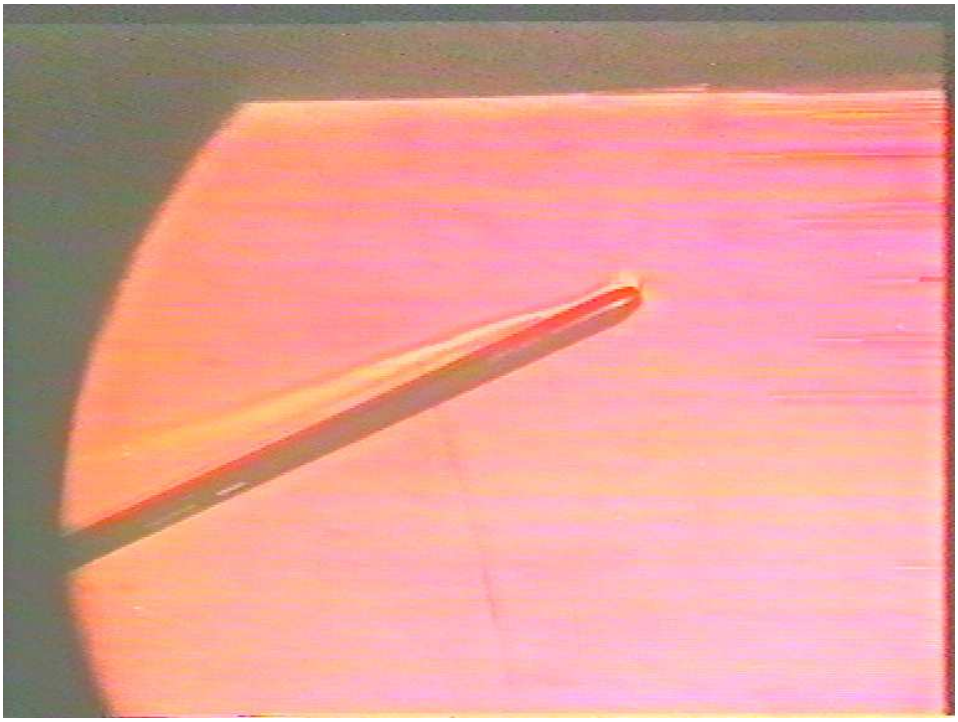


Figure 4.2: Formation of steady asymmetric vortices in the high-speed wind tunnel at Mach 0.8 at an angle of attack of 30° ((CSIR-Defencetek, 2004))

From the schilieren image in Figure 4.2 it can be seen that the flow on the nose of the missile body is attached. Flow separation occurs on the aft cylindrical part of the missile body. The vortices have separated at different axial positions on the missile body. The difference in height between the steady asymmetric vortices is small. Therefore the difference in height between the CFD modelled steady asymmetric vortices must also be small.

4.1 Size of Geometric Perturbation Required to Simulate Asymmetric Vortices

Degani and Schiff (1991) suggested the use of a geometric bump to simulate steady asymmetric vortices in CFD. However, Xuei et al. (2000) showed experimentally that irrespective of the shape of the geometric perturbation, steady asymmetric vortices developed. The bistable state of the steady asymmetric vortices was unaffected and the flowfield structure remained regular even if different shaped perturbations were used (Xuei et al., 2000). Thus instead of using a geometric bump, a hexahedral block was placed $0.25D$ away from the nose tip for this study.

Degani (1992) used a geometric perturbation with a height of 0.01D and a length of 0.05D to create a steady asymmetric flowfield on a pointed slender body. However the body used in this research is a blunt ogive body and thus the exact dimensions used by Degani (1992) could not be used. These dimensions were used as guidelines in choosing the sizes of the geometric perturbations that were to be investigated. Three different sizes of geometric perturbations were studied. The geometric perturbations had the following dimensions:

Table 4.1: Dimensions of geometric perturbations

Model	**Height**	**Length**	**Width**
Perturbation G	$0.06D$	$0.13D$	$0.02D$
Perturbation H	$0.03D$	$0.13D$	$0.02D$
Perturbation I	$0.03D$	$0.06D$	$0.02D$

The width of the geometric perturbations were chosen to be very small and was not varied in this investigation as Degani (1992) indicated that the height and length of the geometric perturbation were the critical factors in modelling steady asymmetric vortices on a body of revolution.

4.1.1 Grid generation

Since the area of interest was the missile forebody and the fact that steady asymmetric vortices alternate along the length of the body, only $8.1D$ of the missile body of revolution was modelled. In this way the number of grid cells required to create a mesh was reduced, thus reducing the number of iterations required for a solution to be obtained.

The geometry modelled is shown in Figure 4.3. This figure shows the size of the geometric perturbation relative to the missile body.



Figure 4.3: Body and geometric perturbation geometry

.

Each structured grid consisted of 272 equispaced circumferential grid points extending completely around the body. In each circumferential plane, the grid consisted of 45 radial points between the body surface and the computational outer boundary and 95 axial points between the nose tip and the base of the body. This grid was very similar to the one constructed by Degani (1992).

The simulations were carried out at the conditions specified in Section 2.1 Simulations were only run at three angles of attack, namely, 5°, 20° and 40° at Mach 0.8 and a Reynold's number of 3×10^6. The results from the 5° angle of attack simulation would indicate whether the geometric perturbation has changed the flowfield on the missile body at low angles of attack. The geometric perturbation also had to introduce a small degree of asymmetry into the flowfield at angles of attack of 20° and 40° as steady vortex asymmetry is low on blunt ogive bodies. A low degree of asymmetry is characterised by a small difference in surface pressures across the body's centre-line and a small difference in height between the two steady asymmetric vortices (Degani and Levy, 1992).

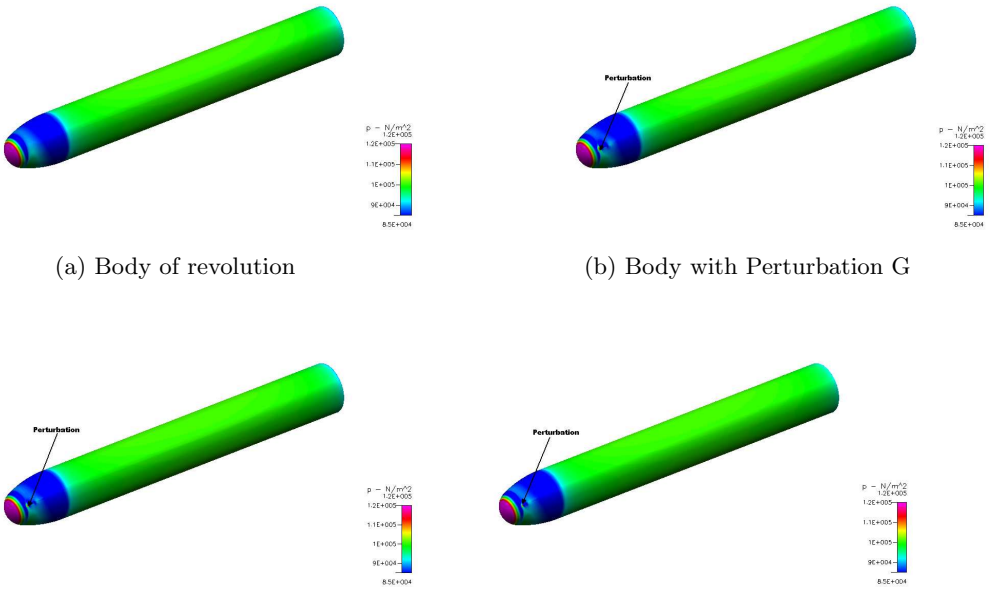
The Menter-SST k-ω turbulence model was used. The flux-splitting algorithm used was Roe's FDS algorithm with the Osher-C flux limiter. Simulations were run at steady conditions, independent of time-step size since asymmetric vortex formation is time-independent. Hartwich et al. (1990) showed that asymmetric vortical flowfields are steady-state solutions to the Navier-Stokes equations.

Simulations were also run on a body of revolution at the three different angles of attack. This was to serve as a comparison between the flowfields created with and without the geometric perturbation.

The full length missile body was also modelled, to see if the multi-vortex structure of Figure 1.2 could be captured by the use of a simulated disturbance, as indicated by Levy et al. (1996).

4.1.2 Results for 5° angle of attack

The surface pressure distributions, shown in Figure 4.4 for the four models, are identical. It is very difficult to determine whether the geometric perturbation had an effect on the flowfield as pressure variations at low angles of attack are very small (Champigny, 1986).



(a) Body of revolution

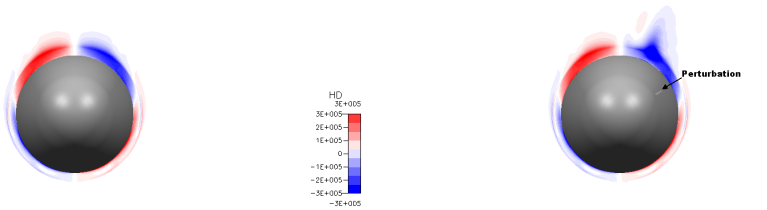
(b) Body with Perturbation G

(c) Body with Perturbation H

(d) Body with Perturbation I

Figure 4.4: Surface pressure distribution on missile body at $\alpha = 5^\circ$ for various geometric perturbations

Contours of helicity density (discussed in Section 2.1) were plotted on cross-sectional cuts, so as to determine if the different geometric perturbations forced vortex separation. Figure 4.5 shows the flow development at an axial distance of $6D$ from the nose tip.



(a) Body of revolution

(b) Body with Perturbation G



(c) Body with Perturbation H

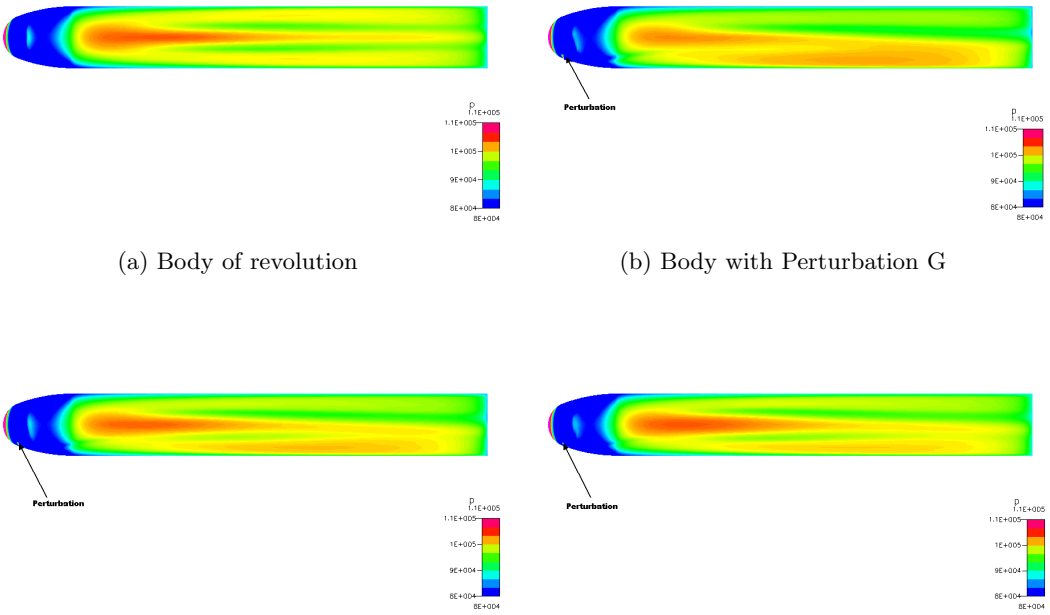
(d) Body with Perturbation I

Figure 4.5: Helicity density contours at $x = 6D$ at $\alpha = 5^\circ$ for various geometric perturbations

Figure 4.5a shows the flow formation on the missile body of revolution without the geometric perturbation on the missile nose. The flow is still attached to the body which is characteristic of flow on bodies of revolution at low angles of attack (Ericsson and Reding, 1991). Figure 4.5b shows that the flowfield due to flow interaction with perturbation G has changed. The right vortex, represented by the blue region, appears to be separating from the body. The two vortices have differing strengths as indicated by the different colour intensities. This indicates that perturbation G is forcing asymmetric vortex separation. The flow formation illustrated in Figures 4.5c and 4.5d is very similar to the flowfield on the body of revolution in Figure 4.5a, indicating that perturbations H and I did not have any significant effect on the attached flow.

4.1.3 Results for 20° angle of attack

The symmetrical surface pressure distribution in Figure 4.6a shows that a pair of symmetrical vortices have formed on the missile body. However, the experimental data in Figure 4.1 show that a non-zero side force exists at 20° angle of attack, indicating that the flowfield should be asymmetric. Figures 4.6b, 4.6c and 4.6d show that by adding a geometric perturbation on the nose of the missile body, the steady symmetric flowfield is forced to a steady asymmetric state. In Figures 4.6b, 4.6c and 4.6d the asymmetric pressure is prominent at the rear of the missile body. The high surface pressure at the rear of the bodies indicates that side forces developed on one side of the body and that the side forces do not oscillate on the body. The non-oscillating side force distribution at 20° is very similar to that found by Champigny (1994).



(a) Body of revolution

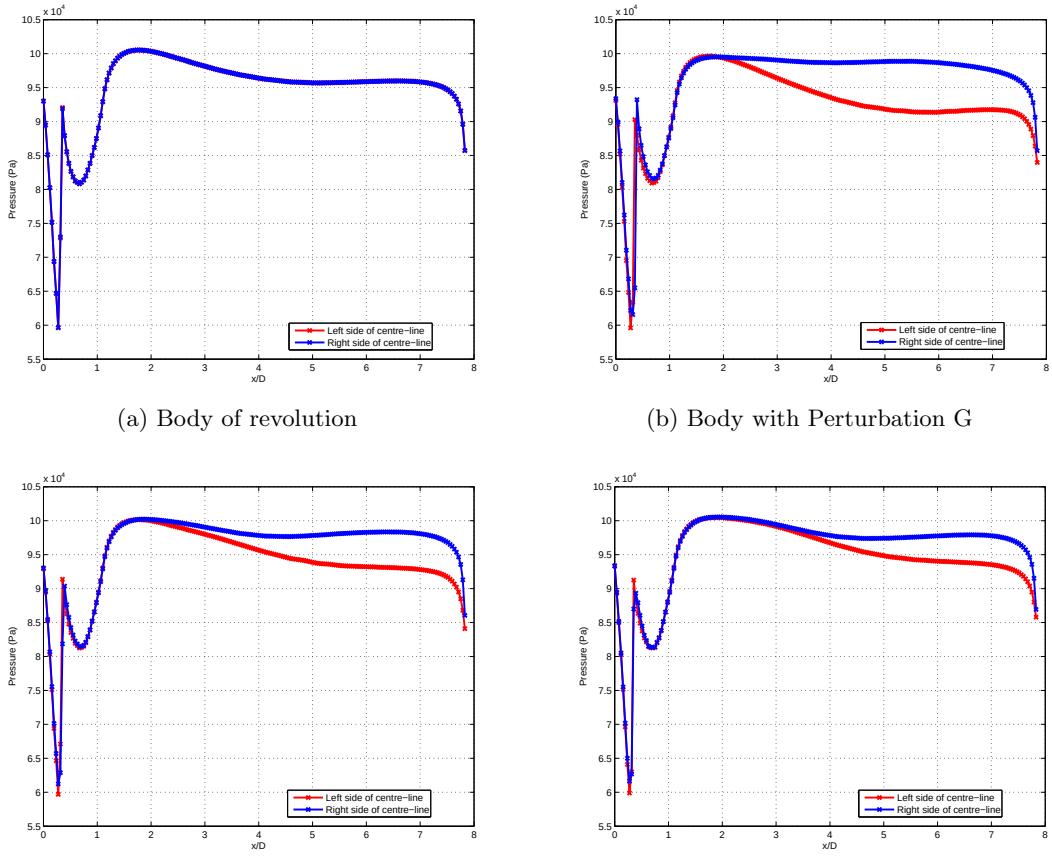
(b) Body with Perturbation G

(c) Body with Perturbation H

(d) Body with Perturbation I

Figure 4.6: Surface pressure distribution on missile body at $\alpha = 20°$ for various geometric perturbations

Perturbation G, in Figure 4.6b has resulted in a large difference in surface pressure distribution between the two halves of the missile body, thus the asymmetry present in the flowfield of Figure 4.6b is high. The differences in the surface pressure distributions between the two halves of the body for perturbations H and I, in Figures 4.6c and 4.6d, are not as large as that which exists for perturbation G, indicating that the asymmetry present in the flowfield, as a result of perturbations H and I, is lower. This is clearly shown in Figure 4.7, which shows the difference in surface pressures across the two halves of the body. The surface pressures a distance of $0.06D$ on either side of body centre-line were plotted.



(a) Body of revolution

(b) Body with Perturbation G

(c) Body with Perturbation H

(d) Body with Perturbation I

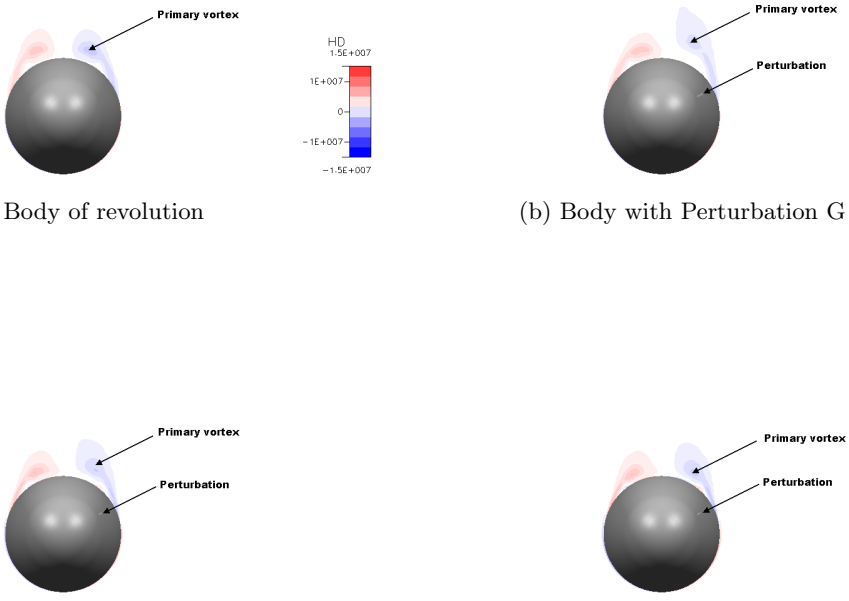
Figure 4.7: Surface pressure distribution along the length of the missile body at 20° angle of attack for various geometric perturbations

As is to be expected the surface pressure distribution across the body of revolution's centre-line in Figure 4.7a are identical. For perturbation G, in Figure 4.7b, there is a large difference in surface pressures across both halves of the body, while the differences in surface pressure for perturbations H and I, in Figures 4.7c and 4.7d are smaller. The asymmetry due to perturbation G occurs closer to the nose of the missile body than the asymmetry forced by perturbations H and I. Perturbation I

shows the smallest difference in surface pressures, indicating that it introduced the lowest degree of asymmetry into the flowfield.

The local minimum in Figure 4.7, located approximately $0.2D$ from the nose tip, is due to flow interaction with the perturbation. The local minima for the two curves in Figures 4.7b, 4.7c and 4.7d are unequal, since the geometric perturbation is located on one side of the missile body.

Figures 4.8 and 4.9 show vortex formation at axial locations of $4D$ and $6D$ respectively by means of helicity density contours.



(a) Body of revolution

(b) Body with Perturbation G

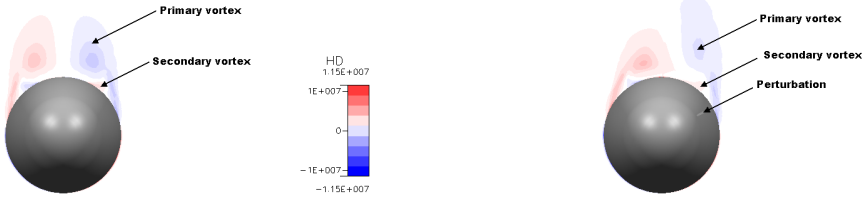
(c) Body with Perturbation H

(d) Body with Perturbation I

Figure 4.8: Helicity density contours at $x = 4D$ at $\alpha = 20°$ for various geometric perturbations

Figure 4.8a shows the development of a symmetrical pair of vortices on the body of revolution, as previously indicated. This prediction by the CFD simulations is not a realistic representation of the flowfield on a body at high angles of attack. The bodies with the perturbations have forced the vortices to separate asymmetrically. In Figures 4.8b, 4.8c and 4.8d, the right vortices, indicated by the blue region, have separated first, since the right vortices are larger than the left vortices, indicating that the right vortices are weaker than the left vortices. This is due to vortex diffusion along the length of the missile body. This was expected since the geometric

perturbations are placed on the right of the body centre-line. This is further confirmed by the higher surface pressure on the right of the body centre-line at the corresponding axial location in Figures 4.7b, 4.7c and 4.7d. The higher surface pressure on the right indicates that the right vortex is further away from the body than the left vortex. The two formed vortices are the primary vortices. The right vortex in Figure 4.8b is further away from the body than the vortices on right vortices in Figures 4.8c and 4.8d, resulting in a higher surface pressure on the body with perturbation G at an axial location of $4D$. This can be clearly seen in Figure 4.7b where the surface pressure on the right of the body centre-line is higher than that in Figures 4.7c and 4.7d at the corresponding axial location on the missile body.



(a) Body of revolution

(b) Body with Perturbation G



(c) Body with Perturbation H

(d) Body with Perturbation I

Figure 4.9: Helicity density contours at $x = 6D$ at $\alpha = 20°$ for various geometric perturbations

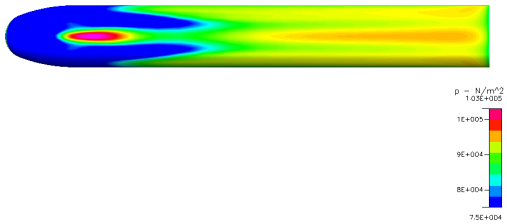
Figure 4.9 shows the development of secondary vortices. The vortex formation in Figures 4.9b, 4.9c and 4.9d corresponds to the flow structure identified by Degani and Levy (1992). The secondary vortices form due to the adverse circumferential pressure gradient encountered by the boundary layer behind the low pressure region created by the primary vortices (Degani and Levy, 1992). The secondary vortices rotate in the opposite direction to their associated primary vortices, as noted by Degani and Levy (1992). This confirms that the grid used and the CFD simulations

are adequately capturing the important features in the steady asymmetric flowfield.

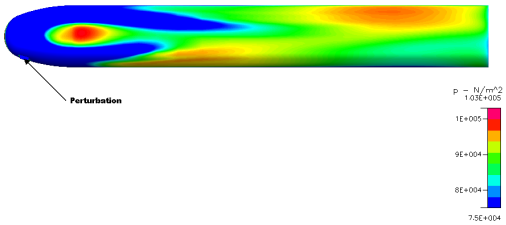
In Figure 4.9 the left primary vortex, represented by the the red region, has separated from the body. The asymmetric primary vortices in Figures 4.9b, 4.9c and 4.9d resemble the asymmetric vortices shown in section A-A of Figure 1.2. Figure 1.2, however, does not show the formation of secondary vortices. The secondary vortices form once the primary vortices have separated from the body. Therefore the secondary vortices also develop asymmetrically along the length of the missile body. This is clearly shown in Figures 4.9b, 4.9c and 4.9d, where the left secondary vortices are smaller than the right secondary vortices due to the asymmetric separation of the primary vortices.

4.1.4 Results for 40° angle of attack

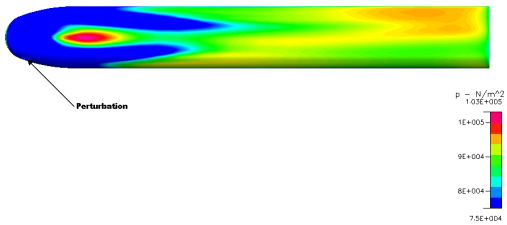
Figure 4.10 shows the surface pressure distribution on the missile bodies with the different geometric perturbations.



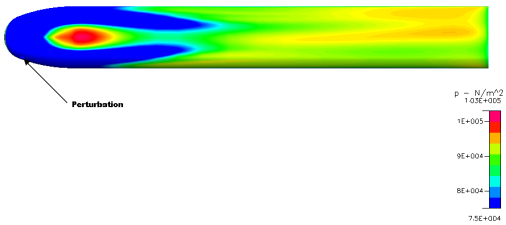
(a) Body of revolution



(b) Body with Perturbation G



(c) Body with Perturbation H

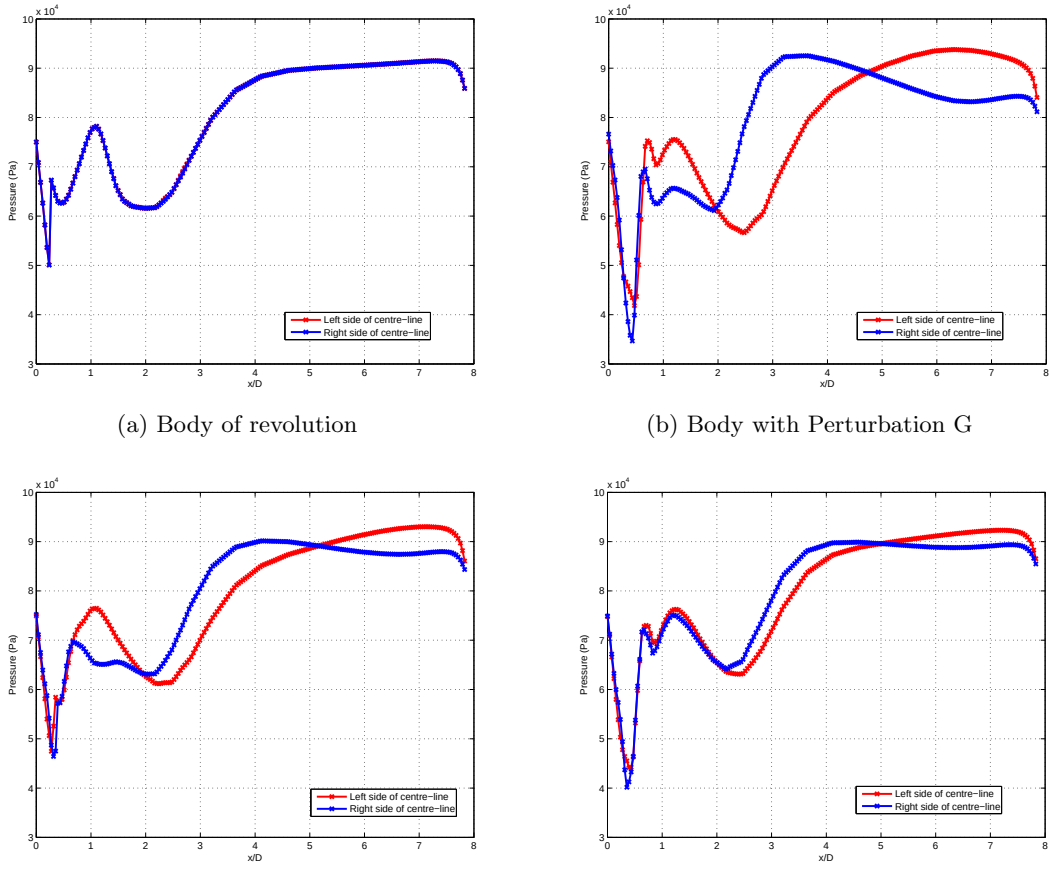


(d) Body with Perturbation I

Figure 4.10: Surface pressure distribution on missile body at $\alpha = 40°$ for various geometric perturbations

Figure 4.10 indicates that the degree of asymmetry present in the flowfield at 40° angle of attack is greater than the degree of asymmetry present in the flowfield at 20° angle of attack (see Figure 4.6). This is expected given the flow geometry discussed in Section 1.1.3. Figures 4.6 and 4.7 also show that it is only at the rear that there is a prominent difference in surface pressure distributions. Figures 4.10 and 4.11 show that the difference in surface pressure distributions alternate on the body, indicating that vortex asymmetry has started earlier on the body at 40° than at 20° angle of attack. Ericsson and Reding (1991) provided evidence that as the angle of attack of the slender body is increased, vortex asymmetry moves closer to the nose tip. The alternating high surface pressures on the body in Figure 4.10 shows the alternate steady asymmetric vortex formation. The alternating high surface pressures at 40° also indicates that the side force distribution alternates along the length of the body as predicted in Figure 1.3.

The surface pressures at a distance of $0.06D$ from the body centre-line are shown in Figure 4.11.



(a) Body of revolution

(b) Body with Perturbation G

(c) Body with Perturbation H

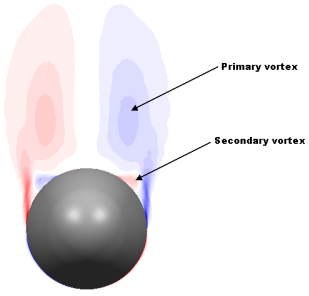
(d) Body with Perturbation I

Figure 4.11: Surface pressure distribution along the length of the missile body at 40° angle of attack for various geometric perturbations

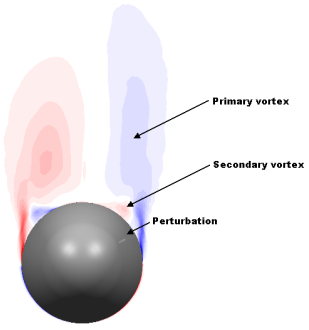
There is a large difference in surface pressure distributions between both halves of the body for perturbation G in Figure 4.11b. This once again illustrates that perturbation G has forced the vortices to separate from the body with larger asymmetry than perturbations H and I. Figure 4.11d shows that perturbation I has introduced the smallest degree of asymmetry into the flowfield indicated by the small difference in surface pressures across the two halves of the body. This indicates that perturbation I has forced an asymmetric flowfield which would be more representative of the actual flowfield on a real blunted ogive body of revolution at high angles of attack.

In Figures 4.11b, 4.11c and 4.11d the surface pressures on the left side of the missile body becomes higher than that on the right side of the body at approximately $x = 5.2D$. These alternating surface pressures across the body centre-line are due to the alternating detachment of vortices from the body (Section 1.1.4).

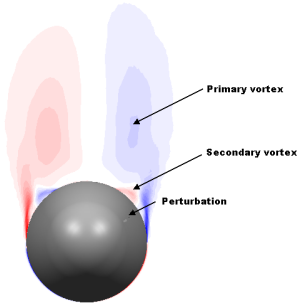
Figures 4.12 and 4.13 are helicity density colourmaps, at different axial locations along the body of revolution, showing vortex formation for the various geometric perturbations.



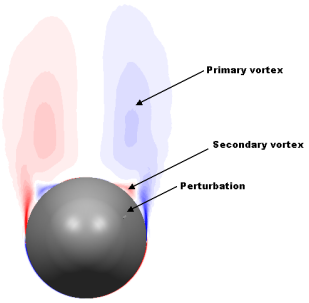
(a) Body of revolution



(b) Body with Perturbation G



(c) Body with Perturbation H



(d) Body with Perturbation I

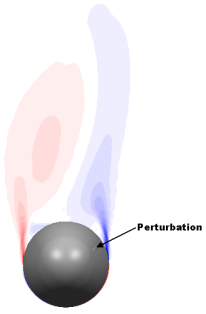
Figure 4.12: Helicity density contours at $x = 4D$ at $\alpha = 40^\circ$ for various geometric perturbations

Figure 4.12a shows the formation of a pair of symmetric primary and secondary vortices that would result in no side force. However, the experimental results in Figure 4.1 shows that at 40° angle of attack a side force does exist on the missile body, indicating the presence of steady asymmetric vortices. Figures 4.12b, 4.12c and 4.12d show the formation of primary and secondary vortices. At the corresponding axial location on the missile body at 20° angle of attack only the right primary vortex had separated from the missile body. This illustrates that at higher angles of attack vortex separation occurs closer to the missile nose.

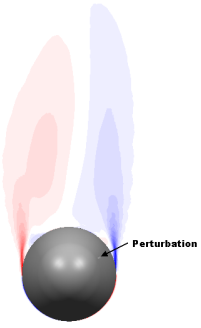
Perturbation G in Figure 4.12b has resulted in a flowfield with a higher degree of asymmetry than the flowfields on the bodies with perturbations H and I due to the large difference in size between the right and left vortices. The difference in the vortex heights away from the body surface is indicated in the large difference in surface pressures at $x = 4D$ in Figure 4.11b. The small difference in surface pressures at $x = 4D$ in Figures 4.11c and 4.11d shows that that the right and left vortices in Figures 4.12c and 4.12d are not as far from the body as the vortices in Figure 4.12b.



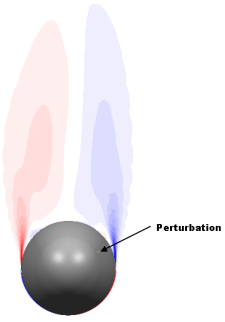
(a) Body of revolution



(b) Body with Perturbation G



(c) Body with Perturbation H



(d) Body with Perturbation I

Figure 4.13: Helicity density contours at $x = 6D$ at $\alpha = 40°$ for various geometric perturbations

Perturbation G in Figure 4.13b introduces the alternating behaviour of steady asymmetric vortices discussed in Section 1.1.3 and shown in Figure 1.2, along the length of the missile body. The missile body with perturbation G shows that a second primary vortex is about to form on the right, below the red vortex. Since perturbations H and I introduced a low degree of asymmetry into the flowfield, this alternating behaviour of steady asymmetric vortices along the body length cannot be observed in Figures 4.13c and 4.13d. However Figures 4.11c and 4.11d shows that at $6D$ away from the missile nose tip, the surface pressure on the left side is larger than that on the right side as opposed to the surface pressures at $4D$ where the surface pressure on the right side is higher than the left side.

4.1.5 Discussion

In Figure 4.5 for the missile body at 5° angle of attack, the right vortex is larger than the left vortex indicating that perturbation G is forcing vortex separation at low angles of attack. A possible reason for flow separation only occurring on the body when perturbation G was used, is that perturbation G has a greater height than perturbation H and has a greater height and length than perturbation I. Even though the separation is small, a side force will develop. Thus perturbation G cannot be used due to its larger height since it would not be representative of the experimental results. The flowfield on the body due to perturbations H and I, in Figures 4.5c and 4.5d resembled the attached flowfield of the missile body of revolution in Figure 4.5a. Since the flowfield on the body with perturbations H and I were very similar to the flowfield in Figure 4.5a, the side forces on the bodies with perturbations H and I would be very close to zero.

The side force coefficients for the bodies with the three perturbations were calculated from Equation 4.1.

$$C_Y = \frac{F_Y}{\frac{1}{2}\rho V^2 S_{ref}} \tag{4.1}$$

The values for ρ, V and S_{ref} are the same as those used in Section 1.3. F_Y, the side force in Newtons, was obtained from the CFD simulations.

The side force coefficients were plotted with the experimental data and with the CFD data for the body of revolution in Figure 4.14.

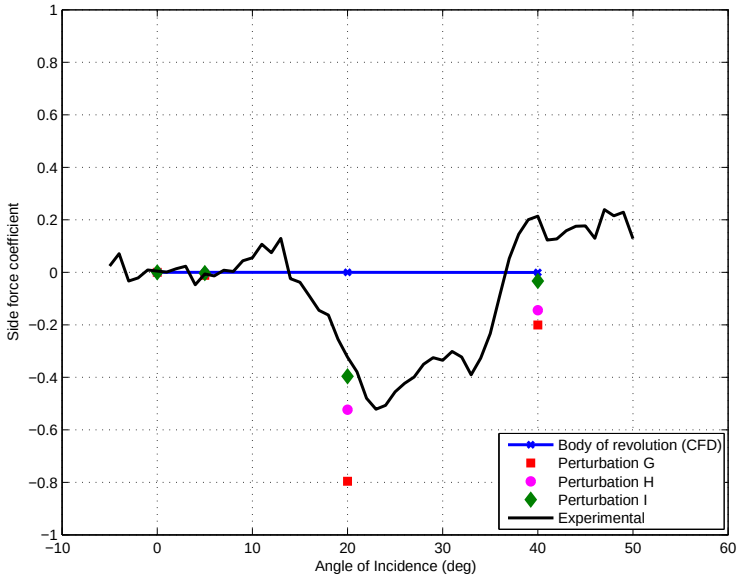


Figure 4.14: Comparison of side force coefficient values for the different perturbations

Quantitatively the CFD data and the experimental data do not match since the experimental conditions and the conditions at which the CFD simulations were carried out were different. The experimental side force coefficients are for the full length missile body while the CFD results are only for a portion of the missile body. The qualitative behaviour of the CFD data, for all three geometric perturbations is very similar to the experimental data, though it does not predict the sign reversal at 40° angle of attack. This can be attributed to the fact that only a portion of the missile body was modelled.

The three perturbations produced almost zero side force coefficients at 5° angle of attack. Perturbation G resulted in the largest side force coefficients at angles of attack of 20° and 40°, which are significantly larger than the experimental data. Perturbation I resulted in side force coefficients which were the closest to the experimental data at 20° and 40°, indicating that it resulted in a steady asymmetric flowfield that is most representative of the experimental flowfield. The side force coefficients due to perturbation H were in between the side force coefficients for perturbations G and I. Perturbation H had a smaller height than perturbation G but a larger length than perturbation I and thus the side force values obtained from the simulations with perturbation H would lie between the side force values for perturbations G and I.

The experimental data shows that at angles of attack of 20° and 40°, non-zero side force coefficients exist and at low angles of attack, side force coefficients are zero. The CFD simulations were not carried out to quantitatively match the experimental data

but to confirm that at 20° and 40° steady side forces due to geometric perturbations can be modelled on a blunt-ogive body of revolution.

Figure 4.6 and 4.7 show that the asymmetric surface pressure distribution begins at the rear cylindrical part of the missile and not at the nose. This is characteristic of blunt ogive bodies, where vortex shedding begins on the aft cylindrical part of the body (Ericsson and Reding, 1991). This is an indication that geometric perturbations on the missile nose simulated a realistic characteristic of steady asymmetric vortex formation on the missile body. When the angle of attack was increased from 20° to 40°, the asymmetry moved forward as shown in Figure 4.7 and 4.11 and described in Section 1.1.3. This flowfield characteristic was observed by Luo et al. (1998), that as the angle of attack increased, the locations of vortex asymmetry and vortex separation propagated upstream toward the nose tip. This characteristic can also be observed in Figures 4.9 and 4.12. At 20° angle of attack, asymmetric primary and secondary vortex formation was identified at an axial location of $6D$ on the body, while at 40° angle of attack, asymmetric primary and secondary vortex formation was identified at an axial location of $4D$.

Also evident from Figures 4.9 and 4.12 is that the secondary vortices form asymmetrically. It is this asymmetric development of primary and secondary vortices that results in the asymmetric surface pressure distributions in Figures 4.6 and 4.10 for the missile bodies with perturbations.

The larger height of perturbation G increased the effective local diameter of the body and thus resulted in a greater degree of flow separation. Degani and Levy (1992) found that for small perturbations, the degree of asymmetry present in the flowfield was small but increasing the size of the perturbation increased the asymmetry in the flowfield. A low degree of asymmetry is characterised by the one vortex being slightly higher than the other and consequently the difference between the surface pressure distribution on opposite sides of the body is small (Degani and Levy, 1992). At 20° and 40° angles of attack, the right primary vortex separates first from the body for perturbations H and I. The difference in height between the left primary vortex, after it has separated and the right primary vortex is very small. This can be clearly seen in Figures 4.9c and 4.13c and Figures 4.9d and 4.13d, which show the flowfields for perturbation H and I respectively. Since perturbation H and I have small heights, flow separation is small. The surface pressures along the length of the body, shown in Figures 4.6c, 4.7c, 4.10c and 4.11c, show a correspondingly small difference between the opposite sides of the body centre-line.

The steady asymmetric flowfield generated by perturbation G is characteristic of a

flowfield with a high degree of asymmetry (Degani and Levy, 1992). Flow separation occurs earlier on the body due to the perturbation's larger height and length. A large difference in the surface pressures exists across the body centre-line (Figures 4.10b and 4.11b).

The three perturbations used in this study were able to force the formation of asymmetric vortices. However, perturbation G forced a high degree of asymmetry into the flowfield due to it's larger height and length, as indicated by the large differences in surface pressures across both halves of the body centre-line in Figure 4.7b and figure 4.11b. Perturbation H introduced a low degree of asymmetry into the flowfield but the difference in surface pressures across the body centre-line is larger in Figures 4.7c and 4.11c due to perturbation H being longer than perturbation I. The side force coefficients obtained from the simulations with perturbation I were very close to that obtained experimentally (Figure 4.14). Therefore perturbation I will be used in the remainder of the study to determine the effect of strakelets on asymmetric flow.

4.1.6 Confirmation of type of instability

In order to confirm the origin and type of the asymmetric flow, perturbation I was removed from the missile body after simulations had converged to a steady asymmetric solution. The simulation was then restarted from this point. This exercise was performed for an angle of attack of 40° only. The change in side force per iteration is shown in Figure 4.15

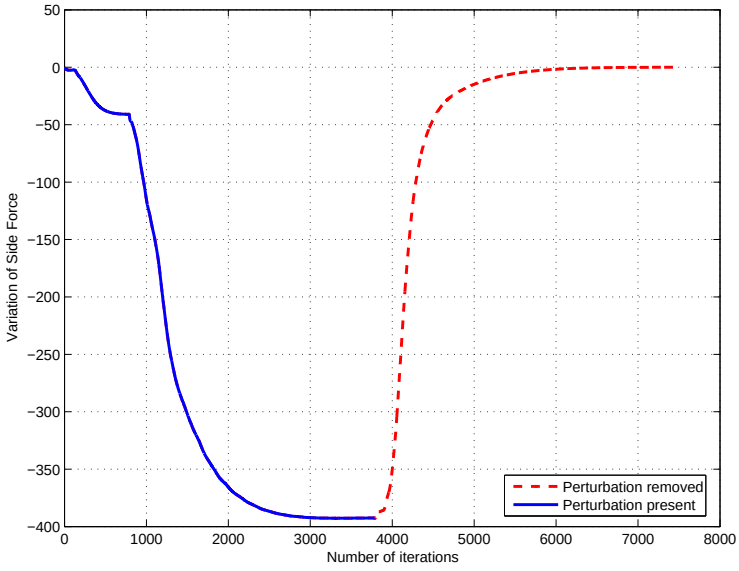


Figure 4.15: Side force variation per iteration

Figure 4.15 shows that once the geometric perturbation had been removed, the flowfield returned to it's ideal symmetric state. Thus the steady asymmetric flow had its origin in a convective instability of the original flow that was induced by a geometric perturbation. A large perturbation resulted in a high degree of flow asymmetry and a small perturbation resulted in a low degree of asymmetry. This is consistent with the idea of convective instability due to geometric perturbations where an increase in the perturbation size results in an increase in the degree of asymmetry (Levy et al., 1996).

4.1.7 Full length missile results

The full length of the missile body, with perturbation I, was also simulated at 40° angle of attack. The asymmetric surface pressure distribution for the full length missile is shown in Figure 4.16.

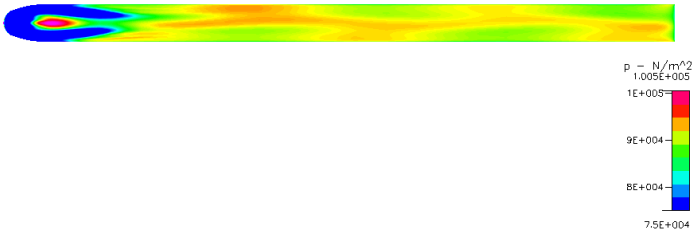


Figure 4.16: Surface pressure distribution on the full length missile body

The asymmetric surface pressure distribution along the full length of the missile body indicates that a simple simulated disturbance can qualitatively capture the asymmetric multi-vortex structure, shown in Figure 1.2. The alternating nature of the asymmetric pressure distribution along the length of the missile body shows that flow characteristics obtained from modelling only a portion of the missile is representative of the flowfield along the full length of the missile body, since the same asymmetric flowfield is repeated along the length of the body (Xueying et al., 1991).

4.2 Effect of Axial and Circumferential Position of A Perturbation on the Flowfield

G.Zilliac et al. (1991) found that at high angles of attack, the flowfield was very sensitive to the axial and circumferential location of surface imperfections. Since asymmetric vortices exhibit a regular bistable state behaviour, the axial and circumferential location of the surface imperfection could trigger either one of the bistable states.

Xuei et al. (2000) defines the two regular states of asymmetric flowfields as *Left Vortex Pattern* and *Right Vortex Pattern*. According to Xuei et al. (2000) the left vortex pattern is defined by the right vortex separating first from the body and the left vortex separating at a different axial location on the body. The left vortex remains closer to the body while the right vortex is further away from the body until it detaches. For the right vortex pattern, the opposite occurs (Xuei et al., 2000).

4.2.1 Grid generation

Effect of the axial location of the perturbation

Perturbation I, from Section 4.1, was placed at the following axial locations on a $8.1D$ missile body, such as that shown in Figure 4.3:

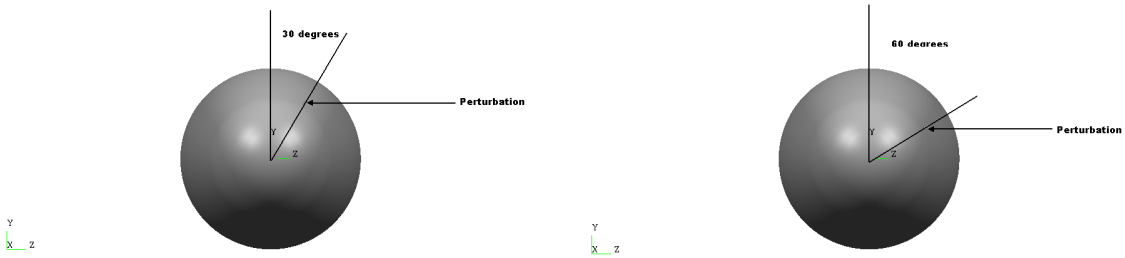
- the nose tip
- $x = 0.06D$
- $x = 0.25D$

Effect of the circumferential location of the perturbation

Perturbation I, fixed at an axial location of $x = 0.25D$ was placed at 2 different circumferential locations:

- 120°, that is 30° clockwise from the lateral meridian, (Figure 4.17a).
- 150°, that is 60° clockwise from the lateral meridian, (Figure 4.17b).

The two circumferential positions were chosen based on Degani and Schiff (1991) findings that the most sensitive circumferential locations to place a disturbance on a pointed slender body are between 90°, which is the lateral meridian and 140°, which is 50° to the right of the lateral meridian. The choice of the second circumferential location was to determine if blunt ogive bodies were less sensitive to the circumferential position of the geometric perturbation.



(a) Geometric perturbation at $\phi = 120°$ (b) Geometric perturbation at $\phi = 150°$

Figure 4.17: Front view showing the two different circumferential positions of the perturbations

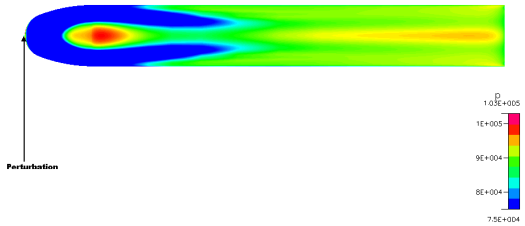
The grid described in Section 4.1, was used to determine the effect of the axial and the circumferential location of the geometric perturbation.

The investigation was only carried out at an angle of attack of 40° at Mach 0.8 and the initial conditions specified in Section 2.1. The Menter-SST turbulence model was used along with Roe's FDS algorithm with the Osher-C flux limiter.

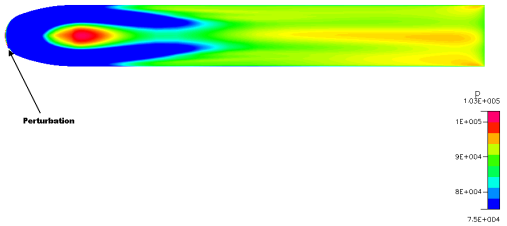
4.2.2 Results

Effect of the axial location of the perturbation

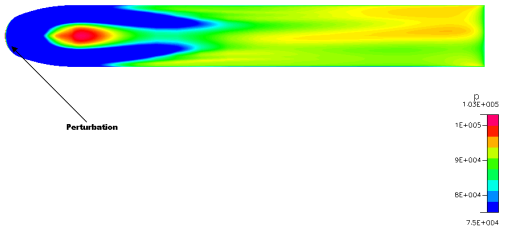
The surface pressure distributions for various pertrubation axial locations are shown in Figure 4.18.



(a) Geometric perturbation at tip of nose



(b) Geometric perturbation at $x = 0.06D$

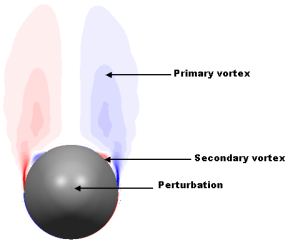


(c) Geometric perturbation at $x = 0.25D$

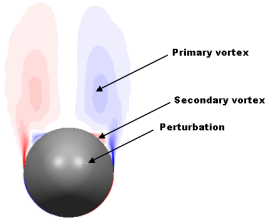
Figure 4.18: Surface pressure distributions on missile bodies with perturbations at different axial locations ($\alpha = 40°$)

Figure 4.18a shows that the surface pressure distribution along the length of the body is symmetrical, which is very different from the results obtained by Degani (1992) on a pointed slender body. The grid used by Degani (1992) was similar but the nose geometries differed, which resulted in the geometric perturbation being at an angle on the body, thus forcing a steady asymmetric flowfield. The perturbations located at axial locations of $x = 0.06D$ and $x = 0.25D$, in Figures 4.18b and 4.18c, produce asymmetric surface pressure distributions. Even thought the geometric perturbations were placed on the right of the body centre-line, the geometric perturbation, $0.06D$ from the nose tip, forced the left vortex to separate before the right vortex. This is indicated by the shorter low pressure region on the left of the missile body surface in figure 4.18b. The perturbation that was placed $0.25D$ from the nose tip, forced the right vortex to separate first, as indicated by the shorter low pressure region on the right of the missile body centre-line in Figure 4.18c. This demonstrates that the perturbations at different axial locations were able to trigger two different stable states of asymmetric vortices. Figure 4.18b shows the high pressure region at the rear of the missile body is not as large as the high pressure region in Figure 4.18c. This indicates that the perturbation at $0.06D$ produced an asymmetric flowfield which was not as strong as that produced by the perturbation at $0.25D$.

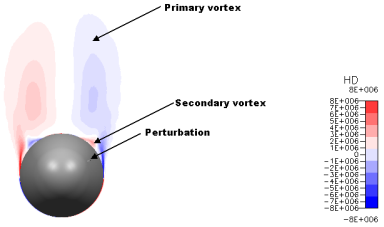
Figures 4.19 and 4.20 show flowfield development at axial locations of $4D$ and $6D$ by means of helicity density contours.



(a) Perturbation at tip of nose



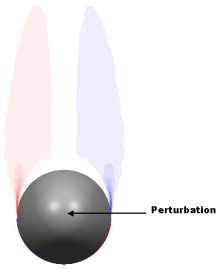
(b) Perturbation at $x = 0.06D$



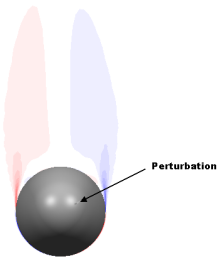
(c) Perturbation at $x = 0.25D$

Figure 4.19: Helical density contours at $x = 4D$ at $\alpha = 40°$ for the perturbations at different axial locations

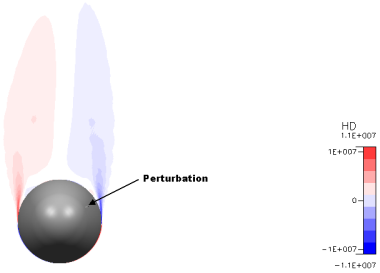
Figure 4.19 shows the formation of primary and secondary vortices on the missile body. Figure 4.19a shows that the symmetric primary vortices formed, even though a perturbation was present at the tip of the nose. This indicates that the perturbation located at the nose was ineffective in creating a steady asymmetric vortex system. Figure 4.19b illustrates that the left primary vortex, which is represented by the red region, is larger than the right primary vortex which is an indication that the left vortex separated from the body first. This is further confirmed by the shorter low pressure region on the left of the missile body surface in Figure 4.18b. The left secondary vortex is larger than the right secondary vortex. The asymmetric flowfield in Figure 4.19c is different to that shown in Figure 4.19b, even though both perturbations were placed at the same declination. In Figure 4.19c, the right primary and secondary vortices are larger than the left primary and secondary vortices, indicating that the separation occurred on the right side first.



(a) Geometric perturbation at tip of nose



(b) Geometric perturbation at $x = 0.06D$

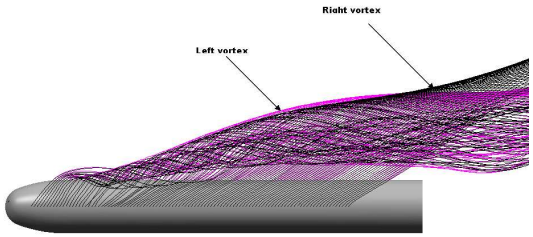


(c) Geometric perturbation at $x = 0.25D$

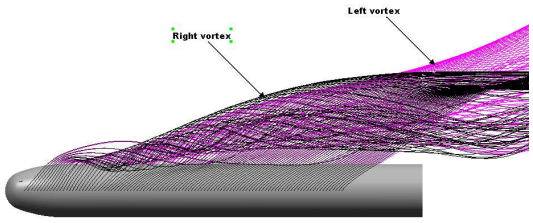
Figure 4.20: Helical density contours at $x = 6D$ at $\alpha = 40°$ for the perturbations at different axial locations

Figure 4.20 shows vortex formation at an axial location of $6D$ due to the different positioned geometric perturbations. In Figure 4.19 at an axial location of $4D$ from the missile nose the two different steady asymmetric states are not clearly visible. Further downstream on the body, at an axial location of $6D$ the different asymmetric states can be clearly seen. The left vortex in Figure 4.20b is larger than the right vortex and the right vortex in Figure 4.20c is larger than the left vortex.

Ribbon traces, in Figure 4.21, show the difference in the resulting vorticity patterns for the two geometric perturbations.



(a) Geometric perturbation at $x = 0.06D$



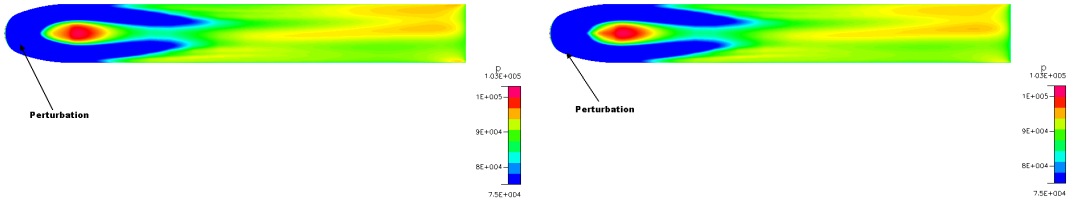
(b) Geometric perturbation at $x = 0.25D$

Figure 4.21: Streamlines on body at $\alpha = 40°$ for the perturbations at different axial locations

In Figure 4.21a, the left vortex separates and is initially higher than the right vortex. Near the base, the right vortex rises above the left. In Figure 4.21b, the right vortex is initially higher than the left vortex while the left vortex is higher near the base. This further demonstrates the alternating nature of the steady asymmetric flow identified in Figure 4.16.

Effect of the circumferential location of the perturbation

The surface pressure distributions for the geometric perturbations at circumferential locations of 120° and 150° are shown in Figure 4.22



(a) Geometric perturbation at $\phi = 120°$ (b) Geometric perturbation at $\phi = 150°$

Figure 4.22: Surface pressure distribution on missile bodies with geometric perturbations at different circumferential locations ($\alpha = 40°$)

The surface pressure distributions on both missile bodies are very similar. The asymmetric pressure distribution indicates that the flowfield for both will be asymmetric and since the high surface pressure region is on the same half of the body, both geometric perturbations triggered off the same regular state.

Helicity density contours were plotted at an axial location of $x = 4D$ from the nose to show the steady asymmetric vortex formation.



(a) Geometric perturbation at $\phi = 120°$ (b) Geometric perturbation at $\phi = 150°$

Figure 4.23: Helical density contours at $x = 4D$ at $\alpha = 40°$ for the geometric perturbations at different circumferential positions

Figure 4.23 shows the primary and secondary vortex formation for the two geometric perturbations. The resultant flowfield for both look very similar. The right vortex is larger than the left vortex, indicating that it separated first from the body. This is confirmed by the shorter low pressure region on the right of the missile body centre-line in Figures 4.22a and 4.22b.

4.2.3 Discussion

Effect of the axial location of the perturbation

Figures 4.19 and 4.20 illustrate that the flow at high angles of attack is sensitive to the axial location of the perturbation. The perturbations, situated at two different axial locations, forced two different asymmetric states. It was thought that since the perturbation was located on the right side of the body, the right vortex would separate first for both geometric perturbations.

Figures 4.19b and 4.21a show that the geometric perturbation at $0.06D$ triggered the right vortex pattern since the left vortex is further away from the body. Figures 4.19c and 4.21b show that the geometric perturbation at $0.25D$ triggered the left vortex pattern since the right vortex separated from the body before the left vortex as seen in Figure 4.18c. This is illustrative of the evidence provided by Champigny (1994) that two strong, counter-rotating vortices cannot co-exist symmetrically at high angles of attack and that a perturbation is required to force the unsteady, symmetric vortices into a stable, asymmetric state. However, the bistable state that is triggered by the geometric perturbation cannot be predetermined, even if the perturbations are located at the same circumferential location.

It was found that distance was an important factor in the degree of asymmetry obtained on a blunt ogive body. When the geometric perturbation was placed at the tip of the nose, symmetric vortices were generated since the perturbation was symmetric. The geometric perturbation at $0.25D$ resulted in a stronger asymmetric flowfield than the perturbation at $0.06D$. This gives the indication that to simulate asymmetric vortices on a blunt ogive body, the geometric perturbation should be placed away from the nose tip. However, the geometric perturbation cannot be placed to far down the length of the missile body as the steady asymmetric vortex formation would no longer be observed on the body but rather further downstream from the body.

Since the geometric perturbation located $0.25D$ away from the nose of the missile resulted in a higher degree of flow asymmetry, this geometric perturbation was chosen for further investigations. The higher degree of asymmetry would help in gaining an understanding of the effect the strakelets would have on the asymmetric flowfield (mentioned in Section 1.3).

Effect of the circumferential location of the perturbation

The surface pressure distributions in Figure 4.22 and the helicity density contours in Figure 4.23 show that the flowfields for the two perturbations, located at different circumferential locations are very similar. Both perturbations triggered the same bistable state.

Also evident is that the perturbation located at $\phi = 150^\circ$ falls outside the limitations specified by Degani and Schiff (1991). This difference is probably due to Degani and Schiff (1991) researching asymmetric flow on a pointed, slender body as opposed to the blunt ogive used in this study. The exact methods used by Degani and Schiff (1991) serve as guidelines and cannot be directly used.

Since the same asymmetric vortex state was triggered by perturbations located at $\phi = 120^\circ$ and $\phi = 150^\circ$, the perturbation located at 120° was chosen for the remainder of the study, due to it's position falling within the limit specified by Degani and Schiff (1991).

4.3 Conclusion

Perturbation I had the least effect on the flowfield and resulted in a negligible value of side force at 5° angle of attack. The presence of perturbation I on the missile forebody also resulted in the formation of steady asymmetric vortices at angles of attack of 20° and 40°. The resultant steady asymmetric flowfield on the body, due to perturbation I, was characteristic of blunt ogive bodies since the degree of asymmetry introduced by the geometric perturbation was low. When the length of the missile body was increased, perturbation I was able to simulate the alternating behaviour of steady asymmetric vortices. It was also shown that the steady flow asymmetry originated from a convective instability in the flowfield as first identified by Degani and Schiff (1991).

Therefore perturbation I will be used in Chapter 5 to create a steady asymmetric flowfield so as to determine the effect of the strakelets on steady asymmetric flow.

A geometric perturbation located at the tip of the nose had no effect on the flowfield and the flow remained symmetric even at 40° angle of attack. It was found that it was possible to excite different stable states of steady asymmetric vortices by placing the geometric perturbations at different axial locations on the body. It was

also found that as the geometric perturbation distance from the nose increased, the degree of asymmetry increased.

The axial location of perturbation I was set at $0.25D$, as the steady flow asymmetry was the most pronounced of the two geometric perturbation locations tested and the effect of the strakelets on the asymmetric vortices could be easily observed.

The circumferential location of the geometric perturbation was also an important factor in creating a steady asymmetric flowfield. However it was found that for a blunt nose body, the geometric perturbation could be at an angle of 120° or 150° and a steady asymmetric flowfield would still be created. Both yielded the same steady asymmetric vortex regular state as well.

The circumferential position of perturbation I was set at 120° as this fell within the circumferential limits set by Degani and Schiff (1991), even though Degani and Schiff (1991) used a pointed slender body.

5 Effect of Strakelets on Steady Asymmetric Vortices

As mentioned in Section 1.2, the large side forces on a missile at high angles of attack, due to the formation of steady asymmetric vortices, need to be controlled or alleviated so that the required missile performance can be obtained (Champigny, 1994). Based on the research by Yuan and Howard (1991) that forebody miniature strakes (strakelets) reduced side forces at high angles of attack, four strakelets were added in the '×' configuration to the nose of a missile body of revolution (referred to as missile body) in an attempt to eliminate the large side forces, by forcing steady vortex symmetry. The strakelets had to be large enough to force vortex symmetry so that symmetric vortices could interact with the control surfaces, placed at the rear of the full length missile body. The strakelets could not, however, contribute to the overall normal force of the missile as this would force the missile nose to pitch-up resulting in an unstable missile. Experimental data in Figure 5.1 shows that the magnitude of the side force coefficient was reduced with the addition of the strakelets on a full length missile body with tail fins at the rear.

Figure 5.1 illustrates the side force coefficient on a body with 4 control surfaces (body-tail configuration) with and without strakelets.

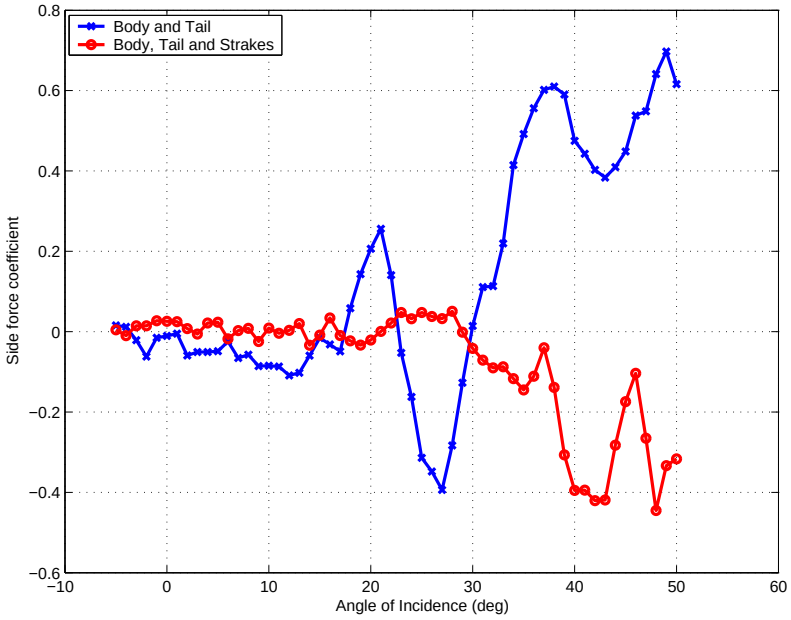


Figure 5.1: Comparison of experimental side force data for a body-tail configuration with and without strakelets

When the strakelets were not placed on the body-tail configuration, side forces developed on the missile body at angles of attack less than 10°. The side force coefficient fluctuated non-linearly from approximately 0.2 at 20° angle of attack to approximately -0.4 at 25° to 0.6 at 38° angle of attack.

When the strakelets were added to the body-tail configuration, side forces developed on the body at approximately 30° angle of attack. The highest value for the side force coefficient was approximately -0.42 at approximately 48°, which is lower than that obtained when the strakelets were absent.

As identified in Section 1.1.3 the onset of steady vortex asymmetry is dependent on the model used as steady vortex asymmetry is as a result of surface imperfections on the model. These imperfections differ from model to model (Champigny, 1994).

This study was conducted in order to gain an understanding of the effect the strakelets had on the steady asymmetric flowfield and is thus of a purely qualitative nature.

The strakelets' height, the strakelets' leading edge position and the strakelets' chord length were identified as the critical factors that would affect the asymmetric flowfield on the body and thus the side force acting on the body (DAS, 2004). Using the

full factorial Design of Experiments (DOE) methodology, as described by Barrentine (1999), Table 5.1 was set up.

Table 5.1: Coefficients for Effects in a 2^3 Experiment

Runs	X	Y	Z
1	-	-	-
2	+	-	-
3	-	+	-
4	+	+	-
5	-	-	+
6	+	-	+
7	-	+	+
8	+	+	+

In Table 5.1 X represents the strakelet height, Y represents the strakelet leading edge position and Z represents the strakelet chord length position. The base 2 represents the two levels that the variable can have, that is the variable can have a high value ('+') or the variable can have a low value ('−') and the exponent 3 represents the number of variables present in the experiment (Barrentine, 1999). The '+' signs in Table 5.1 indicates a changing variable while the '−' indicates that the variable is held constant. From Table 5.1 it was decided that the following effects would be investigated:

- The effect of changing the height of the strakelets on steady asymmetric vortices. (Run 2 from Table 5.1)
- The effect of changing the axial position of the nose strakelets on steady asymmetric vortices. (Run 3 from Table 5.1)

The effect of the strakelet chord length was not considered and thus runs $5 - 8$ are not applicable. Run 1 represents the baseline run with all variables constant. This simulation validates the simulation methodology from Chapter 4. Runs 2 and 3 are discussed Sections 5.1 and 5.2 respectively. Run 4 was not considered as it entails investigating the effect of varying both the strakelet height and the strakelet leading edge position in a single run. In this way the mutual interaction between the two parameters would be investigated, however in order to perform run 4, runs 2 and 3 are required first so that the influence of the individual parameters can be determined before investigating their mutual influence.

5.1 Effect of Changing the Span of the Strakelets

5.1.1 Grid generation

Figure 5.2 shows the geometry modelled for the CFD simulations. The geometry of the strakelets were similar to that used in the wind tunnel test.

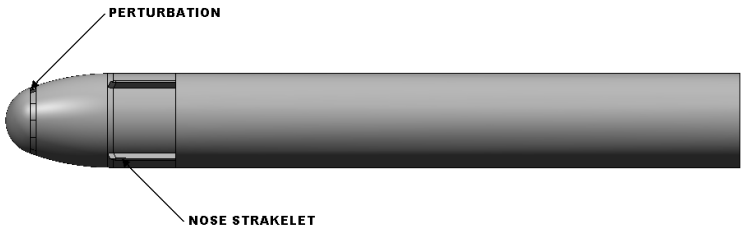


Figure 5.2: Geometry of missile with nose strakelets

The strakelets used in the experiments had a height of $0.06D$, a chord of $0.8D$ and a width of $0.06D$. The leading edge of the strakelets was $1D$ from the nose tip. Due to the alternating behaviour of steady asymmetric vortices along the length of the missile body, only $8.1D$ of the missile body was once again modelled. Perturbation I, from Section 4.1 was placed on the nose, a distance of $0.25D$ away from the nose tip and at a circumferential location of 120°, 30° clockwise from the lateral meridian, to create a steady asymmetric flowfield.

Three different strakelet heights, denoted by b, were investigated:

- Model A strakelets: $b = 0.06D$
- Model B strakelets: $b = 0.09D$
- Model C strakelets: $b = 0.13D$

The leading edge for the three different models was fixed at $1D$ from the nose tip.

The structured grid used in this study is shown in Figure 5.3.

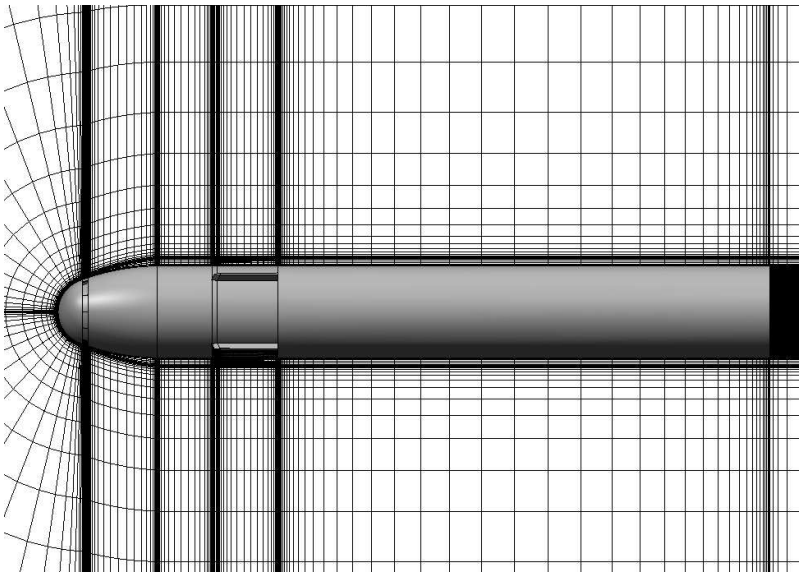


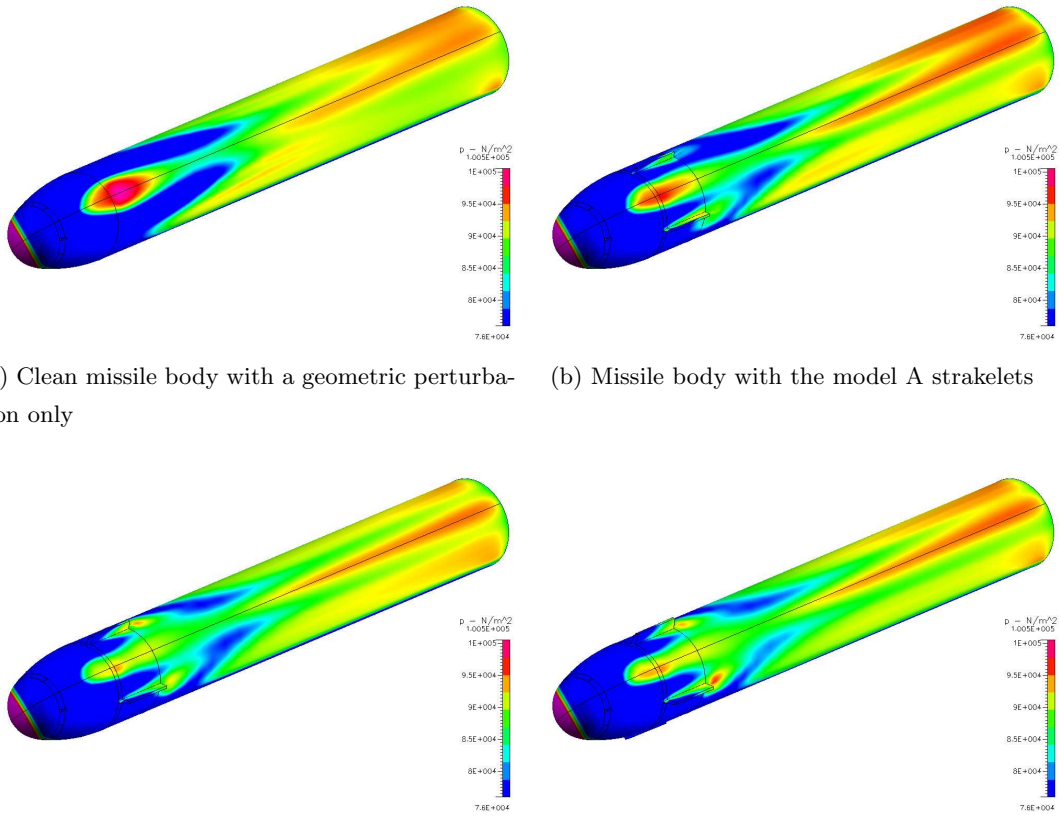
Figure 5.3: A close view of the structured grid constructed on the missile-strakelet geometry

The grid consisted of approximately 280 circumferential grid points extending around the body, 60 radial grid points extending from the body surface to the farfield boundary and 140 axial grid points extending from the tip of the nose to the outlet boundary. Grid points in the axial and radial locations near the strakelets were increased so as to capture the flowfield on the strakelets.

Simulations were only carried out at an angle of attack of 40° since at this angle of attack steady vortex asymmetries were most pronounced (as shown in Figure 5.1) and thus the effect of the strakelets on the steady asymmetric flowfield could be easily observed. The Menter-SST turbulence model was used. Roe's FDS with the Osher-C limiter was used to solve the RANS equations.

5.1.2 Results

Figure 5.4 shows the pressure distribution on the top surface (leeward side) of the missile bodies. The clean missile body with the geometric perturbation, from Section 4.1, is also included for comparison between the different results.



(a) Clean missile body with a geometric perturbation only

(b) Missile body with the model A strakelets

(c) Missile body with the model B strakelets

(d) Missile body with the model C strakelets

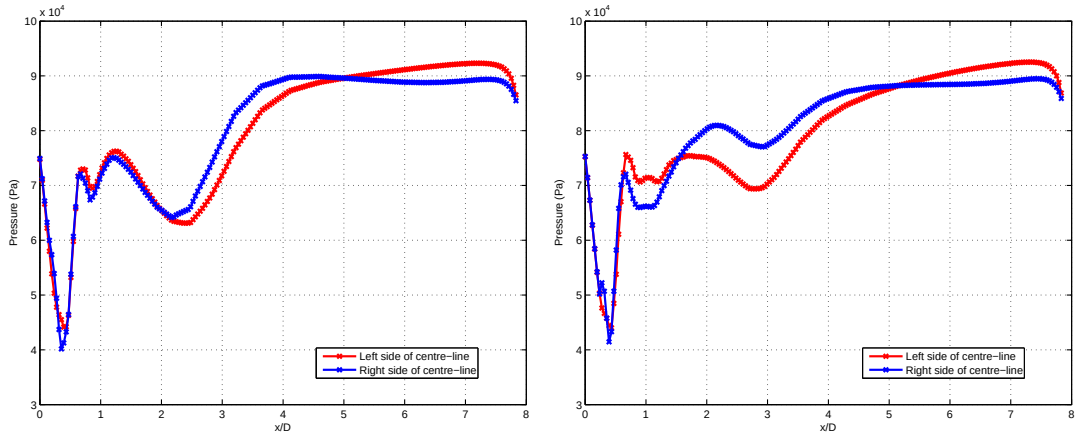
Figure 5.4: Surface pressure distributions on the strakelet models with different spans at 40° angle of attack

The asymmetric surface pressure distributions on the missile bodies with the models A and C strakelets respectively, in Figures 5.4b and 5.4d indicates that the resultant flowfields are asymmetric. The model A strakelets were used in the experimental tests and it resulted in an asymmetric flowfield at 40° angle of attack, as shown in Figure 5.1. This indicates that the CFD simulations do qualitatively match the experimental flowfields. The symmetric surface pressure distribution at the rear of the missile body in Figure 5.4c indicates that the model B strakelets forced the formation of steady symmetric vortices.

Figures 5.4c and 5.4d have two sets of low pressure regions on the leeward side of

the body. The first set of low pressure regions end almost at the trailing edge of the strakelets. This is due to vortex separation off the strakelets. The second set of low pressure regions is on the cylindrical part of the missile body. This is where the flow from the bottom strakelets separate on the leeward side of the missile body and feed into the separated primary vortices. In Figure 5.4b the two sets of low pressure regions on the body are joined. Indicating that the two vortices, formed due to flow interaction with the top strakelets, are still attached to the body surface when flow from the bottom strakelets separate on the leeward side and feed into the vortices.

Figure 5.5 shows the surface pressure distribution on the leeward side of the missile body, $0.06D$ on either side of the body centre-line, for the different models. This is a numerical representation of the surface pressures, allowing for a clearer identification of the flow asymmetries.



(a) Clean missile body with a geometric perturbation only

(b) Missile body with the model A strakelets

(c) Missile body with the model B strakelets

(d) Missile body with the model C strakelets

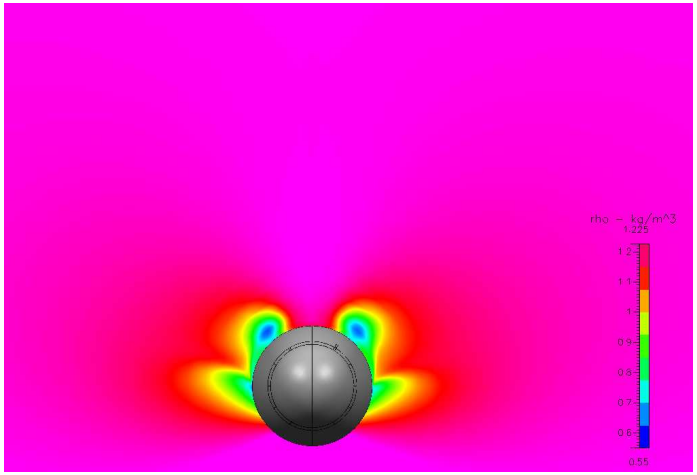
Figure 5.5: The surface pressure distribution along the length of the body for the strakelet models with different spans

Figure 5.5b shows that the difference in surface pressure distribution at the rear of the missile body, between $x = 6D$ and $x = 8D$, is very similar to the surface pressure difference at the corresponding axial locations in Figure 5.5a. Flow interacts with the model A strakelets at approximately $1D$ from the nose tip. The surface pressures on either side of the missile body centre-line are unequal, indicating that the flow is asymmetric when it interacts with the strakelets. The trailing edge of the strakelets are at $1.9D$ from the nose tip. At this axial location the surface pressures are different, indicating that the formed vortices are asymmetric. The different surface pressures along the length of the body shows that the model A strakelets were not able to eliminate the asymmetry introduced by the geometric perturbation on the missile nose.

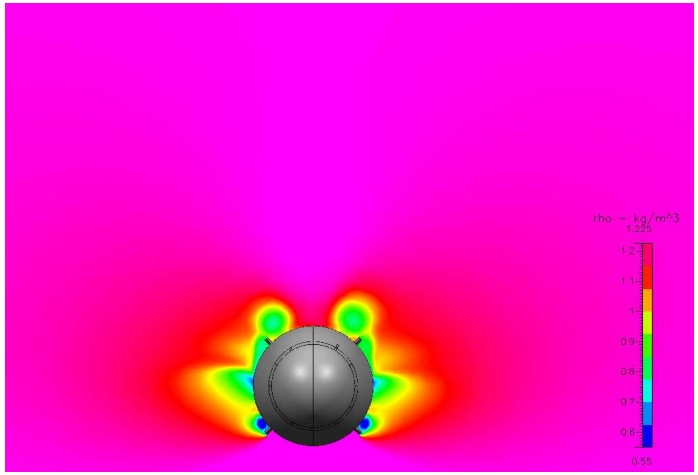
In Figure 5.5c it is evident that from an axial location of approximately $3D$ from the nose tip, the surface pressures on either side of the body centre-line are equal, indicating that the resultant flowfield has symmetric vortices. The flow is asymmetric when it interacts with the leading edge of the model B strakelets at $1D$, as can be seen by the difference in surface pressures across the missile body centre-line. At the trailing edge of the strakelets, surface pressures across both halves of the body are different but this difference is smaller and opposite in sign than that in Figure 5.5b at the corresponding axial location.

The difference in surface pressures at the rear of the missile body, between $x = 6D$ and $x = 8D$ in Figure 5.5d is smaller than the difference at the corresponding axial locations in Figures 5.5a and 5.5b. Even though the flow is asymmetric when it interacts with the leading edge of the model C strakelets, the surface pressures along the length of the body surface from $x = 1D$ to $x = 1.9D$ are almost equal. Thus the flow became symmetric when it interacted with the strakelets. However, as the flow developed along the remainder of the body length, the asymmetry introduced by the geometric perturbation developed, resulting in asymmetric vortices at the rear of the body.

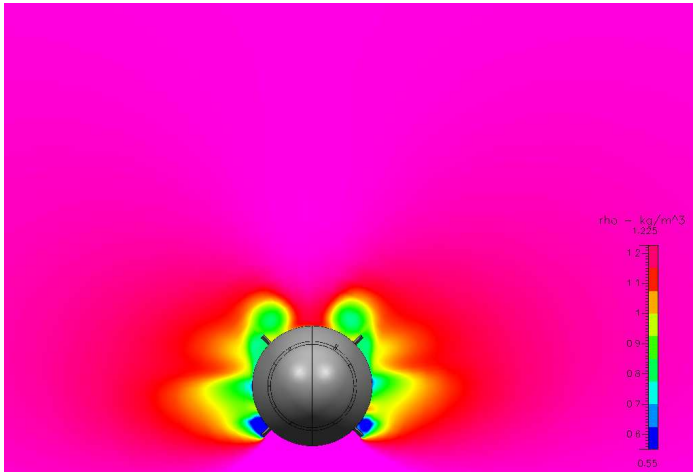
Cross-sections of the flow at different axial locations on the body are shown in Figures 5.6 to 5.9 using density colour flood maps. These show the flow development along the length of the missile body. Since it is the interaction of the flowfield with the strakelets that is of importance, density colour maps are sufficient.



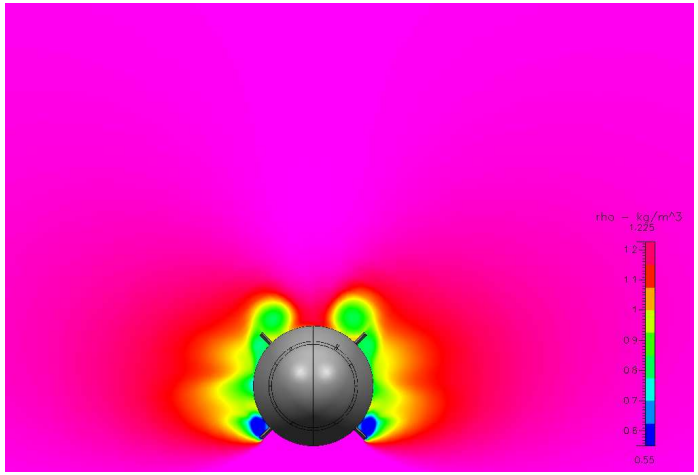
(a) Clean missile body with a geometric perturbation only



(b) Missile body with the model A strakelets



(c) Missile body with the model B strakelets



(d) Missile body with the model C strakelets

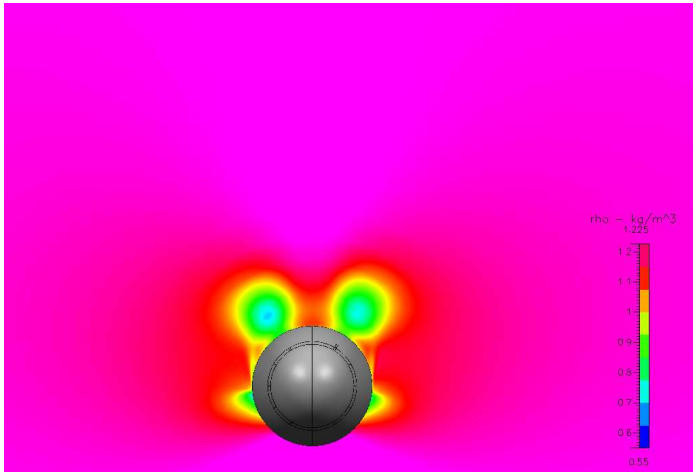
Figure 5.6: Flowfield on the missile bodies with strakelets with different spans at $x = 1.4D$ at an angle of attack of 40°

Figure 5.6 shows flow interaction with the strakelets, $1.4D$ from the nose tip. The right vortex in Figure 5.6b is larger than the left vortex. Both vortices are still attached to the body. Figure 5.5b shows that at the corresponding axial location, the surface pressure on the left of the body is slightly higher than that on the right, indicating that the left vortex has less contact with the body than the right vortex. Flow is attached to the bottom strakelets.

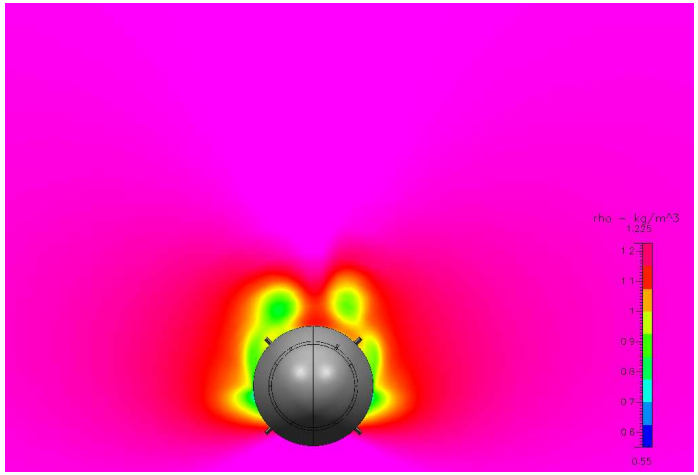
The right vortex on the missile body with the model B strakelets in Figure 5.6c is slightly larger than the left vortex. The higher surface pressure on the left side of the body at $x = 1.4D$ in Figure 5.5c indicates that due to the small size of the left vortex it has less contact with the body than the right vortex, even though both vortices are still attached to the body surface.

In Figure 5.6d two vortices of similar size form at the top strakelets. The almost equal surface pressures at $x = 1.4D$ in Figure 5.5d indicates that both vortices are of similar size.

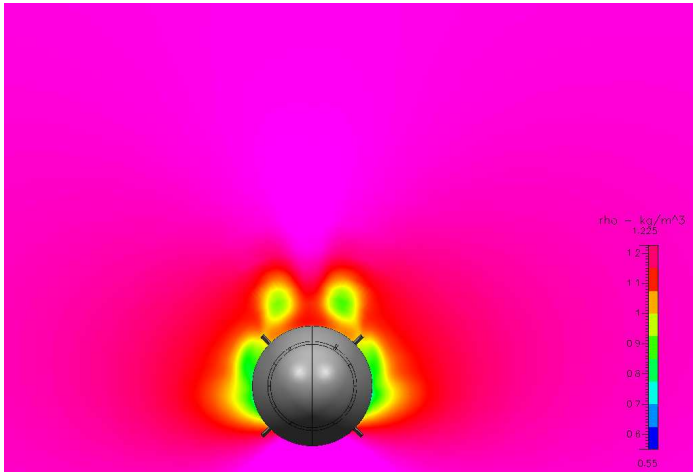
The trailing edge of the three different strakelets is located at $1.9D$. Figures 5.7 to 5.9 show flow development on the missile body behind the strakelets.



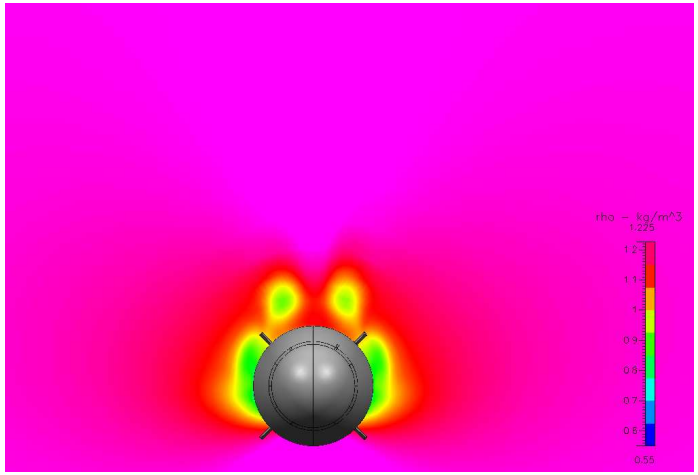
(a) Clean missile body with a geometric perturbation only



(b) Missile body with the model A strakelets



(c) Missile body with the model B strakelets



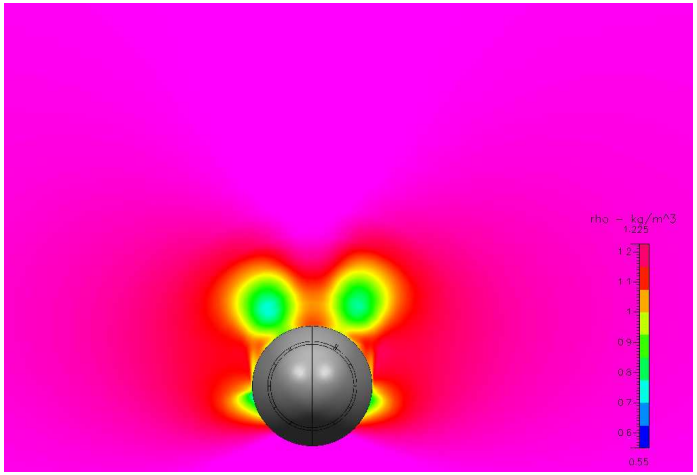
(d) Missile body with the model C strakelets

Figure 5.7: Flowfield on the missile bodies with strakelets with different spans at $x = 2.5D$ at an angle of attack of 40°

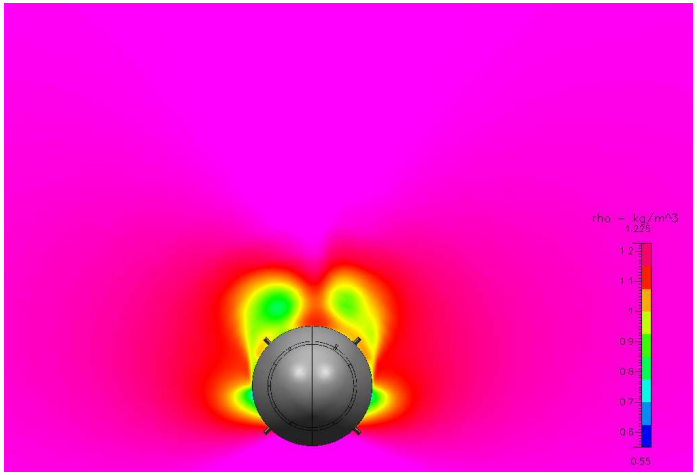
In Figure 5.7 the flowfield $0.4D$ behind the strakelets is shown. In Figure 5.7b the right vortex is smaller than the left vortex and it is further away from the body surface than the left vortex. This results in a higher surface pressure on the right of the missile body centre-line as shown in Figure 5.5b at $2.5D$. The flow from the bottom strakelets has moved around the body surface towards the leeward side. The flow on the right is still attached to the side of the body, while the flow on the left has separated and feeds into the left vortex, strengthening it.

In Figure 5.7c flow from the bottom strakelets moves around the missile body surface, towards the leeward side. Both vortices that formed at the top strakelets have separated, with the right vortex being larger than the left vortex. The left vortex is slightly further away from the body than the right vortex, resulting in a higher surface pressure on the left side of the body surface, as seen in Figure 5.5c at $2.5D$.

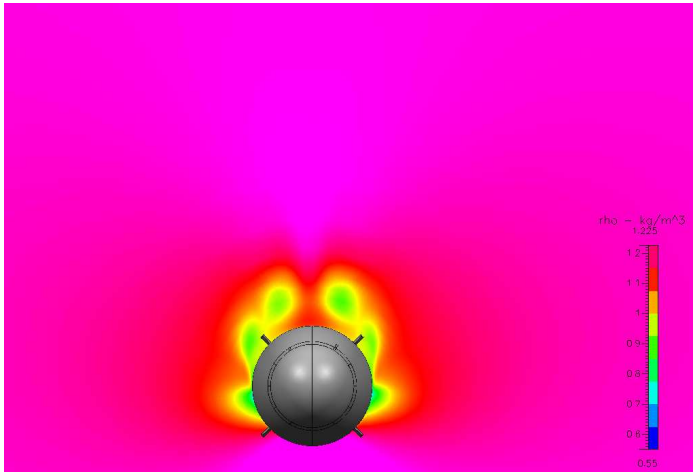
Flow from the bottom strakelets in Figure 5.7d moves towards the leeward side of the body surface. The right vortex is slightly smaller than the left vortex but both vortices are almost at the same height above the missile body surface, resulting in the almost equal surface pressures on the both halves of the missile body in Figure 5.5d at the corresponding axial location.



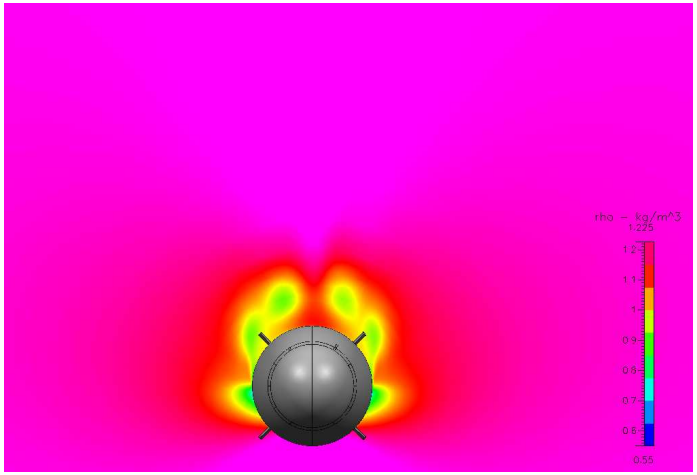
(a) Clean missile body with a perturbation only



(b) Missile body with the model A strakelets



(c) Missile body with the model B strakelets



(d) Missile body with the model C strakelets

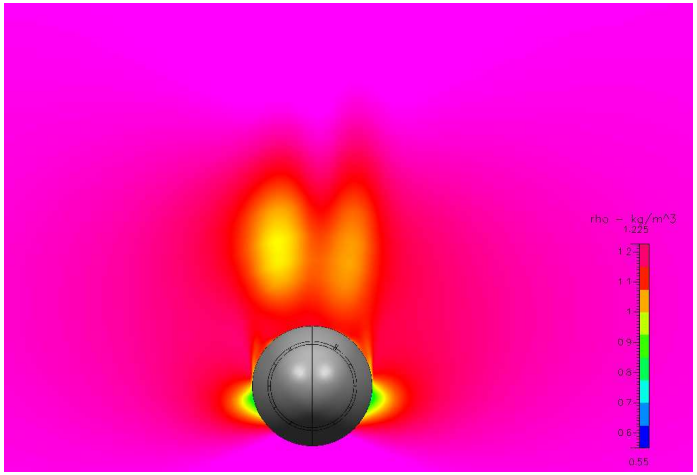
Figure 5.8: Flowfield on the missile bodies with strakelets with different spans at $x = 2.8D$ at an angle of attack of 40°

In Figure 5.8b flow separates on the right side of the missile body and feeds into the small, right vortex. The left vortex is larger than the right vortex due to flow separation occurring on the left at $x = 2.5D$ (Figure 5.7b). The flowfield in Figure 5.8b is asymmetric as indicated by the different heights of the vortices from the body surface, which results in unequal surface pressures in Figure 5.5b at the corresponding axial location.

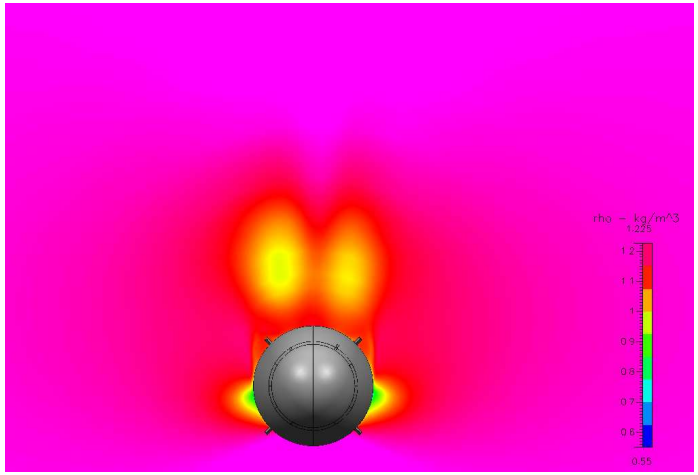
In Figure 5.8c the right vortex is larger than the left vortex. Both vortices are almost at the same height above the body surface, resulting in the almost equal surface pressures, seen in Figure 5.5c at the corresponding axial location. The flow on both sides of the body separates at the same axial location on the body surface. Therefore both vortices, that formed at the top strakelets will be strengthened at the same axial location on the body surface.

Flow around the missile body separates at the same axial position in Figure 5.8d as well. The higher surface pressure on the right of the missile body centre-line in Figure 5.5d, at $x = 2.8D$ indicates that the right vortex is slightly higher than the left vortex, thus the left vortex would be strengthened by the separated flow before the right vortex, resulting in the two vortices growing with different strengths along the length of the body.

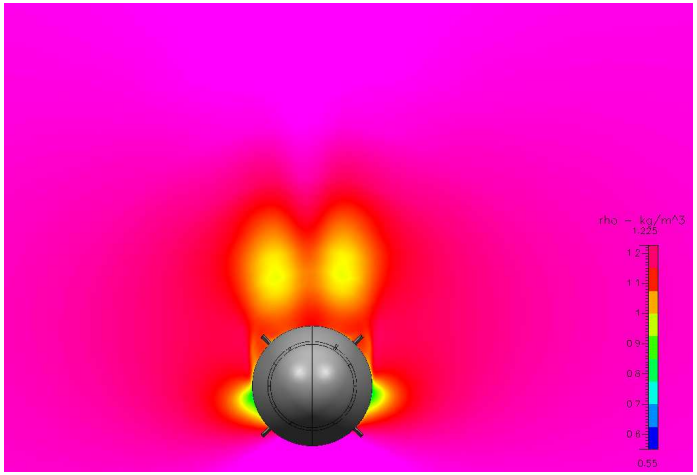
Figure 5.9 shows the flow at the rear of the body, approximately $6D$ from the nose tip.



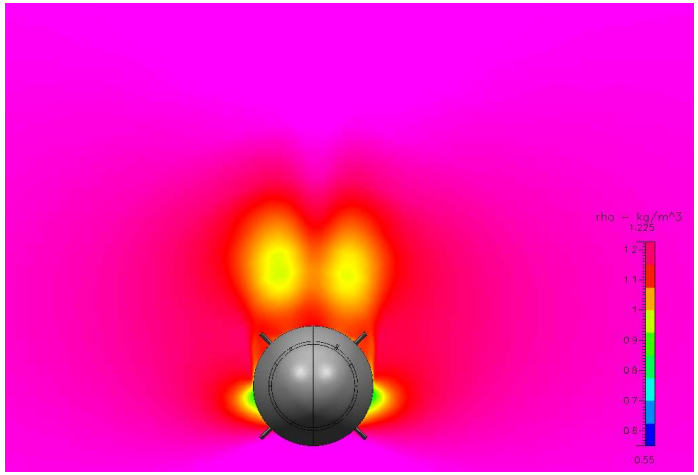
(a) Clean missile body with a perturbation only



(b) Missile body with the model A strakelets



(c) Missile body with the model B strakelets



(d) Missile body with the model C strakelets

Figure 5.9: Flowfield on the missile bodies with strakelets with different spans at $x = 6D$ at an angle of attack of 40°

The resultant asymmetric flowfield in Figure 5.9b is very similar to that of the body and geometric perturbation in Figure 5.9a. The left vortex is further away from the missile body than the right vortex, resulting in the unequal surface pressures at $x = 6D$ in Figure 5.5b.

In Figure 5.9c the resultant vortices are of similar strengths and are approximately the same distance above the body surface. The surface pressures in Figure 5.5c, at the corresponding axial location, are equal. Thus the model B strakelets were able to eliminate the asymmetry introduced by the geometric perturbation on the nose.

The vortex asymmetry in Figure 5.9d is less than the vortex asymmetry in Figure 5.9a. The difference in height between the two vortices is small, as indicated by the small difference in surface pressures in Figure 5.5d at $x = 6D$.

5.1.3 Discussion

The flow over the missile nose is forced to a steady asymmetric state by the geometric perturbation, placed $0.25D$ from the missile nose tip. The leading edge of the three strakelet models are located approximately $0.75D$ behind the geometric perturbation at $x = 1D$. Figures 5.5b, 5.5c and 5.5d show that the surface pressures across both halves of the missile body are unequal at $x = 1D$, thus the flow is asymmetric when it interacts with the leading edges of the three strakelet models.

Flowfield on the missile body with the model A strakelets

From the surface pressure distributions on the missile body with the model A strakelets in Figures 5.4b and 5.5b it can be seen that the resultant flowfield at the rear of the missile body, between axial locations of $6D$ and $8D$, is asymmetric. In Figure 5.6b two vortices formed at the top strakelets, with the right vortex larger than the left one. The surface pressures at the corresponding axial location of $1.4D$ showed that the surface pressure on the left of the missile body centre-line was a little higher than the surface pressure on the right. The lower surface pressure on the right indicates that due to the right vortex being larger than the left vortex, it has more contact with the body surface than the smaller left vortex. The right vortex separates from the body surface first, as indicated by the short low pressure line on the right of the body centre-line in Figure 5.4b. In Section 4.2 it was seen that the geometric perturbation on the missile nose at an axial location of $0.25D$ forced the right vortex to separate first from the body surface (Figure 4.20). Thus

the model A strakelets have retained the right vortex pattern that was triggered by the geometric perturbation. At $x = 1.9D$, the trailing edge of the model A strakelets the vortices are asymmetric, with the the right vortex further away from the missile body than the left vortex, as indicated by the higher surface pressure on the right of the missile body centre-line.

Behind the trailing edge of the model A strakelets, flow from the bottom strakelets, remains attached to the body surface and moves towards the leeward side of the body surface. In Figure 5.7b, flow separates on the left and feeds into the left separated vortex strengthening it. The flow on the right separates at a different axial position on the missile body and feeds into the right separated vortex (Figure 5.8b). The left vortex is strengthened before the right vortex resulting in the asymmetric flowfield in Figure 5.9b. The flow separated on the leeward side, at different axial locations because the short model A strakelets were not able to force the flow to separate sufficiently far from the missile body. The flowfield at $x = 6D$ in Figure 5.9b resembles that in Figure 5.9a of the body with the geometric perturbation only. The asymmetric vortices in Figure 5.9b are stronger than the asymmetric vortices in figure 5.9a, indicated by the different colour intensities.

Flowfield on the missile body with the model B strakelets

The resultant flowfield on the missile body with the model B strakelets is symmetric as indicated by the symmetric surface pressure distributions at the rear of the body in Figures 5.4c and 5.5c. At the trailing edge of the strakelets, $x = 1.9D$, the difference in surface pressures across both halves of the body is smaller than the surface pressure difference at the trailing edge of the the model A strakelets, indicating that the resultant flowfield at the trailing edge of the model B strakelets is less asymmetric. The lower surface pressure on the right side of the body centre-line indicates that the right vortex is closer to the body than the left vortex. The short length of the low pressure region on the left of the body centre-line in Figure 5.4c, indicates that the left vortex separated before the right vortex. In Section 4.2, in Figure 4.20 it was seen that the right vortex separated before the left vortex. Thus the model B strakelets were able to produce strong vortices so that the left vortex separated before the right vortex, changing the vortex pattern triggered by the geometric perturbation. For the missile body with the geometric perturbation only, the right vortex separated before the left vortex and with the addition of the model B strakelets, the vortex pattern changed.

Flow from the bottom strakelets moves along the body surface, towards the top

surface of the body (Figure 5.7c). Both vortices have separated, with the left vortex higher than the right vortex, as indicated by the higher surface pressure on the left in Figure 5.5c at $2.5D$. At $x = 2.8D$ the flow on either side of the body centre-line separates and feeds into the separated vortices at the same axial position on the missile body. This is unlike the flow separation for the model A strakelets where the flow on the left separated at $x = 2.5D$ and the flow on the left separated at $x = 2.8D$. Thus the larger height of the model B strakelets allowed for the bottom strakelet to force the flow to separate sufficiently far from the body, so that flow separation on the leeward side of the missile body would not be influenced by the asymmetry introduced by the geometric perturbation on the missile nose. The resultant flowfield, $6D$ away from the nose tip in Figure 5.9c shows that the vortices at the rear of the missile body are symmetric.

Flowfield on the missile body with the model C strakelets

It was thought that since the model B with a height of $0.09D$ was able to force the asymmetrically triggered flow to become symmetric, the model C strakelets, with a height of $0.13D$ would also force vortex symmetry. The asymmetric surface pressure distribution in Figures 5.4d and 5.5d indicates that this was not the case. However, the difference in surface pressures across both halves of the body between $6D$ and $8D$ is smaller than the difference in surface pressures on the body and geometric perturbation at the corresponding axial locations in Figure 5.5a.

At $x = 1.9D$, the trailing edge of the model C strakelets, the flowfield is almost symmetric, as indicated by the almost equal surface pressures on the left and right side of the body centre-line at the corresponding axial location in Figure 5.5d. Even though the flowfield was asymmetric when it interacted with the strakelets at approximately $1.3D$ from the nose tip, the flowfield was made symmetric, as indicated by the equal surface pressures at the corresponding axial location in Figure 5.5d. The flow remained symmetric for the entire length of the model C strakelets up to it's trailing edge at $x = 1.9D$. This is unlike the flow on the model A strakelets where surface pressures on the body alternate for the length of the strakelets and the surface pressures on the body with the model B strakelets have an almost constant difference for the length of the strakelets. The large height of the model C strakelets forced the formation of strong symmetrical vortices only on the strakelets so that the flow on the strakelets remains symmetric. However, at approximately $x = 2D$ the asymmetry, which was not visible on the strakelets, begins to develop.

In Figure 5.8d, the flow from the bottom strakelets separates at the same axial

position on the body and feeds into the two separated vortices. Due to the larger height of the model C strakelets, the flow from the bottom strakelets were not influenced by the asymmetry present in the flowfield and thus separated at the same axial position on the body. Since the left vortex is larger and closer to the body than the right vortex, the separated flow on the left will feed into the left vortex before the separated flow on the right feeds into the right vortex. The larger left vortex will be strengthened first. Thus the already asymmetric vortices will develop asymmetrically along the remainder of the missile body length, resulting in the asymmetric flowfield seen in Figure 5.9d.

Effect of strakelets on normal force coefficient

An interesting observation was made when the normal force coefficient, at 40° angle of attack, for the missile bodies with the three strakelet models were compared to that of the missile body with the geometric perturbation only. It was found that the normal force coefficient for the models with strakelets was less than that of the missile body with the geometric perturbation only. (Table 5.2).

Table 5.2: Comparison of normal force coefficients for the strakelet models with different spans

The model	C_N
Body and perturbation	4.303
The model A	4.150
The model B	3.879
The model C	4.0550

This phenomenon was also observed in the data obtained experimentally. The result shown below is for a body, strakelets and tail configuration (Figure 5.10).

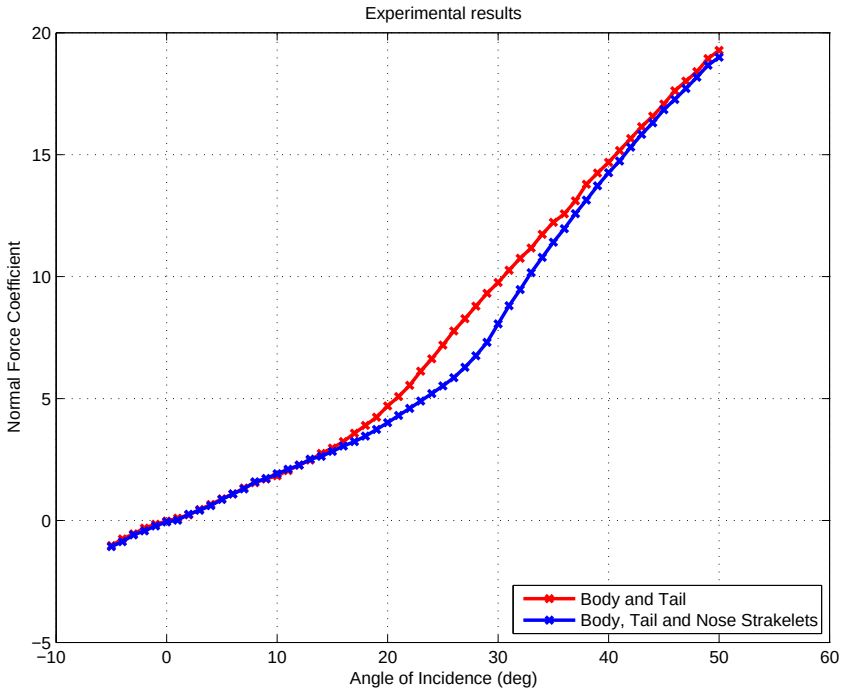


Figure 5.10: The effect of the strakelets on the normal force coefficient

This effect was also noted by Ericsson and Reding (1991). The asymmetric vortex pattern contributed to the normal force on the nose and did not result in it being reduced, as was expected. The vortex induced normal force on the body is due to the movement of steady asymmetric vortices. For steady asymmetric flow one vortex moves further away from the body while the other remains tucked in between the body and the outer vortex, as discussed in Section 1.1.3. This phenomenon results in an increase in normal force and an increase in the interference effects of the forebody vortices on the aft body tail surfaces. The strakelets force vortex symmetry by lifting the lower asymmetric vortex up and outboard, resulting in a loss of lift (Ericsson and Reding, 1991). The normal force on the missile body with the model B strakelets is lower than that on the missile bodies with the model A or C strakelets, since it was able to lift the inner vortex sufficiently to force vortex symmetry more than the model A and C strakelets.

5.2 Effect of Changing the Axial Position of the Strakelets

5.2.1 Grid generation

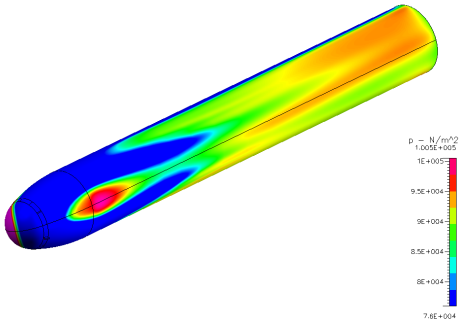
The strakelets span was fixed at $0.09D$. The leading edge of the strakelets were positioned at three different axial (x) locations from the nose.

- The model D: $x = 0.5D$
- The model B: $x = 1D$
- The model F: $x = 1.3D$

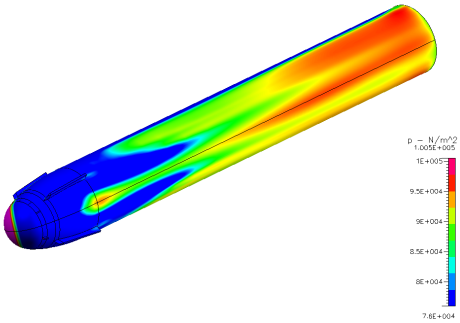
The model B strakelets from Section 5.1 are used in this study. The structured grid shown in Figure 5.3 was used. As before simulations were only carried out an angle of attack of 40°.

5.2.2 Results

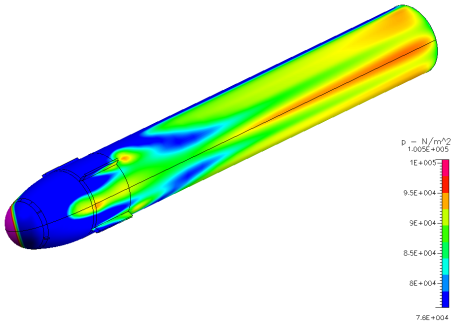
Figure 5.11 shows the surface pressure distributions on the missile bodies with the different strakelet models. The missile body with the geometric perturbation, from Section 4.1, is also included for comparison between the different set of results.



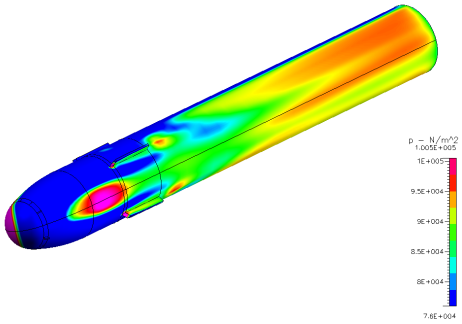
(a) Body of revolution with a geometric perturbation only



(b) Missile body with the model D strakelets



(c) Missile body with the model B strakelets



(d) Missile body with the model E strakelets

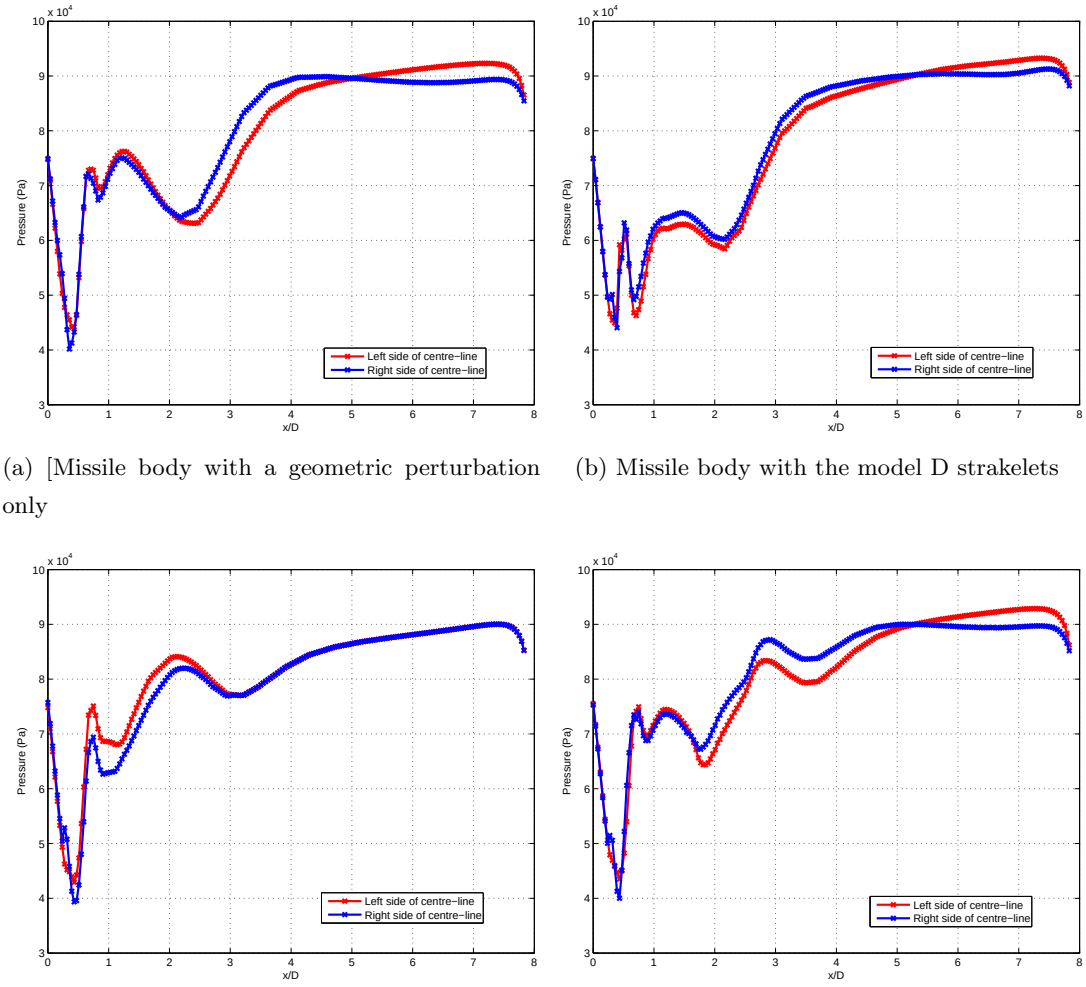
Figure 5.11: Surface pressure distributions on the different strakelet models at different axial locations at 40° angle of attack

Figures 5.11b and 5.11d show that moving the axial location of the strakelets does not eliminate the asymmetry in the flowfield. In Figures 5.11c and 5.11d small

regions of high surface pressure are visible at the trailing edge of the the model D strakelets. These high surface pressure regions are not visible in Figure 5.11b. This indicates that the vortices, that formed as a result of flow interaction with the model D strakelets are still attached to the missile body at the strakelets' trailing edge. The high surface pressure regions in Figures 5.11c and 5.11d indicate that the vortices separate shortly after the trailing edges of the model B and E strakelets.

Due to the different axial locations of the strakelets' leading edges, the axial location at which the the vortices separate from the missile body differ.

Figure 5.12 shows the surface pressure distribution a distance of $0.06D$ on either side of the body center line for the different models.



(a) [Missile body with a geometric perturbation only

(b) Missile body with the model D strakelets

(c) Missile body with the model B strakelets

(d) Missile body with the model E strakelets

Figure 5.12: The surface pressure distribution along the length of the missile body with the different strakelet models at different axial locations

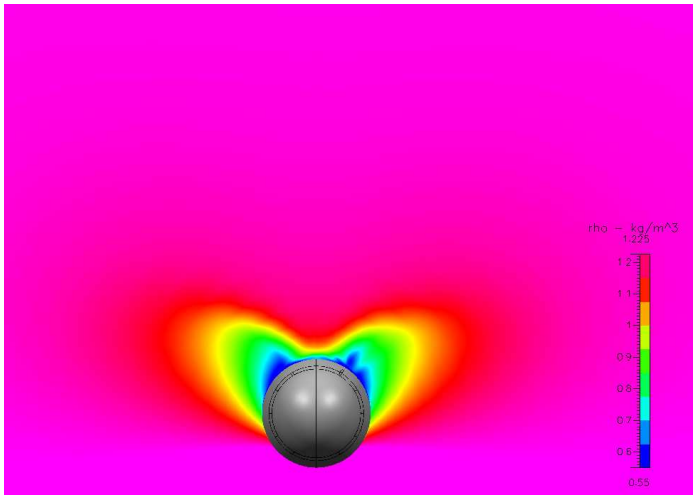
Figure 5.12b shows the surface pressure distribution on the body with the model

D strakelets. The leading edge of the model D strakelets is located $0.5D$ from the nose tip. There is a small difference in surface pressures across both halves of the body, indicating that the flow is asymmetric when it interacts with the model D strakelets. The trailing edge of the the model D strakelets is located $1.3D$ from the nose tip. At this axial location there is still a difference in surface pressures across both halves of the body. The surface pressure differences at the rear of the body, between $6D$ and $8D$ on the missile body is smaller than the differences in surface pressures in Figure 5.12a at the corresponding axial location, indicating that the model D strakelets were able to reduce vortex asymmetry.

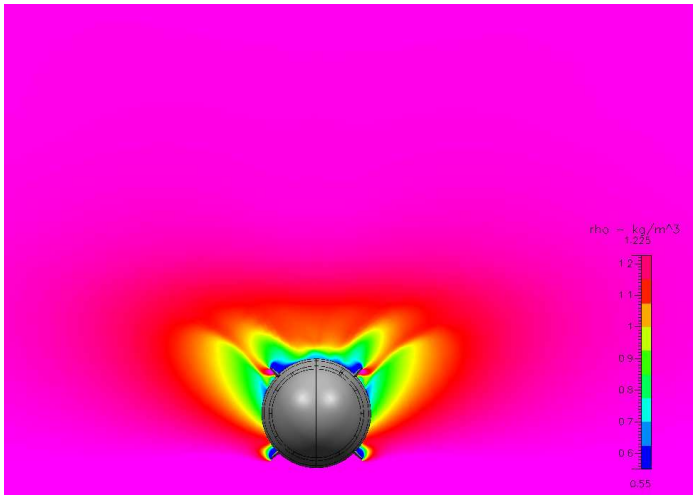
The difference in surface pressures at the leading edge of the the model B strakelets is larger than that at the leading edge of the the model D strakelets, indicating that the flow had a higher degree of asymmetry when it interacted with the model B strakelets due to the leading edge of the model B strakelets being $0.75D$ behind the geometric perturbation. Figure 5.12c is the same as Figure 5.5*c* in Section 5.1.

In Figure 5.12d the difference in surface pressures across both halves of the body surface at $1.3D$ is larger than the surface pressure differences on the bodies with the model D and B strakelets in Figures 5.12b and Figure 5.12c respectively. This indicates that the flow had a greater degree of asymmetry before it interacted with the model E strakelets. The flow remains asymmetric along the length of the strakelets and along the length of the body indicating that the model E strakelets were not able to force the flowfield to become symmetric.

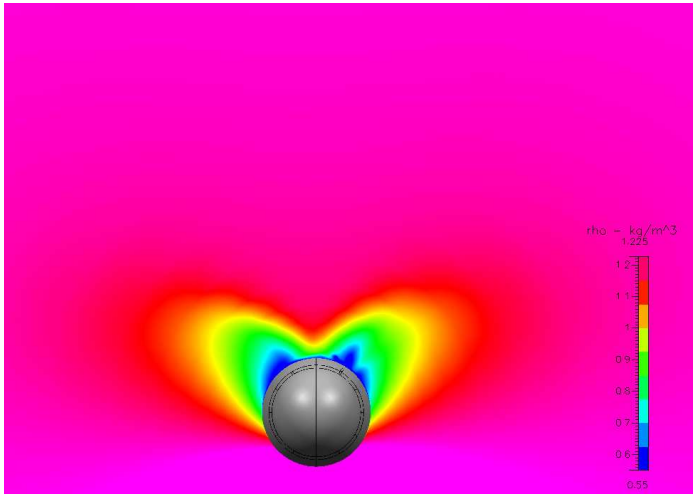
Density contour plots at different axial locations along the body are shown in Figures 5.14 to 5.18 to show flow development at different cross-sections along the body length.



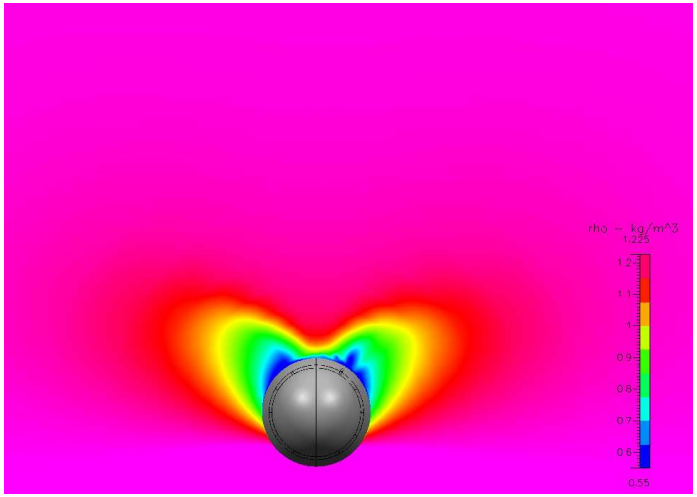
(a) Missile body with a geometric perturbation only



(b) Missile body with the model D strakelets



(c) Missile body with the model B strakelets

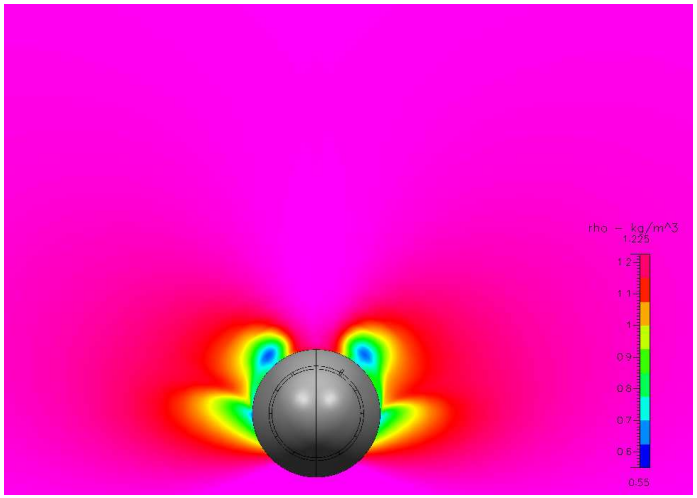


(d) Missile body with the model E strakelets

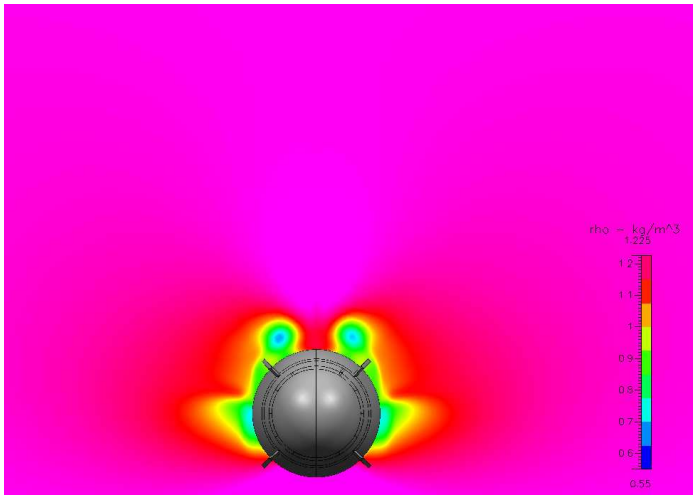
Figure 5.13: Flowfield on the missile bodies with different strakelet models at $x = 0.55D$ at an angle of attack of 40°

The flowfields on the missile bodies with models B and E in Figures 5.13c and 5.13d respectively, are the same as that in Figure 5.13a. The leading edge of the model B strakelets is located at $1D$ away from the nose tip and that of the model E strakelets is located $1.3D$ away from the nose tip.

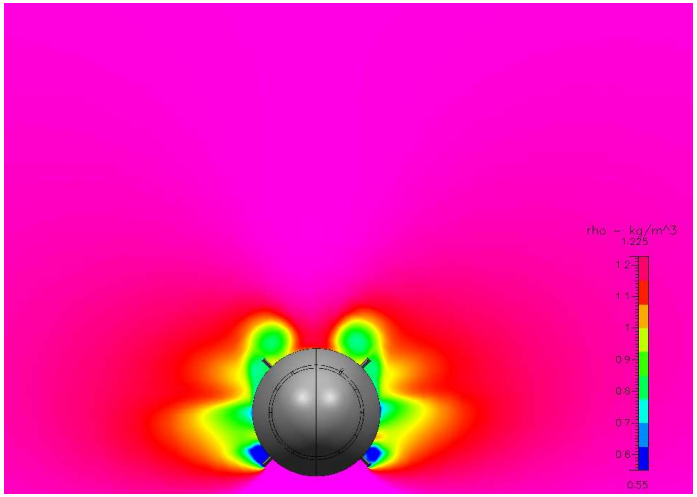
Figure 5.13b shows flow interaction with the the model D strakelets. The flow is asymmetric when it interacts with the model D strakelets as indicated by the difference in surface pressures in Figure 5.12d at $0.55D$.



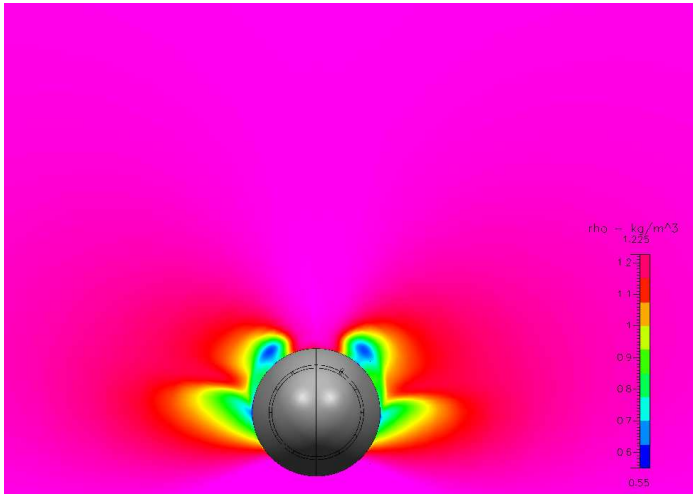
(a) Missile body with a geometric perturbation only



(b) Missile body with the model D strakelets



(c) Missile body with the model B strakelets



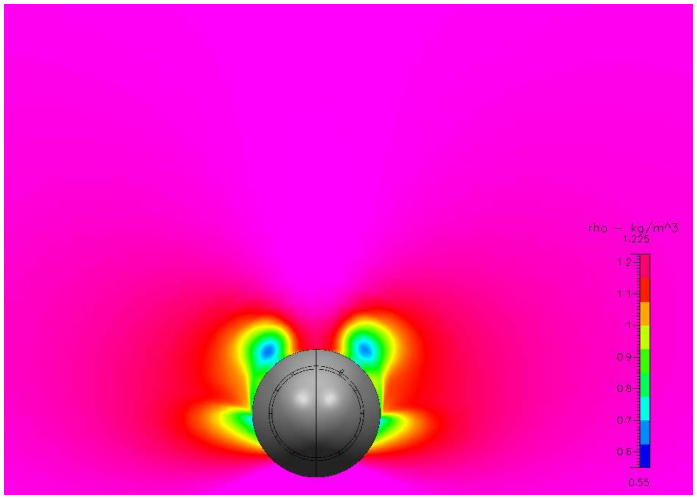
(d) Missile body with the model E strakelets

Figure 5.14: Flowfield on the missile bodies with different strakelet models at $x = 1.2D$ at an angle of attack of 40°

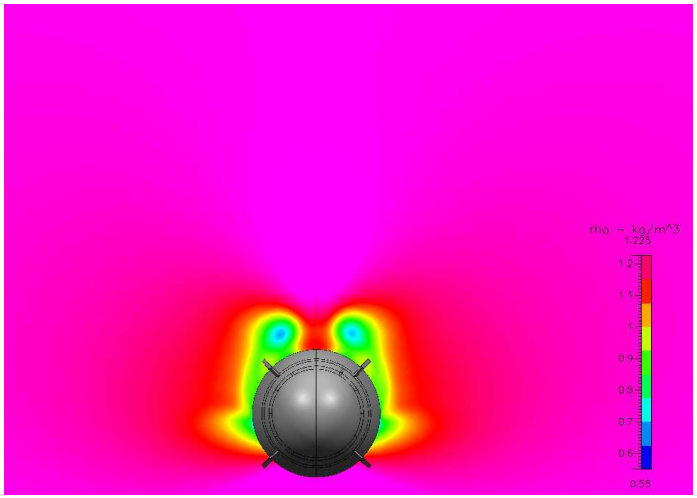
In Figure 5.14b the right and left vortices are of similar sizes and are still attached to the missile body. The surface pressure on the right of the missile body centre-line in Figure 5.12b, at $1.2D$ is slightly higher than that on the left of the missile body centre-line. This indicates that the right vortex is in slightly less contact with the missile body surface than the left vortex and will thus separate before the left vortex. Since the geometric perturbation forced the right vortex to separate first, as shown in Section 4.2, the model D strakelets have not changed the vortex pattern in the flowfield. Flow from the bottom strakelets move towards the leeward side of the missile body.

In Figure 5.14c the flowfield $0.1D$ after the leading edge is shown. The left vortex is slightly smaller than the right vortex. Thus the left vortex has less contact with the missile body surface, resulting in the higher surface pressure on the left of the missile body centre-line, as shown in Figure 5.12c at $x = 1.2D$. The geometric perturbation introduces an asymmetry on the right of the body centre-line, as shown in Section 4.2 in Figure 4.20. Since the left vortex has less contact with the body, it will separate before the right vortex. Thus the model B strakelets changed the vortex pattern introduced by the geometric perturbation.

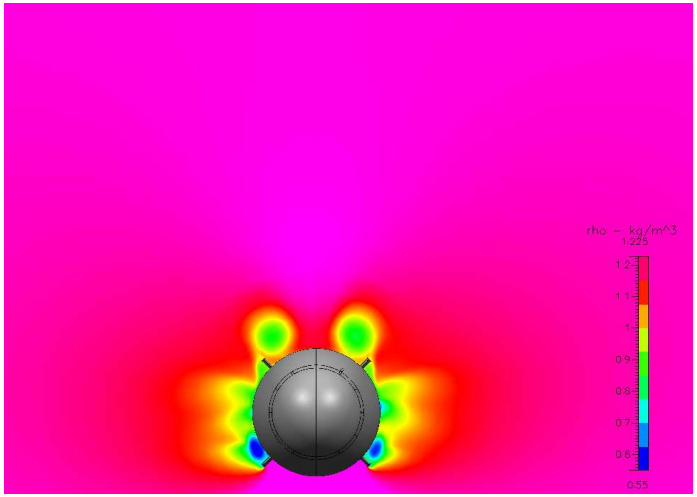
The flow in Figure 5.14d resembles that in Figure 5.14a since the leading edges of the model E strakelets are located $1.3D$ from the nose tip. Both body vortices are still attached to the body. The surface pressure differences in Figure 5.12d shows that the flow is asymmetric before it interacts with the leading edge of the the model E strakelets.



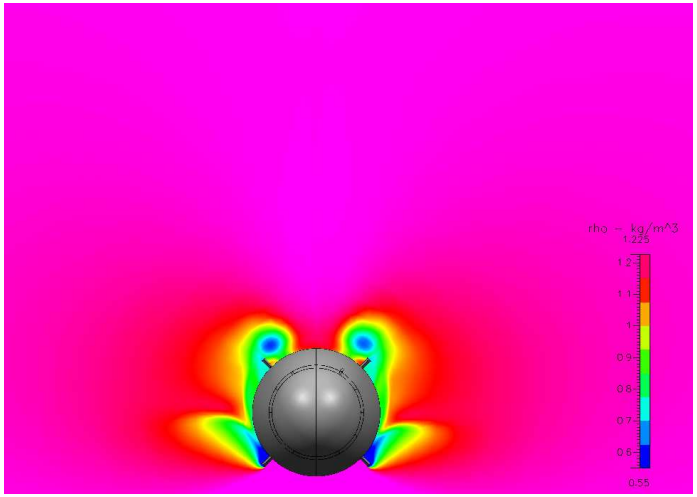
(a) Missile body with a geometric perturbation only



(b) Missile body with the model D strakelets



(c) Missile body with the model B strakelets



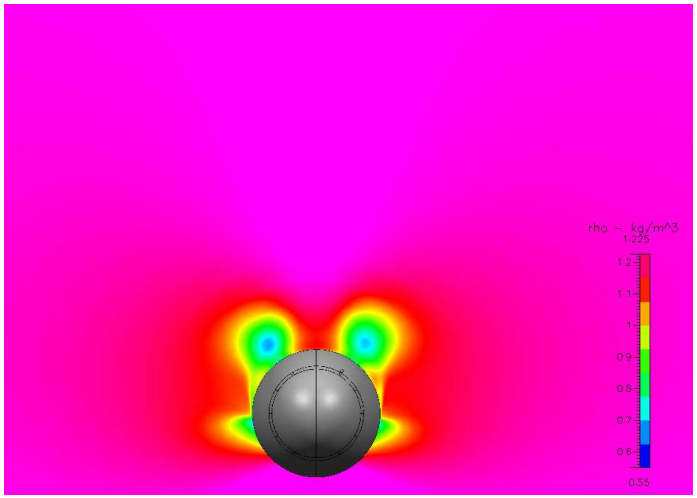
(d) Missile body with the model E strakelets

Figure 5.15: Flowfield on the missile bodies with different strakelet models at $x = 1.5D$ at an angle of attack of 40°

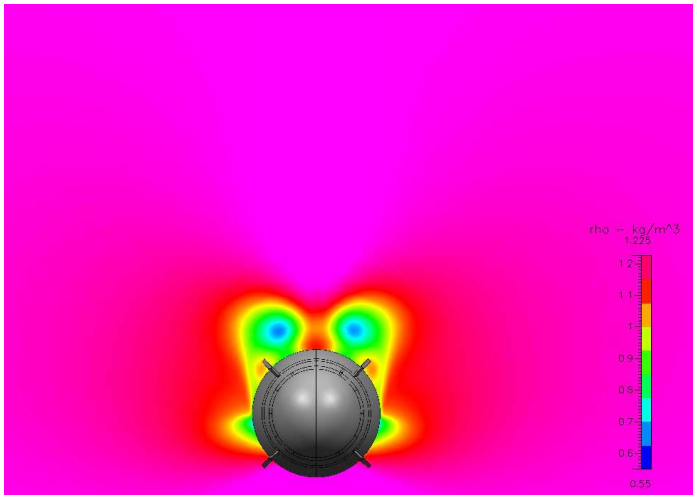
Figure 5.15b shows the flowfield behind the the model D strakelets. Flow from the bottom strakelets moves around the missile body surface and separates on the leeward side of the body. The separated flow feeds into the two attached vortices. Flow separation has occurred on both sides of the missile body at the same axial location, indicating the two attached vortices will be strengthened at the same axial position on the missile body. The asymmetry, introduced by the geometric perturbation, is not evident in Figure 5.15b, however in Figure 5.12b, at $x = 1.5D$ the surface pressure on the right of the body centre-line is higher than that on the left. This asymmetry will develop along the length of the body resulting in the formation of asymmetric vortices. Thus the vortices, produced by the model D strakelets were not able to produce strong vortices to absorb the asymmetry introduced by the geometric perturbation on the missile nose.

In Figure 5.15c the left vortex has separated from the missile body before the right vortex, resulting in a higher surface pressure on the left of the body centre-line in Figure 5.12c at the corresponding axial location.

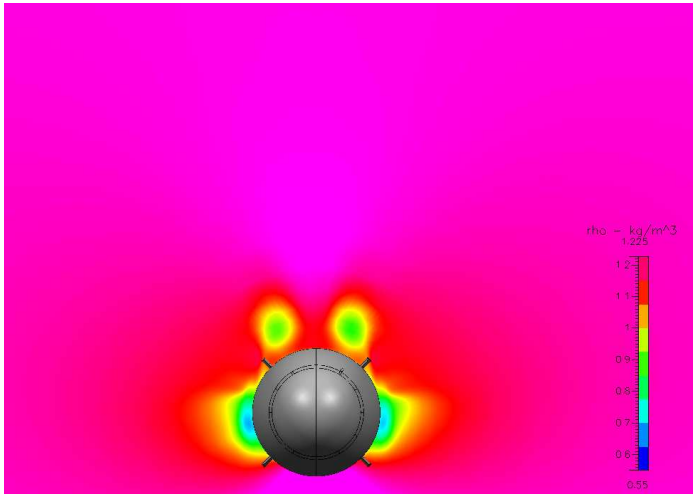
In Figure 5.15d two well-defined body vortices interact with the model E strakelets. Since the vortices are well formed upon interaction with the strakelets, the vortices are forced to separate. The vortex on the right is further away from the body surface than the left vortex in Figure 5.15d. This is further confirmed by the higher surface pressure on the right of the body centre-line in Figure 5.12d at $x = 1.5D$ which indicates that the right vortex is slightly higher than the left vortex from the missile body surface. The left vortex pattern, introduced by the geometric perturbation, has not changed, since the right vortex will separate first from the body surface.



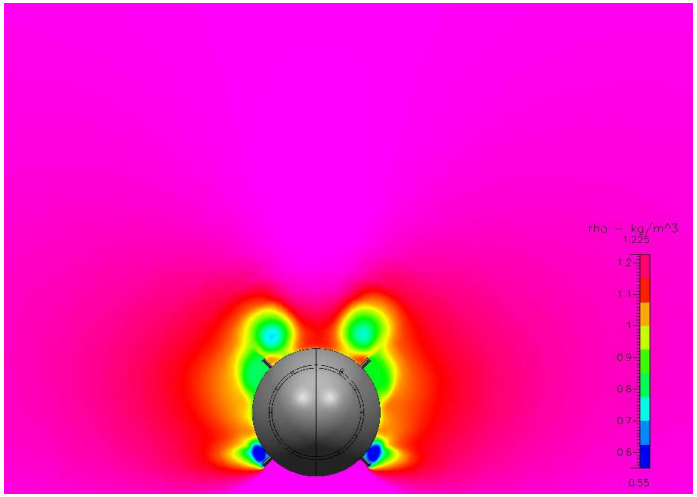
(a) Missile body with a geometric perturbation only



(b) Missile body with the model D strakelets



(c) Missile body with the model B strakelets



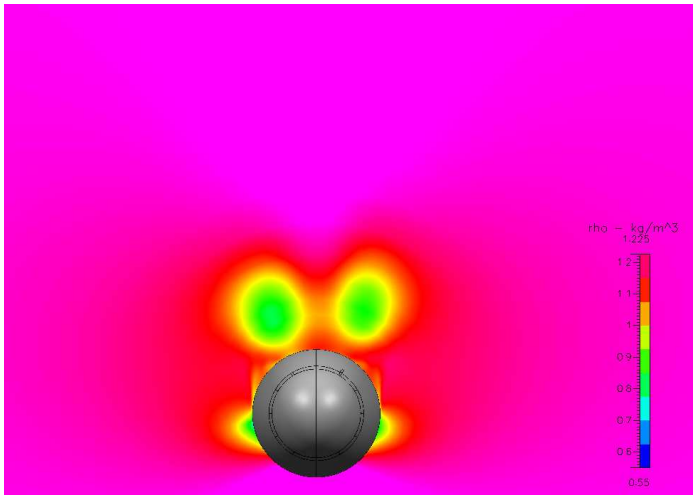
(d) Missile body with the model E strakelets

Figure 5.16: Flowfield on the missile bodies with different strakelet models at $x = 2.3D$ at an angle of attack of 40°

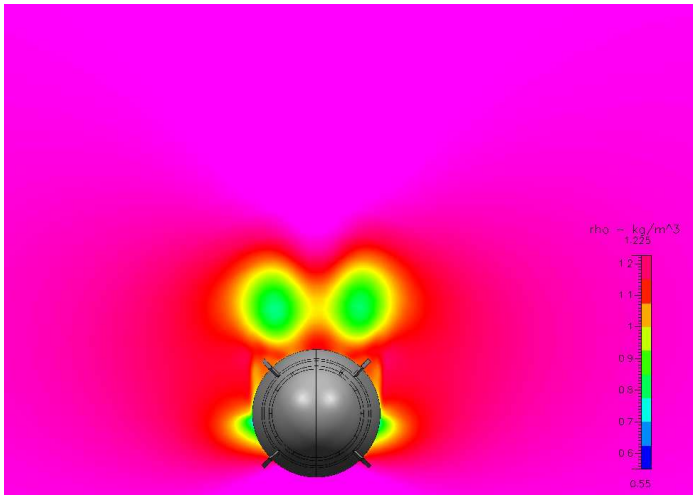
Figure 5.16b shows the formation of two almost symmetric vortices. Figure 5.12b shows that the surface pressure on the right is slightly higher than that on the left at $2.3D$ from the nose tip, indicating that the right vortex has less contact with the missile body surface than the right vortex. Since the difference in surface pressures on both halves of the body, in Figure 5.12b, is small it is difficult to see the asymmetry in Figure 5.16b.

Figure 5.16c shows the flow behind the model B strakelets. The left vortex is further away from the missile body surface than the right vortex. This results in the higher surface pressure on the left in Figure 5.12c at $2.3D$. Flow from the bottom strakelets move towards the leeward side of the body.

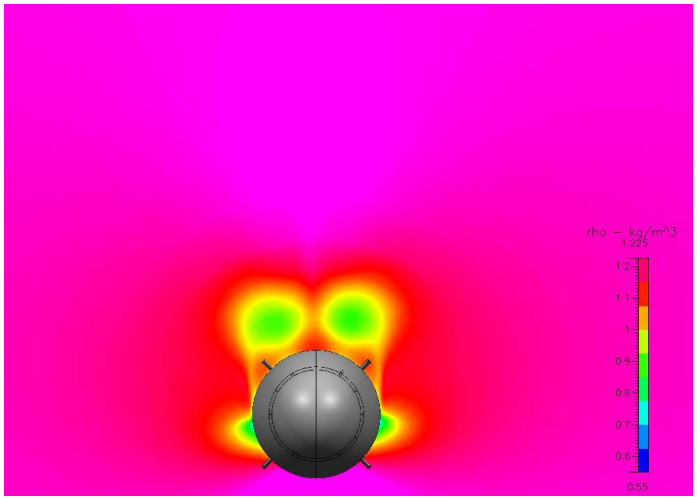
The right vortex in Figure 5.16d has less contact with the missile body than the left vortex. Thus the surface pressure on the right of the body centre-line is higher than that on the left in Figure 5.12d at the corresponding axial location. Flow is still attached to the bottom strakelets.



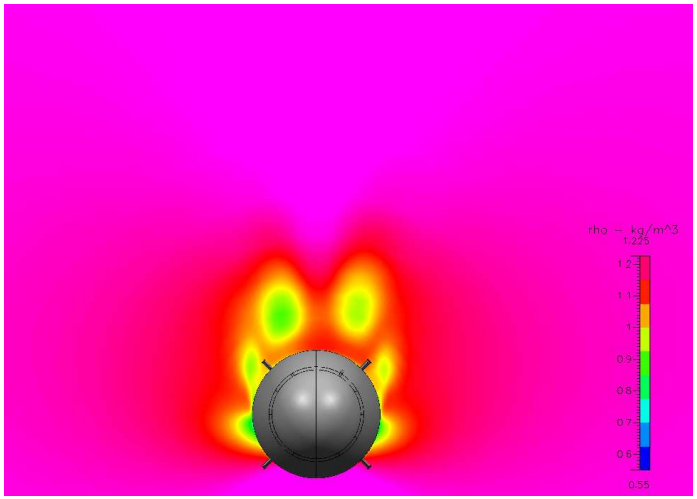
(a) Missile body with a geometric perturbation only



(b) Missile body with the model D strakelets



(c) Missile body with the model B strakelets



(d) Missile body with the model E strakelets

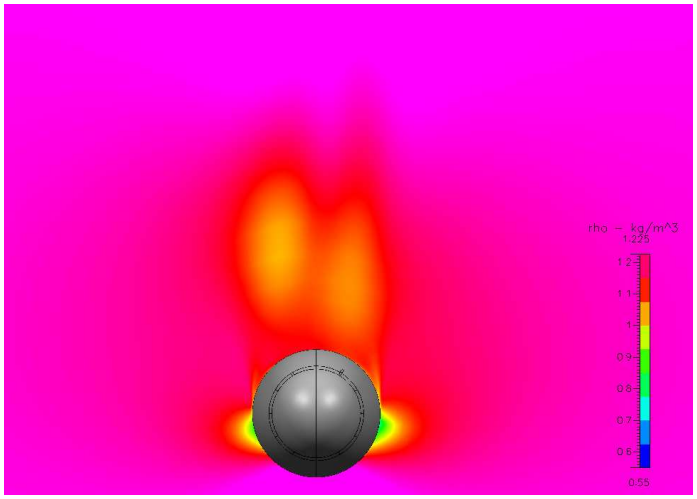
Figure 5.17: Flowfield on the missile bodies with different strakelet models at $x = 3.4D$ at an angle of attack of 40°

In Figure 5.17b the right vortex is slightly smaller than the left vortex, indicating that it is further away from the body surface than the left vortex. This is confirmed by the higher surface pressure on the right of the missile body centre-line in figure 5.12b at $5.5D$. The two vortices will continue to develop asymmetrically along the length of the missile body resulting in an asymmetric flowfield, as indicated by the surface pressure distribution in Figure 5.11b and 5.12b.

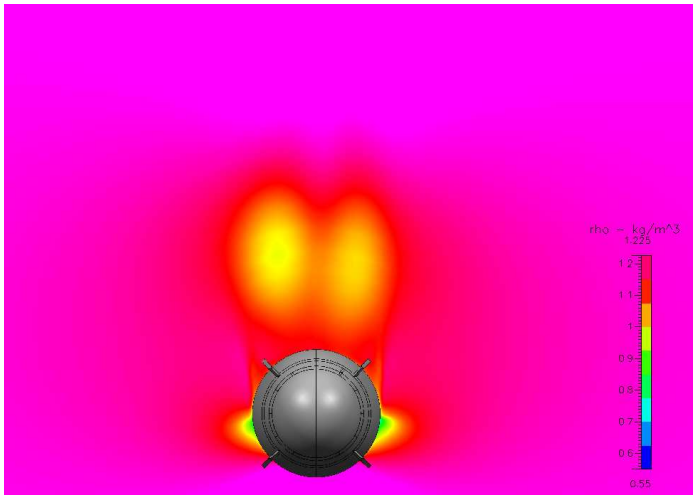
Figure 5.8c in Section 5.1 shows that flow from around the body separates at the same axial position of $2.8D$ on the missile body. At this axial position both vortices are at the same height above the body surface, as indicated by the equal surface pressure on the missile body at $2.8D$ in Figure 5.12c. Thus the separated vortices are strengthened at the same axial position on the body resulting in the formation of two symmetric vortices, shown in Figure 5.17c. The surface pressures on either side of the missile body centre-line are equal at this axial location in Figure 5.12c.

Figure 5.17d shows that flow from around the body separates at the same axial position along the missile body length. However, the asymmetry introduced by the geometric perturbation has influenced flow separation since the separating flow on the left is stronger than that on the right. Thus the height of the model E strakelets was not large enough to strengthen the flow such that the separating flow would not be influenced by the asymmetry present in the flowfield. Since the left vortex is closer to the body surface, as indicated by the lower surface pressure on the left in Figure 5.12d, the left vortex will be strengthened before the right vortex. This results in the vortices developing asymmetrically along the remainder of the missile body length.

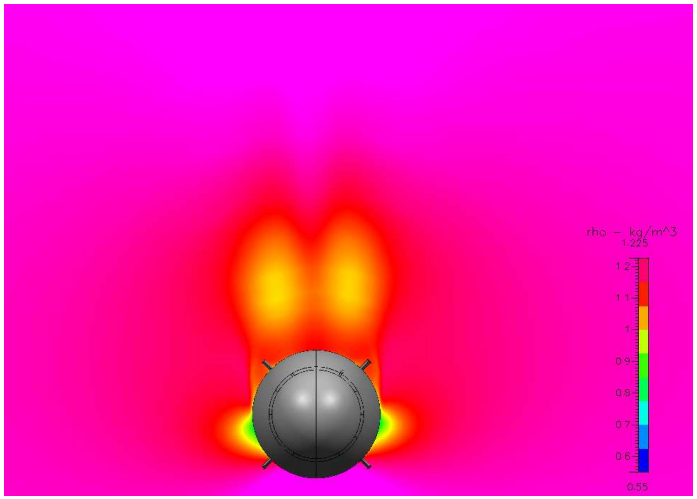
Figure 5.18 shows the flowfield at the rear of the missile body.



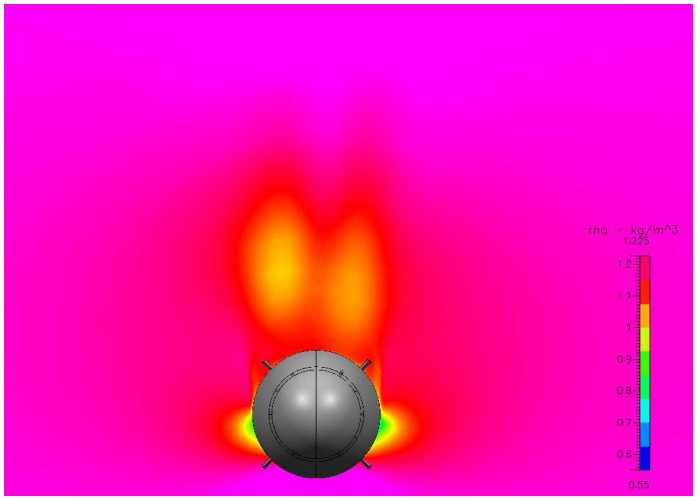
(a) Missile body with a geometric perturbation only



(b) Missile body with the model D strakelets



(c) Missile body with the model B strakelets



(d) Missile body with the model E strakelets

Figure 5.18: Flowfield on the missile bodies with different strakelet models at $x = 6.9D$ at an angle of attack of 40°

In Figure 5.18b the difference in height between the two vortices is small when compared to the difference in height between the two vortices in Figure 5.18a. This indicates that the degree of asymmetry present in the flowfield in Figure 5.18b is less than that in Figure 5.18a. Thus moving the strakelets closer to the nose allows for a reduction in vortex asymmetry.

The resultant flowfield in Figure 5.18c is symmetric. Both vortices are similar in size and are the same height above the body surface.

The asymmetric flowfield in Figure 5.18d is very similar to that in Figure 5.18a. The surface pressure difference across both halves of the body in Figure 5.12d at $6.9D$ is very similar to the surface pressure difference in Figure 5.18d at the corresponding axial location. Thus moving the strakelets further back does not result in a symmetric flowfield.

5.2.3 Discussion

Since the leading edge of the three strakelet models are located at different axial locations on the missile body surface, the flow asymmetry on the body is at different stages in its development along the length of the body, when it interacts with the each of the three models.

Missile body with the model D strakelets

A distance $0.15D$ after the flow has been triggered to become asymmetric by the geometric perturbation that was placed $0.25D$ from the nose tip, the flow interacts with the leading edge of the model D strakelets. The surface pressure on the right side of the body centre-line is higher than the surface pressure on the right in Figure 5.12d at $0.5D$, indicating that the flow was asymmetric when it interacted with the strakelets. Figure 5.12b shows that the difference in surface pressure across both halves of the missile body, at the leading edge of the model E strakelets, was less than the surface pressure difference at the leading edge of the model B strakelets, at $x = 1D$ in Figure 5.12c. The flow remains asymmetric along the length of the strakelets, as indicated by the surface pressure differences in Figure 5.12b from $x = 0.5D$ to $x = 1.3D$. At the trailing edge of the strakelets the vortices are still attached to the body, as shown by the low pressure regions in Figure 5.11b. Figure 5.12b shows that the surface pressure on the right is higher than that on the left, thus the right vortex is in less contact with the missile body than the left

vortex. Behind the trailing edge of the strakelets, flow from the bottom strakelets moves, along the missile body surface and separates at the same axial position on the leeward side of the body at $x = 1.5D$, as shown in Figure 5.15d. The separated flow feeds the two attached vortices on the leeward side of the body. The flow on both sides of the body separated at the same axial position indicating that the height of the model D strakelets was sufficient to strengthen the flow such that it was unaffected by the asymmetry present in the flowfield. At the corresponding axial location in Figure 5.12b, the higher surface pressure on the right of the body centre-line implies that the right vortex is in less contact with the body. The low surface pressure regions on the missile body surface in Figure 5.11b indicates that the right vortex separates shortly before the left vortex. Therefore the asymmetry, introduced by the geometric perturbation on the nose is still present as shown in Figure 5.18b. The vortices produced by the top strakelets of the model D were not able to eliminate the asymmetry present in the flowfield.

Missile body with the model E strakelets

The leading edge of the model E strakelets was positioned $1.3D$ from the nose tip. At this axial location the surface pressure on the right of the missile body centre-line is less than the surface pressure on the left of the body centre-line, as seen in Figure 5.12d. Thus the flow is asymmetric when it interacts with the strakelets. For the length of the strakelets, from $x = 1.3D$ to $x = 2.1D$, the surface pressure on the right of the body centre-line remains higher than the surface pressure on the left, indicating that at the trailing edge of the model E strakelets the right vortex was slightly higher than the left vortex from the missile body. In Figure 5.15d the high density region under the vortex illustrates that the right vortex is forced further away from the missile body. In Figure 5.16d two well defined vortices form. The right vortex is slightly larger than the left vortex and is slightly higher than the left vortex. In Figure 5.17d the flow from the bottom strakelets separates from both sides of the missile body at $3.4D$ from the nose tip, illustrating that the model E strakelets were able to strengthen the flow so that the asymmetry, triggered by the geometric perturbation, did not influence the flow as it did for the model A strakelets, where flow separation occurred at two different axial locations (Section 5.1). At $3.4D$, in Figure 5.12d the surface pressure on the right is higher than on the left, thus the right vortex is further away from the missile body than the left vortex. The left vortex would be strengthened before the right vortex and the two vortices would develop asymmetrically along the length of the body, resulting in the flowfield in Figure 5.18d.

5.3 Effect of Strakelets on a Steady Asymmetric Flowfield

The model A strakelets had a height of $0.06D$. The model A strakelets on the leeward side of the body were not able to produce strong enough vortices to eliminate the asymmetry in the flowfield. The asymmetry, introduced by the geometric perturbation on the nose influenced the flow on the missile body surface by forcing the right vortex to separate before the left vortex. At the trailing edge of the model A strakelets the right vortex is higher than the left vortex, and since the geometric perturbation introduced an asymmetry on the right of the body centre-line (Section 4.2), the right vortex is pushed further away from the missile body. The flow from the bottom strakelets was also not strong enough to absorb the effect of the asymmetry in the flowfield, thus forcing flow separation at two different axial locations on the missile body. Since the flow on the left separated before the flow on the right, the left vortex was strengthened before the right vortex. This resulted in the two asymmetric vortices developing asymmetrically along the rest of missile body.

The model C strakelets were large enough to produce strong symmetric vortices which were not influenced by the asymmetry introduced by the geometric perturbation on the nose. At the trailing edge of the model C strakelets two symmetric vortices had formed, however, the asymmetry introduced by the perturbation was still present in the flowfield. This resulted in the right vortex being pushed further away from the missile body. The flow from the bottom strakelets separated at the same axial location on the body. However, since the left vortex was closer to the missile body than the right vortex it was strengthened by the left separated flow before the right vortex was strengthened by the flow separating on the right side of the missile body. Since the vortices were strengthened asymmetrically, the vortices developed asymmetrically along the rest of the body length resulting in an asymmetric flowfield. Even though the flow separated from around the body at the same axial position since the vortices were at different heights above the missile body surface one vortex was strengthened before the other. Thus the resultant flowfield was made less asymmetric.

The model D strakelets were place $0.25D$ behind the geometric perturbation, thus the asymmetry in the flowfield had not been allowed to develop for a distance on the missile body before it interacted with the leading edge of the model D strakelets. The flow remained attached to the missile body for the length of the the model D strakelets. The asymmetry introduced by the geometric perturbation was still present in the flow at the trailing edge of the model D strakelets even though the

flow was still attached to the body. Flow from the bottom strakelets separated at the same axial location on the body and strengthened the two attached leeward vortices symmetrically. However, since the asymmetry introduced by the geometric perturbation was still present the vortices developed asymmetrically along the missile body. The presence of the model strakelets on the missile body did reduce the vortex asymmetry, since the flow interacted with the strakelets shortly after being forced into a steady asymmetric state. The height of the model D strakelets was not sufficient to produce strong vortices to eliminate the asymmetry.

The model E strakelets were placed $0.15D$ behind the perturbation. Thus when the flow interacted with the model E strakelets two well defined body vortices had already formed, forcing vortex separation close to the leading edge of the strakelets. The asymmetry, introduced by the geometric perturbation was allowed to develop for a distance of $1.3D$ along the body before it interacted with the model E strakelets. At the trailing edge of the model E strakelets the right vortex was further away from the body than the left vortex. The flow from the bottom strakelets separated at the same axial location on the missile body with differing strengths. Since the asymmetry was allowed to develop for a considerable distance along the length of the missile body, it influenced the strength of the flow separating around the missile body. Since the left vortex was closer to the body than the right vortex and the separated flow on the left was stronger than that on the right, the left vortex was strengthened before the right vortex. This resulted in the vortices developing asymmetrically along the length of the body.

At the trailing edge of the model B strakelets the left vortex was further away from the missile body than the right vortex. Thus the model B strakelets changed the asymmetry from the right of the missile body to the left, forcing the left vortex to separate before the right one. Since the geometric perturbation introduced the asymmetry on the right, as the two vortices developed along the length of the body, the right vortex that was closer to the body was pushed further away from the body, such that the two vortices were approximately the same distance from the missile body when flow separated from the sides of the missile body. The bottom strakelets had strengthened the flow such that the flow was not influenced by the asymmetry in the flowfield and thus separated at the same axial location on the body surface. Since the two separated vortices were at the same height above the body when the flow separation took place, both vortices were strengthened at the same axial position, resulting in the formation of two symmetric vortices. The two vortices developed symmetrically along the rest of the body length and at the base of the missile body, both vortices were at the same height above the missile body.

5.4 Conclusion

The strakelets with a span of $0.06D$, at an axial location of $1.1D$ did not produce strong enough vortices to eliminate the flowfield asymmetry introduced by the geometric perturbation.

The strakelets with a span of $0.13D$, at an axial location of $1.1D$ did result in a reduction in flow asymmetry, but were unable to eliminate the asymmetry.

The strakelets at an axial location of $0.5D$, with a span of $0.09D$ were not large enough to force the formation of strong vortices to eliminate flow asymmetry but the strakelets were able to reduce flow asymmetry.

The strakelets at an axial location of $1.8D$, with a span of $0.09D$ did not reduce or eliminate flow asymmetry. Placing the strakelets too far back allows flow asymmetry to develop, thus making it difficult to eliminate the asymmetry.

The strakelets with a span of $0.09D$ at an axial location of $1.1D$ was able to eliminate the asymmetry present in the flowfield. The strakelets resulted in the formation of vortices which were strong enough to force symmetry.

Placing the leading edge of the strakelets where the pressure difference is the greatest, yielded the best results. If the leading edge of the strakelets are placed close to the axial position at which the surface pressure distribution is the greatest, the asymmetry in the flowfield is not allowed to develop along the length of the body. The strakelets would produce vortices that would possibly be stronger than the asymmetry introduced by the geometric perturbation on the nose. However, the span of the strakelets also plays a role in determining if the resultant flowfield is symmetric.

Increasing the span of the strakelets does result in the strakelets producing sufficiently strong vortices to absorb the effect of the asymmetry. However, if the strakelet span is increased by too much, and if the length of the strakelets is too small the asymmetry could develop along the length of the body behind the strakelets trailing edge.

Changing the height and the leading edge of the strakelets, and thus indirectly changing the strakelet's trailing edge position, has shown that the steady asymmetric flowfield at high angles of attack is very sensitive to the three parameters. When the strakelet height was increased to $0.09D$, while the leading edge position was

fixed at $1.1D$ and the chord length was fixed at $0.7D$ the steady asymmetry in the flowfield was eliminated, showing that the three parameters were in the right combination. However, once the strakelet height was increased further to $0.13D$ the flowfield remained asymmetric, but the steady asymmetry had been reduced. The increase in strakelet height resulted in a change in combination of the three variables and thus the combined effects of the variables were not able to eliminate the flowfield asymmetry. This shows that if the strakelet height changes the other two parameters must change as well to obtain a symmetric flowfield.

The sensitivity of changing the strakelet parameters was once again illustrated when the leading edge position of the strakelets were changed while keeping the strakelet height and strakelet chord length constant. Once the combinations of the three parameters were changed the flowfield became asymmetric. The steady asymmetry of the flowfield was increased when the strakelets were moved further away from the geometric perturbation and reduced when the strakelets were moved closer to the geometric perturbation but was not eliminated since the other two parameters were not in the right proportion.

The effect of changing the strakelet chord length was not investigated in this study but it is recommended that its effect must be investigated. However, by the findings in this study that the three parameters need to be in the right proportion to obtain a symmetric flowfield, it is suggested that when investigating the effect of the strakelet chord length, the strakelet height and the strakelet chord length must be varied, as per run 8 in Table 5.1. Each of the three strakelet geometry parameters contributes in forcing symmetry on a steady asymmetric flowfield.

6 Conclusions and Recommendations

6.1 Conclusions

Experimental tests conducted by Gobey (2004) on a body-strake configuration (a body of revolution with a very low aspect ratio wings), revealed that there was a dramatic difference in normal force and pitching moment coefficients generated by the missile strakes at different roll orientations. When the missile strakes were orientated in the '×' configuration the normal force coefficients generated by the missile strakes were very small when compared to that generated by the strakes in the '+' orientation. The low normal force coefficients indicated that the missile strakes were not forcing the flow to separate from the body when they were in the '×' orientation. Thus in order to force the flow to separate sufficiently far from the body, and thus improving the aerodynamics of the body-strake configuration when the missile strakes are in '×' orientation, the missile strake span was increased from $0.06D$ to $0.13D$.

When the shorter strakes were orientated in the '×' flow around the body reattached itself to the body once it had interacted with the bottom strakes. This resulted in very low values of normal force coefficients, and thus pitching moment coefficients at low angles of attack. The higher normal force coefficients generated by the strakes when they were in the '+' orientation was due to the flow not reattaching itself to the body.

The higher strakes (strake span = $0.13D$) increased the effective diameter of the missile body and thus flow around the body did not reattach to the body. This resulted in the formation of stronger vortices and thus an increase in the normal force generated by the strakes at the low angles of attack. From the work of Chapter 2 it can be concluded that an increase in the strake span results in greater flow separation around the body. The increase in strake span resulted in an increase in normal force coefficient ranging from 11.28% at 30° to 42% at 10°. The increase in normal force

resulted in a corresponding increase in pitching moment coefficient ranging from 43% at 30° to 52% at 20° angle of attack. Thus increasing the strake span resulted in an increase in the normal force coefficient generated by the strakes due to the prevention of flow reattachment.

Degani and Schiff (1991) found that to create a steady asymmetric flowfield in CFD it was necessary to introduce a time-invariant, space-fixed perturbation near the apex of an ogive cylinder. Degani and Schiff (1991) suggested the use of a geometric bump on the nose of the body of revolution or a small jet flowing normal to the body of revolution. Levy et al. (1990) found that the essential steady asymmetric multi-vortex structure could be qualitatively captured by the use of a simple simulated disturbance. The methods suggested by Degani and Schiff (1991) were used as guidelines since they studied the steady asymmetric flowfield on a pointed slender body and a blunt ogive body of revolution was used in this study. A geometric perturbation, as suggested by Degani and Schiff (1991), was placed on the missile nose to create steady asymmetric vortices on the missile body. An iterative process using three different sized perturbations was carried out to determine the size of the perturbation required to create an asymmetric flowfield that would be representative of that on a blunt ogive body. The effect of the axial and circumferential position of the chosen geometric perturbation on steady asymmetric vortices was also investigated.

All three perturbations forced a steady asymmetric flowfield on the missile body. The primary and secondary vortices were adequately captured. It was found that the degree of asymmetry introduced into the flowfield was dependent on the size of the perturbation used, with the largest perturbation resulting in the highest degree of flow asymmetry, as defined by Levy et al. (1990). The smallest perturbation, perturbation I, with a height of $0.03D$, a length of $0.06D$ and a width of $0.02D$ resulted in an asymmetric flowfield most representative of that on a blunt ogive body. This perturbation was used in further studies.

It was also found that when the geometric perturbation was removed from the missile body once a steady asymmetric flowfield had been obtained, the flowfield returned to its steady symmetric state. This was similar to the findings of Degani and Schiff (1991) and confirmed that the asymmetry introduced by the geometric perturbation on the missile nose was amplified along the length of the body by a convective instability. When the geometric perturbation was placed on a full length missile body, the multi-vortex structure of steady asymmetric vortices was also captured.

Placing the geometric perturbation at the tip of the missile body, as suggested by

Degani (1992) did not result in an asymmetric flowfield. It was found that by placing the geometric perturbation further away from the missile nose tip, steady asymmetric vortices formed, with the degree of asymmetry increasing with an increased distance from the missile nose tip. However, placing the geometric perturbation too far down the length of the missile body could result in the formation of asymmetric vortices away from the body, which is not realistic. By placing the geometric perturbations at two different axial positions at the same circumferential position resulted in the two different states of steady asymmetric vortices. The perturbation used in this study introduced the right vortex pattern, as defined by Xuei et al. (2000).

Changing the circumferential position of the perturbation did not have any visible effect on the state and strength of the formed asymmetric flowfield.

In order to eliminate the side forces that develop on a body of revolution due to the formation of steady asymmetric vortices, four forebody strakelets were placed, in the '$\times$' orientation, on the missile nose, behind the geometric perturbation. The objective of the strakelets was to force the formation of symmetric vortices thus eliminating side force development on the missile body.

Strakelets with a span of $0.09D$, placed $1D$ from the missile nose tip, forced the formation of symmetric vortices. This is due to the leading edge of the strakelets being placed close to the point at which the largest difference in surface pressures existed. The strakelets were also large enough to produce strong vortices to eliminate the asymmetry introduced by the geometric perturbation by changing the vortex pattern introduced by the strakelets.

Decreasing the span of the strakelets to $0.06D$ did not change the vortex pattern introduced by the geometric perturbation as the vortices produced by the shorter strakelets were not strong enough to eliminate the asymmetry in the flowfield. Increasing the span of the strakelets to $0.13D$ did not have the desired effect of eliminating the asymmetry introduced by the geometric perturbation. For as long as the flow interacted with the strakelets the formed vortices were symmetric. However, the flow behind the strakelets trailing edge developed asymmetrically resulting in the formation of asymmetric vortices.

Placing the strakelets with a span of 0.09 closer to the nose tip reduced the asymmetry introduced by the geometric perturbation. This is due to the vortices, produced by the strakelets not being strong enough to absorb the effect of the geometric perturbation. Placing the strakelets leading edge further away from the nose tip did not

eliminate the asymmetry introduced by the geometric perturbation, as the asymmetry was allowed to develop in the flowfield. Placing the strakelets close to the point at which the difference in surface pressures is the largest has the best effect of reducing the asymmetry in the flowfield.

It was found that by placing the leading edge of the strakelets close to the axial position at which the largest surface pressure difference was experienced, resulted in the formation of symmetric vortices. The asymmetry, introduced by the geometric perturbation, was not allowed to develop along the length of the body since the vortices produced by the strakelets absorbed the effect of the asymmetry.

The span of the strakelets also played an important role in determining if the resultant flowfield was symmetric. Increasing the strakelet span does result in the strakelets forcing flow to separate sufficiently far from the body, thus resulting in the formation of strong vortices that absorb the effect of the asymmetry introduced by the geometric perturbation on the missile nose. However, if the strakelet's span is increased by too much and the length of the strakelets is too small, the asymmetry could develop in the flowfield behind the trailing edge of the strakelets.

This study showed that the steady asymmetric flowfield on a body at high angles of attack is very sensitive to the combination of both geometric strakelet parameters that were tested. An increase in the strakelet height from $0.06D$ to $0.09D$, while keeping the chord length constant at $0.8D$ and the leading edge position of the strakelet fixed at $1D$, resulted in a steady symmetric flowfield. By increasing the strakelet height to $0.09D$ the strakelet chord length, strakelet height and strakelet leading edge position were in the right proportion to one another and thus were effective in forcing a symmetric flowfield. However, once the strakelet height was increased further, or the leading edge position of the strakelet was moved, the three parameters were not in the right proportion to each other and the resultant flowfield remained asymmetric. This showed that small changes to strakelet parameters resulted in a steady asymmetric flowfield of a higher or lesser degree than when no strakelets were present on the body. Thus each of the three strakelet geometry parameters contributes in forcing symmetry on a steady asymmetric flowfield.

6.2 Recommendations

In creating the asymmetric flowfield in CFD, a hexahedral block was used. Studies should also be conducted to determine the effect of using a different shaped geometric perturbation.

The study conducted in this research has only focused on the effect of changing the span and axial location of the strakelets, when orientated in the '×'. Studies should also focus on changing the chord length and the width of the strakelets.

A similar study, with respect to changing the span, the axial position, the chord length and width of the strakelets should also be carried when the strakelets are in the '+' orientation.

A further study should also be carried to determine the effect of changing the strakelets geometry, possibly investigating the effect of a delta-shaped strakelet.

The Menter-SST $k - \omega$ turbulence model was used in this study. The efficiency of using the large eddy simulation (LES) turbulence model or the detached eddy simulation (DES) turbulence model should also be investigated.

REFERENCES

J.E. Bardina, P.G. Huang, and T.J. Coakley. *Turbulence Modelling Validation, Testing and Development. NASA Technical Memorandum*, 1997.

L.B. Barrentine. *An Introduction to Design of Experiments: A simplified approach.* ASQ Quality Press, Wisconsin, 1999.

J.E. Bernhardt and D.R. Williams. *Proportional Control of Aysmmetric Forebody Vortices. AIAA Journal*, 36(11):2087–2093, November 1998.

CFDRC. *CFD-FASTRAN Theory Manual version 2003.* CFD Research Corporation, 2003.

P.J. Champigny. *Stability of Side Forces on Bodies at High Angles of Attack. AIAA Paper 86-2176*, 1986.

P.J. Champigny. *Side Forces at High Angles of Attack. Why, When, How? La Recherche Aérospatiale*, 4:269–282, 1994.

CSIR-Defencetek. Confidential. Technical report, CSIR, 2004.

R.M. Cummings, J.R. Forsthye, S.A. Morton, and K.D. Squires. *Computational Challenges in High Angle of Attack Flow Prediction. Progress in Aerospace Sciences*, 39:369–384, 2003.

DAS. Confidential. Technical report, Denel Aerospace Systems, 2004.

D. Degani. *Instabilites of Flows over Bodies at Large Incidence. AIAA Journal*, 30(1):94–100, January 1992.

D. Degani and Y. Levy. *Asymmetrical Turbulent Vortical Flows over Slender Bodies. AIAA Journal*, 30(9):2267–2273, September 1992.

D. Degani and L.B. Schiff. *Numerical Simulation of the Effect of Spatial Disturbances on Vortex Asymmetry. AIAA Journal*, 29(2):344–352, February 1991.

P.C. Dexter. *High Angle of Attack Missile Aerodynamics. Journal of Aerospace Engineering*, 207:15–19, 1993.

ERCOFTAC. *Best Practice Guidelines, Version 1.0.* Technical report, European Research Community On Flow, Turbulence and Combustion, January 2000.

L.E. Ericsson and J.P. Reding. *Tactical Missile Aerodynamics*, volume 141, chapter *Chapter 10: Asymmetric Vortex Shedding on a Slender Body of Revolution*, pages 391–452. Progress in Astronautics and Aeronautics, second edition, 1991.

ESDU. *Normal force, pitching moment and side force of forebody cylinder combinations for angles of attack up to 90 degrees and Mach numbers up to 5*-esdu 89014. Technical report, Engineering Science Data Unit, 1989.

J.E. Fidler. *Active Control of Asymmetric Vortex Effects. Journal of Aircraft*, 18(4):267–272, April 1981.

J.E. Fidler and M.C. Bateman. *Asymmetric Vortex Effects on Missile Configurations. Journal of Spacecraft and Rockets*, 12(11):674–681, November 1975.

S.G. Gobey. *Examination of Historical Wind Tunnel Testing Data.* Internal document, Denel Aerospace Systems, 2004.

G.Zilliac, D. Degani, and M. Tobak. *Asymmetric Vortices on a Slender Body of Revolution. AIAA Journal*, 29(5):667—675, May 1991.

P.M. Hartwich, R.M. Hall, and M.J. Hemsch. *Navier-Stokes Computations of Vortex Asymmetries Controlled by Small Surface Imperfections. Journal of Spacecraft and Rockets*, 28(2):258—264, February 1990.

Y. Levy, D. Degani, and A. Seginer. *Graphical Visualisation of Vortical Flows by Means of Helicity. AIAA Journal*, 28(8):1347–1352, August 1990.

Y. Levy, L. Hesselink, and D. Degani. *Systematic Study of Correlation between the Geometrical Disturbances and Flow Asymmetrices. AIAA Journal*, 34(4): 772–777, April 1996.

P. Luo, W. Yankai, and L. Degani. *Flowfield around Ogive/Elliptic Tip Cylinder at High Angles of Attack. AIAA Journal*, 36(10):560–566, October 1998.

F.R. Menter. *Ten Years of Experience with the SST Turbulence Model. Turbulence, Heat and Mass Transfer*, 4, 2003.

T.T. Ng. *Effect of a Single Strake on the Forebody Vortex Asymmetry. Journal of Aircraft*, 27(9):844–846, September 1990.

T.T. Ng. *Effect of a Nose-Boom on Forebody Vortex Control. Journal of Aircraft*, 29(4):738–741, July-August 1992.

T.T. Ng and G.N. Malcolm. *Forebody Vortex Control using Small Rotatable Strakes. Journal of Aircraft*, 29(4):671–678, July-August 1992.

D.M. Rao, C. Moskovitz, and D.G. Murri. *Forebody Vortex Management for Yaw Control at High Angles of Attack. Journal of Aircraft*, 24(4):248–254, April 1987.

J.L. Thomas and P.M. Hartwich. *Tactical Missile Aerodynamics: Prediction Methodology*, volume 142, chapter Navier-Stokes Analyses of Flows over Slender Airframes, pages 561–648. Progress in Astronautics and Aeronautics, second edition, 1991.

D.C. Wilcox. *Turbulence Modeling for CFD*. DCW Industries, second edition, 2000.

C. Xuei, D. Xueying, W. Yankui, L. Peiqing, and G. Zhifu. *Influence of Nose Perturbations on Behaviours of Asymmetric Vortices over Slender Body. AIAA Journal*, 38(4):358–388, April 2000.

D. Xueying, W. Gang, C. Xuerui, W. Yankui, L. Peiqing, and X. Zhongxiang. *A Physical Model of Asymmetric Vortices Flow Structure in Regular State over Slender Body at High Angle of Attack. Science in China*, 1991.

C.C. Yuan and R.M. Howard. *The Effects of Forebody Strakes on a Missile. Journal of Spacecraft and Rockets*, 28(4):411–417, July-August 1991.